ABSTRACT

Title of dissertation: ELASTICITY IN FERROMAGNETIC
SHAPE MEMORY ALLOYS

Liyang Dai, Doctor of Philosophy, 2004

Dissertation directed by: Professor Manfred Wuttig
Department of Materials Science and Engineering

Ferromagnetic shape memory alloys (FSMAs) are a new class of active materials, which combine the properties of ferromagnetism with those of a diffusionless, reversible martensitic transformation. These materials are technologically interesting due to the possibility of inducing large shape changes with an external applied magnetic field; either inducing the austenite/ martensite transformation or rearranging the martensitic variant structure with an applied field will induce a reversible shape change. The dependence of a solid's elastic properties on temperature in the vicinity of a structural transformation provides insight into the nature of the transition. Therefore, the elasticity of Ni_2MnGa and Fe_3Pd were studied.

The temperature dependence of the elastic constants of the austenitic Ni_2MnGa, $Ni_{0.50}Mn_{0.284}Ga_{0.216}$ and $Ni_{0.49}Mn_{0.234}Ga_{0.276}$, were studied by an ultrasonic continuous wave method. Anomalous behavior in austenite was observed, which indicates a premartensitic transition. The temperature dependence of the elastic constants in martensitic $Ni_{0.50}Mn_{0.284}Ga_{0.216}$ indicates a structural phase change from the

tetragonal to a second phase at lower temperature. Modeling this phase change as a reentrance transition reproduces the major aspects of the temperature dependence of the shear elastic constant, $(C_{11}\text{-}C_{12})/2$.

The elasticity as a function of temperature and magnetic field of Fe_3Pd was studied as well. An abrupt change of the elastic constants at around 45°C indicates a possible premartensitic transformation. The magnetic field dependence of elastic constants also indicates a probably magnetic field induced transition.

ELASTICITY IN FERROMAGNETIC SHAPE MEMORY ALLOYS

by

Liyang Dai

Dissertation submitted to the Faculty of the Graduate School of the
University of Maryland, College Park in partial fulfillment
of the requirements for the degree of
Doctor of Philosophy
2004

Advisory Committee:

Professor Manfred Wuttig, Chairman/Advisor
Adjunct Professor James R. Cullen
Professor George E. Dieter
Professor Alison Flatau
Dr. Kristl B. Hathaway
Professor Alexander Roytburd
Professor Ichiro Takeuchi

DEDICATION

for my family.

ACKNOWLEDGEMENTS

I would like to begin my thanking by thesis advisor, Professor Manfred Wuttig, who introduced me to the exciting field of magnetism, magnetic materials and ferromagnetic shape memory alloys. This research work would not have been realized without his academic and financial support over the years of my graduate study. His enthusiasm and collaborative spirit helped to create a great work environment, and his amazingly broad knowledge and experience gave my research both direction and inspiration.

I am most grateful to Professor James Cullen, who advised me with the riches of his theoretic knowledge. Particular gratitude goes to Dr. Jun Cui, who have helped me learn various aspects of this fascinating field. I am truly grateful for these valuable experiences.

I would especially like to thank all the members of my committee for their efforts on my behalf: Professor Manfred Wuttig, Professor James Cullen, Professor Ichiro Takeuchi, Dr. Kristl Hathaway, Professor Alexander Roytburd, Professor Alison Flatau and Professor George Dieter.

Particular and heartfelt thanks go to those friends and colleagues who selflessly helped me in these years of study. I apologize in advance to those whose important contributions have been overlooked here because of my own unfamiliarity with them or my inability to fully appreciate their significance.

TABLE OF CONTENTS

LIST OF TABLES

LIST OF FIGURES

Chapter 1

Introduction

Smart materials have one or more properties that can be dramatically altered by external fields. They are distinctly different from structural materials. Their physical and chemical properties are sensitive to a change in the environment such as temperature, pressure, electric field, magnetic field, optical wavelength, adsorbed gas molecules, and pH. Smart materials are the components of a smart system.

A smart system is a multifunctional structure with the capabilities of sensing, processing, actuating, feedback, self-diagnosing, and self-recovery. All these characteristics are based on the functionality of the materials composing the system and their intercommunication. The system uses the functional properties of advanced materials to achieve high performance with capabilities of recognition, discrimination, and adjustment in response to a change of its environment. Each component of this system must have functionality, and the entire system is integrated to perform a self-controlled smart action, similar to a living creature that can think, judge, and act. A smart system can be considered as a design philosophy that emphasizes prediction, adaptation, and repetition. Each smart material

in the smart system is required to have a specific functionality, such as sensing a change in its environmental conditions, actuating a mechanical or electric response simultaneously, automatically modifying one or more of its property parameters, and quickly recovering its original status once the environmental conditions are changed. The materials have the ability to modify their intrinsic structures, the band structure or the domain structure, in response to an external change, such as temperature, electric field, stress field, or magnetic field. In other words, smart materials have large mechanical response coefficients in the external fields.

Smart materials can be divided in to three categories according to the different external fields: Ferromagnetic materials, Ferro-electrical materials, Shape Memory Alloys (SMA). In these three kinds of smart materials the mechanical response is magnetostrictive, piezoelectric (electro-strictive) or thermo-strictive (thermo-mechanical) coefficient, respectively. The mechanical response of each material can be written as: $\epsilon \sim f(H, E, \sigma, T)$, where H: magnetic field, E: electrical field, σ: Stress field, and T: temperature. Three of the most widely used smart materials are piezoelectric, magnetostrictive and the shape memory alloy. These materials can be taken as typical examples to briefly illustrate structural characteristics of the smart materials. Recently many new materials with multiple functionalities have been found, such as FE-FM, FESMA, FMSMA. In this work, we concerned with the ferromagnetic shape memory materials, which display a large magnetic field induced strain and martensitic transformation. To date, various ferromagnetic shape memory alloys, e.g. Ni_2MnGa [62], FePd [30], FePt [67], NiCoGa [67], NiCoAl [67], have been investigated. They have both properties of ferromagnetic and shape memory alloys. Hence, they display a giant magnetostriction that consists really of a magnetically induced domain redistribution. The understanding

of this mechanism requires knowledge of the elastic properties of these materials. This thesis is directed at the elasticity of Ni_2MnGa and Fe_3Pd alloys

1.1 Shape Memory Alloys

Shape memory alloys (SMA) are quite fascinating materials characterized by a shape memory effect and super-elasticity, which are based on the diffusionless and reversible martensitic transformation [40]. They are now being practically used as functional alloys in many areas. They exhibit large work output and can be used as working parts in various actuator systems.

Most shape memory effects are related to the martensitic phase transformation, which is diffusionless and involves a crystallographic shearing deformation. The parent phase of this transformation is called austenite; the product phase is called martensite. There are several ways to transform from austenite to martensite, which accommodates the shape change. If the transformation is induced by temperature, the material has no preference for any of the variants because they all have the same free energy. If the transformation is induced by stress, only certain variants will appear because of local energy minimization.[27] If the martensitic material is also ferromagnetic, there exists the possibility of inducing the martensitic transformation or of rearranging the variants of martensite with a simultaneously magnetic field.

Martensite is the relatively soft and easily deformed phase of shape memory alloys, which exists at lower temperatures. The structure of this phase is twinned which is the configuration shown in the middle of Figure 1.1. Upon deformation this phase takes on the second form shown in Figure 1.1 on the bottom right. Austenite, the stronger phase of shape memory alloys, occurs at higher tempera-

tures. The structure of the Austenite is cubic, shown on the upper part of Figure 1.1. The un-deformed Martensite phase is the same size and shape as the cubic Austenite phase on a macroscopic scale, so that no change in size or shape is visible in shape memory alloys until the Martensite is deformed. Therefore this transition is a thermo-elastic martensitic transformation. Such structural transformations are diffusion-less, reversible and occur between a high temperature phase and the low temperature phase. The high temperature phase has high symmetry whereas the low temperature phase has lower symmetry. Shape memory materials are unique in their ability to accommodate large strains without plastic deformation. When the martensitic transformation occurs, a microstructure of symmetry related and compatible variants is formed, in which two variants meet at a well defined interface called a twin plane as shown in Figure 1.2. The martensite phase has multiple variants, which are symmetry related configurations of the same atomic lattice. An external field could rearrange the different variants in the martensite phase inducing a large strain between the twinned and detwinned structure.

Pseudo-elasticity occurs in shape memory alloys when the alloy is completely composed of Austenite (temperature is greater than Af). Unlike the shape memory effect, pseudo-elasticity occurs without a change in temperature. The load on the shape memory alloy is increased until the Austenite becomes transformed into Martensite simply due to the loading. The loading is absorbed by the softer Martensite, but as soon as the loading is decreased the Martensite begins to transform back to Austenite since the temperature of the SMA is still above Af, and the material returns to its original shape. The most effective and widely used alloys include NiTi, CuZnAl, and CuAlNi, etc.

Shape memory alloys have the large mechanical response to the stress field or

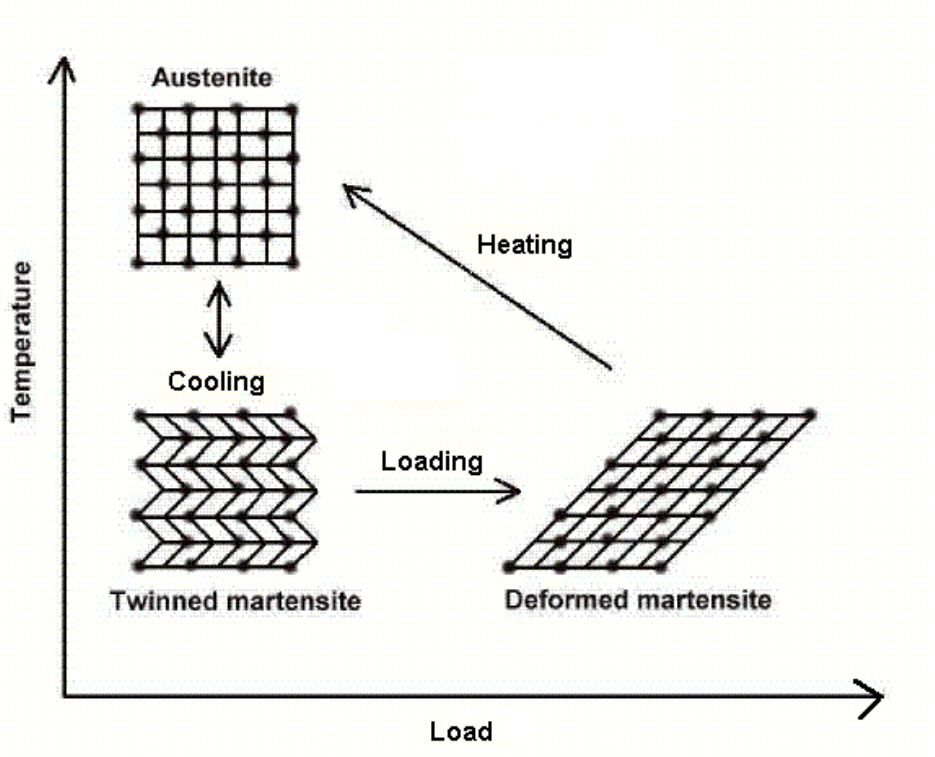

Figure 1.1: Microscopic Diagram of the Shape Memory Effect

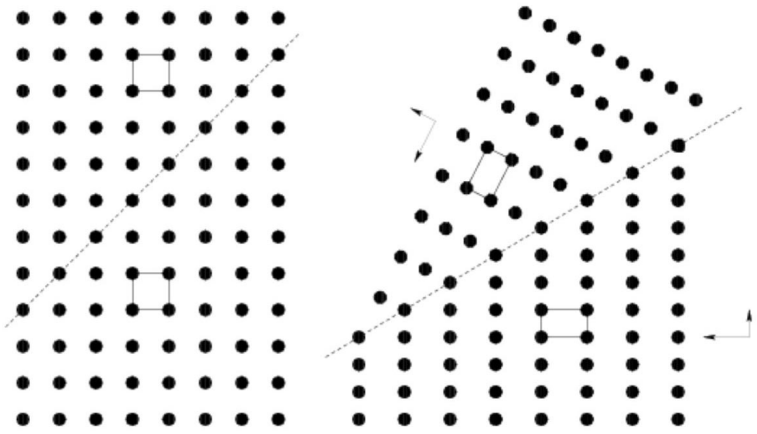

Figure 1.2: Austenitic cubic lattice and martensitic tetragonal lattice in 2D with two variants. The twin planes in the reference cubic lattice and in the deformed tetragonal lattice are shown by the dotted lines.

temperature field. Another type of smart material is the ferromagnetic material, which displays a large strain by applying magnetic field. This strain is equivalent to magnetostriction.

1.2 Magnetostriction

When the magnetization state of a ferromagnetic material is changed by an applied field, there is an accompanying small change in its dimensions. This is called magnetostriction, which is one of the important properties of ferromagnetic materials. Magnetostriction represents the balance of the magnetization, crystalline anisotropy and the elastic energy. It, λ, was defined as:

$$\lambda = \frac{\Delta l}{l} \tag{1.1}$$

where Δl denotes the deformation of the specimen in the magnetic field and l is the length of the specimen[14].

There are two types of magnetostriction. One is the shape magnetostriction, which is also called Joule magnetostriction. It causes the different crystalline directions of the sample to have different strain, however the total volume of the sample will keep the same. Another is the volume magnetostriction, which causes an equal expansion or contraction in all directions. Volume magnetostriction is a very small effect and has no bearing on the behavior of practical magnetic materials in ordinary fields. Therefore in this work, only shape magnetostriction will be considered

The process of magnetization is then one of converting the specimen from a multi-domain state into one in which it is a single domain magnetized in the same direction as the applied filed. Figure 1.3 schematically shows the relationship

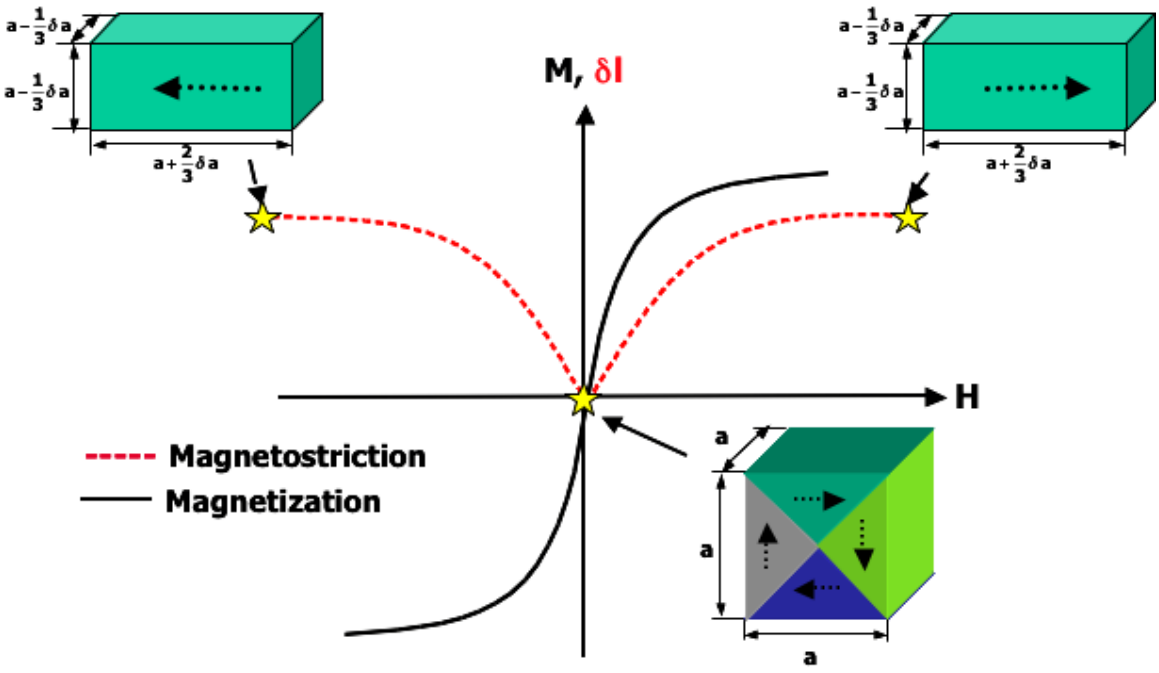

Figure 1.3: Schematic representation of the relationship between the magnetization and magnetostriction. The dashed line is the magnetostriction. The black solid line is the magnetization hysteresis.

between the magnetization and magnetostriction.

Magnetostriction is the shape change of a ferromagnetic material changes during the process of magnetization, so it is the elastic response of a crystal to the spontaneous magnetization.[2] Although the strain $\Delta l/l$ resulting from magnetostriction is small, there exists an inverse effect, which causes many material's properties, such as permeability and the size of the hysteric loop, to be highly dependent on stress. Hence magnetostriction has many practical consequences, and considerable research has been devoted to it.

When a ferromagnetic material is subjected to an applied field, the observed magnetization depends on both the magnitude of the field and the crystallographic direction along which it is applied. The dependence of magnetic properties on

crystallographic direction is known as magnetocrystalline anisotropy, which is of fundamental importance in determining the magnetic properties of ferromagnetic materials.

In a sufficiently large field the magnetization will reach the saturation value, which is the same for all crystallographic directions of one crystal. Magnetization in the various crystallographic directions has an associated energy, and it is the difference in this energy between different directions that determines the magnetic behavior. The crystallographic direction for which the magnetization reaches saturation in the lowest applied field is known as the easy axis of magnetization. The work required to rotate the magnetization away from one of the easy axes with an applied field is described by the magnetocrystalline anisotropy energy. For cubic crystals the energy of magnetization is given by

$$\Psi_{Anis} = K_0 + K_1(\alpha_1^2\alpha_2^2 + \alpha_2^2\alpha_3^2 + \alpha_3^2\alpha_1^2) + K_2(\alpha_1^2\alpha_2^2\alpha_3^2) \tag{1.2}$$

where α_i are the direction cosines of the magnetization with respect to the cubic axes and $\alpha_1^2 + \alpha_2^2 + \alpha_3^2 = 1$. The values of K_0, K_1 and K_2 are material constants associated with the easy, medium and hard axes of magnetization, and have units of ergs/cm^3[14].

The elastic energy density in the approximation of Hooke's law is a quadratic function of the strains. In a cubic crystal, the elastic energy can be represented as:

$$\Psi_{el} = \frac{1}{2}C_{11}(\varepsilon_{xx}^2+\varepsilon_{yy}^2+\varepsilon_{zz}^2)+\frac{1}{2}C_{44}(\varepsilon_{xy}^2+\varepsilon_{yz}^2+\varepsilon_{zx}^2)+C_{12}(\varepsilon_{xx}\varepsilon_{yy}+\varepsilon_{yy}\varepsilon_{zz}+\varepsilon_{zz}\varepsilon_{xx}) \tag{1.3}$$

where C_{11}, C_{44} and C_{12} are the elastic moduli, ε_{xx}, ε_{yy}, ε_{zz}, ε_{xy}, ε_{yz} and ε_{zx} are the strain tensor components[14].

The magneto-elastic interaction energy is a function of the inter-atomic distance, because the magnetostriction originates in the interaction between the

atomic magnetic moments. In a simple cubic lattice, the magnetoelastic energy is presented as:

$$\begin{aligned}\Psi_{magel} &= B_1\left[\varepsilon_{xx}\left(\alpha_1^2-\frac{1}{3}\right)+\varepsilon_{yy}\left(\alpha_2^2-\frac{1}{3}\right)+\varepsilon_{zz}\left(\alpha_3^2-\frac{1}{3}\right)\right] \\ &\quad +B_2\left(\varepsilon_{xy}\alpha_1\alpha_2+\varepsilon_{yz}\alpha_2\alpha_2+\varepsilon_{zx}\alpha_3\alpha_1\right) \qquad (1.4)\end{aligned}$$

where B_1 and B_2 are magnetoelastic coupling constants[8].

When a martensitic ferromagnetic material is exposed to a magnetic field, the magnetostriction produces an elastic strain in the materials that either increases or decreased the magnetoelastic energy, depending on the conditions. Thus the magnetoelastic energy depends on the lattice strain and the direction of domain magnetization. The interaction between an applied stress and magnetostriction is an important effect, and may have a marked influence on the field-dependent magnetic properties. Since the magnetoelastic energy is a linear function with respect to the strains, the crystal will be deformed without limit unless it is counterbalanced by the elastic energy, which is represented by Equation (1.3).

From above discussion, the total energy which relate to the crystal's magnetization status can be expressed as:

$$\Psi_{Total} = \Psi_{Anis} + \Psi_{el} + \Psi_{magel} \qquad (1.5)$$

The equilibrium direction of M_S is that, which renders Ψ a minimum and this direction is a complicated function of K, λ and ε. In cubic crystal the magnetostriction could be calculated at the equilibrium state, $\partial\Psi/\partial\varepsilon = 0$.

$$\begin{aligned}\lambda_{100} &= -\frac{2B_1}{3\left(C_{11}-C_{12}\right)} \\ \lambda_{100} &= -\frac{B_2}{3C_{44}} \qquad (1.6)\end{aligned}$$

Alloy	Magnetostrictive Strain $\lambda_{100}\,[10^{-6}]$	Explanation	Reference
Fe	21	Joule Mangetostriction	[14]
Ni	-46	Joule Mangetostriction	[14]
$Fe_{84}Al_{16}$	86	Joule Mangetostriction	[11]
$Fe_{50}Co_{50}$	140	Joule Mangetostriction	[21]
$Fe_{83}Ga_{17}$	207	Joule Mangetostriction	[10]
$Co_{0.8}Fe_{2.2}O_4$	-590	Joule Mangetostriction	[3]
Terfenol-D (FeTbDy)	1,600	Joule Mangetostriction	[9]
Fe_3Pd	10,000	Reversible Strain resulting from rearrangement of variants	[13]
Ni_2MnGa	100,000	Reversible Strain resulting from rearrangement of variants	[53]

Table 1.1: Overview of Crystalline Metallic Alloys with Magnetostriction λ_{100}

An overview of magnetostrictive materials is listed in Table 1.1. It clearly shows that the magnetically induced strain in FSMAs, Fe_3Pd and Ni_2MnGa, are much larger than the general magnetostrictive ferromagnetic materials.

Since the spontaneous strain in martensitic materials is commonly one order of magnitude larger than that of giant magnetostrictive materials, the field-induced strain available from a material that is both martensitic and ferromagnetic is much larger than that of magnetostrictive materials.

1.3 The Free Energy of Ferromagnetic, Shape Memory and Ferromagnetic Shape Memory Materials

Materials scientists and physicists have spent one decade trying to understand the phase transitions in the Ferromagnetic Shape Memory Alloys (FSMA), particularly the relationship between the microstructure and the magnetic properties in FSMA systems. Here, we introduce the evolution of the SMA and FSMA eigen-strain on the basis of the simplest Landau energy possible. It will be seen that the magnetic anisotropy automatically leads to elastic domains that are differently magnetized.

The magnetoelasticity in ferromagnetic alloys may be formally described by the Landau expansion $\Psi_{ferro}(\varepsilon, M) = -\beta\varepsilon M^2 + C\varepsilon^2/2 - aM^2/2 + bM^4/4$ where the quantity M is the spontaneous magnetization, coefficient a is related to the exchange energy, β is the magnetoelastic coupling constant, C is the elastic constant and b is a constant coefficient of forth order magnetization term. This free energy yields the equilibrium magnetoelastic strain and magnetization in ferromagnetic materials, $\varepsilon_0 = \beta M^2/C$ and $M_0 = \pm\sqrt{(2\beta\varepsilon - a)/b}$

The free energy of the low temperature phase of a SMA may be written as $\Psi_{SMA}(\varepsilon) = \alpha\varepsilon^4/4 - C\varepsilon^2/2$, where α is a constant coefficient and C designates the formally negative shear elastic constant, that relates to the shear strain $\varepsilon_{xx} - \varepsilon_{yy}$. The spontaneous equilibrium strain is now $\mid \varepsilon_{xx} - \varepsilon_{yy} \mid_0 = \pm\sqrt{\alpha/C}$. It designates the two variants of the 2D low temperature phase.

The free energy of a FSMA can be represented by the sum of the Landau energies of SMA and ferromagnetic solids. Then it could be presented in 2D dimension as:

$$\Psi = -\frac{\kappa}{2}\varepsilon^2 M^2 - \frac{C}{2}\varepsilon^2 - \frac{a}{2}M^2 + \frac{\alpha}{4}\varepsilon^4 + \frac{b}{4}M^4 \tag{1.7}$$

Introducing the magnetic anisotropy results in martensitic phase is coupled with the directions of the magnetization. Then the energy is:

$$\Psi_{FSMA} = -\frac{\kappa}{2}\varepsilon^2 M^2 - \frac{C}{2}\varepsilon^2 - \frac{a}{2}M^2 + \frac{\alpha}{4}\varepsilon^4 + \frac{b}{4}M^4 - \beta\varepsilon m + \frac{1}{2}Dm^2 \tag{1.8}$$

where β is the magnetoelastic coupling constant and D is the constant coefficient of M^2 term, $\varepsilon = \varepsilon_{xx} - \varepsilon_{yy}$, $m = M_x^2 - M_y^2$ and $M^2 = M_x^2 + M_y^2$. Expanding around the equilibrium position at $m_{eq} = \beta\varepsilon/D$ and $M_{eq}^2 = (a + \kappa\varepsilon^2)/b = M_0 + \kappa\varepsilon^2/b$ yields

$$\Delta\Psi = \Psi - \Psi_M = -\frac{1}{2}C^*\varepsilon^2 + \frac{1}{4}\alpha^*\varepsilon^4 \tag{1.9}$$

where $\Psi_M = -aM_0^2/2 + bM_0^4/4$ is the magnetization energy, C*$= \kappa M_0 + C - \beta^2/D$ is the new elastic constant with magnetization effect and $\alpha^* = \alpha - \kappa^2/b$ is the new coefficient for the forth order term of ε. The equilibrium strain is then $\varepsilon_{eq} = \pm\sqrt{(C + \kappa M^2 + \beta^2/D)/\alpha}$, which is clearly larger than the equilibrium strain of SMA, $\pm\sqrt{\alpha/C}$. The results of the free energy in FSMA are schematically shown in Figure 1.4.

As can be seen in Figure 1.4, this free energy has two energy wells located at $\varepsilon_0 = \pm\sqrt{(C + \kappa M^2 + \beta^2/D)/\alpha}$ corresponding to the two martensitic variants,

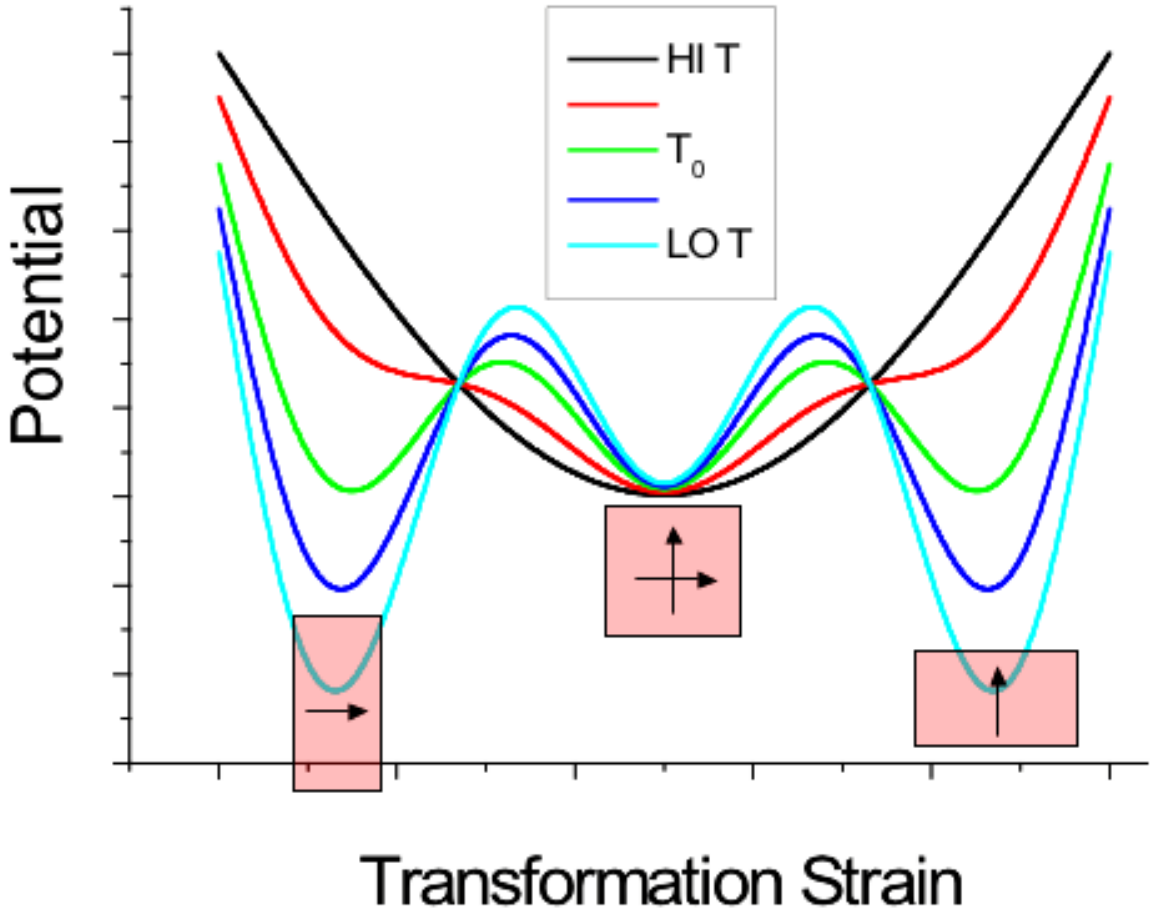

Figure 1.4: Schematic of the free energy of FSMA at $T > T_0$, $T = T_0$ and $T < T_0$, where T_0 is the phase transition temperature. When $T < T_0$, the free energy has two energy wells located at $\varepsilon_0 = \pm\sqrt{(C + \kappa M^2 + \beta^2/D)/\alpha}$ corresponding to the two martensitic variants, $\pm(\varepsilon_{xx} - \varepsilon_{yy})$. The direction of the magnetization is directed along the major or minor axes of the low temperature phase.

$\pm(\varepsilon_{xx} - \varepsilon_{yy})$. Since $(M_x^2 - M_y^2) \propto (\varepsilon_{xx} - \varepsilon_{yy})$, the direction of the magnetization is directed along the major or minor axes of the low temperature phase depending on the sign of β, see Figure 1.4. It follows that the martensitic variants in FSMAs are simultaneously elastic and magnetic variants. Their population could be changed by an elastic and, this is the novel feature of this material, magnetic fields. The curvature of the minimum energy of a FSMA represents the elastic constant, which is the topic of this thesis.

1.4 Ferromagnetic Shape Memory Alloy

Ferromagnetic shape memory alloys (FSMA) are a new class of active materials, which combine the properties of ferromagnetism with those of a diffusionless, reversible martensitic transformation. The term "ferromagnetic shape memory effect" is used to describe the reversible change in shape caused by either inducing the austenite/martensite transformation or rearranging the martensitic variants with an applied magnetic field. The magnetic field rearranges the variants resulting in a giant strain. The variant rearrangement phenomenon is a complicated one that depends on twin boundary mobility, the magnetic properties of the martensite, proper biasing of the initial microstructure, proper specimen orientation, and specimen shape, among others.

Rearranging martensite variants by a magnetic field is a novel idea and received attention only in recent years. In 1996, Vasil'ev *et al.* [62] measured the magnetostriction in the $\langle 110 \rangle$ directions of a Ni_2MnGa single crystal, and suggested the existence of field-induced shape memory effect. In the same year, Ullakko *et al.* [60] demonstrated the field-induced variant rearrangement by measuring a 0.2% field-induced strain in an unstressed Ni_2MnGa single crystal. In the experiments,

the field applied to induce the shape change was 8 kOe, which is considerably lower than the field commonly used to study the effect of magnetic field (40-350 kOe) on phase transformation temperatures. In 1998, a larger reversible field-induced strain of 0.6% under cyclic fields of 10 kOe has been achieved in $Fe_{70}Pd_{30}$ [30]. In 1999, Tickle *et al.* [58] reported the largest field-induced strain of 4.5% in Ni_2MnGa. In their experiments, the evidence of field-induced variants rearrangement, the movement of twin interfaces by the applied magnetic field, was directly observed. Theoretical work regarding the field induced variant rearrangement was carried out by Wuttig, James and Desimone [30, 17], and O'Handley [44].

1.4.1 Magnetic Field Induced Strain

A ferromagnetic material in the demagnetized state is divided into a number of domains. Each domain is spontaneously magnetized to the saturation value M_S, but the directions of magnetization of the various domains are such that the specimen as a whole has no net magnetization, as shown in Figure 1.6. If the martensitic transformation is induced by temperature, the material has no preference for any of the variants because they all have the same free energy. When stress is applied to this mixture of variants, only certain variants will appear due to local energy minimization. The process of magnetization is then one of converting the specimen from a multi-domain state into one in which it is a single domain magnetized in the same direction as the applied magnetic filed. The process of magnetization occurs by two mechanisms, domain-wall motion and domain rotation; most of the magnetostrictive change in length usually occurs during domain rotation.

The magnetic field induced strain in ferromagnetic shape memory alloy is different from the ordinary magnetostriction. Magnetostriction is the spontaneous

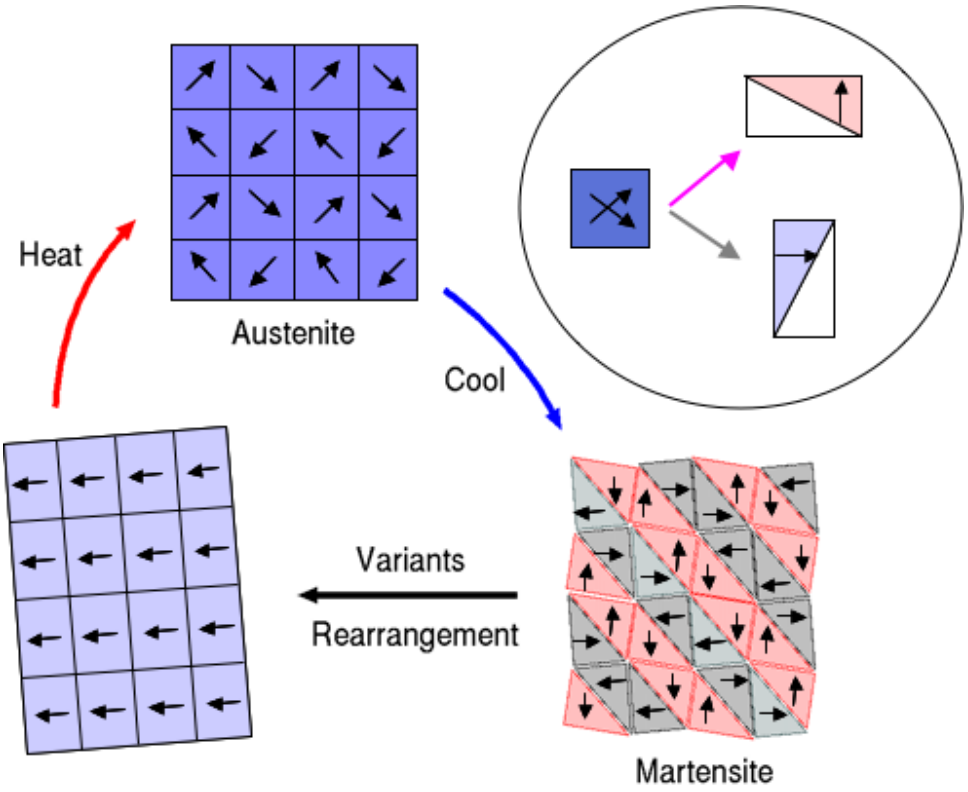

Figure 1.5: Cartoon of the phase transition process and the twin structure in the Ferromagnetic Shape Memory alloy.

deformation of a solid in response to its magnetization. Martensitic transformation produces a spontaneous deformation of a solid to form a martensite twin structure, upon lowering the temperature. If the martensitic material is also ferromagnetic, there exists the possibility of inducing the martensitic transformation or of rearranging the variants of martensite to yield large strain by applying a magnetic field. Since the spontaneous strain in martensitic materials is commonly one order of magnitude larger than that of giant magnetostrictive materials, the field-induced strain available from a martensitic or ferromagnetic material is potentially much larger than giant magnetostrictive materials.

The recent progress in designing of a new class of magnetic shape memory alloys is based on the physical mechanism of the martensite-martensite twin boundary motion driven by magnetic field in a martensitic state. There exist three possible mechanisms that can produce the shape change. First, applying a magnetic field induces a structural transition, as in Fe-Ni alloys.[51] This requires very large field, about 10 tesla for a 20°C shift. Secondly, a magnetic field rotates the spontaneous magnetization with respect to the crystal lattice, as in Terfonol-D.[9] This requires negligible magneto-crystalline anisotropy, so that there is little or no energy cost for rotating the magnetization. Thirdly, a magnetic field rearranges the martensite variants, as in Ni_2MnGa [57] and $Fe_{70}Pd_{30}$ [30]. This third mechanism could result in large strains compared to the other two, and requires high twin interface mobility, large magnetization, and large magnetic anisotropy. The large anisotropy essentially pins the spontaneous magnetization along the crystalline easy axis, ensuring a significant driving force on the twin interfaces.

Figure 1.6 shows schematically the different process between magnetostriction and magnetic field induced strain. Consider a rectangular bar specimen with $\langle 100 \rangle$

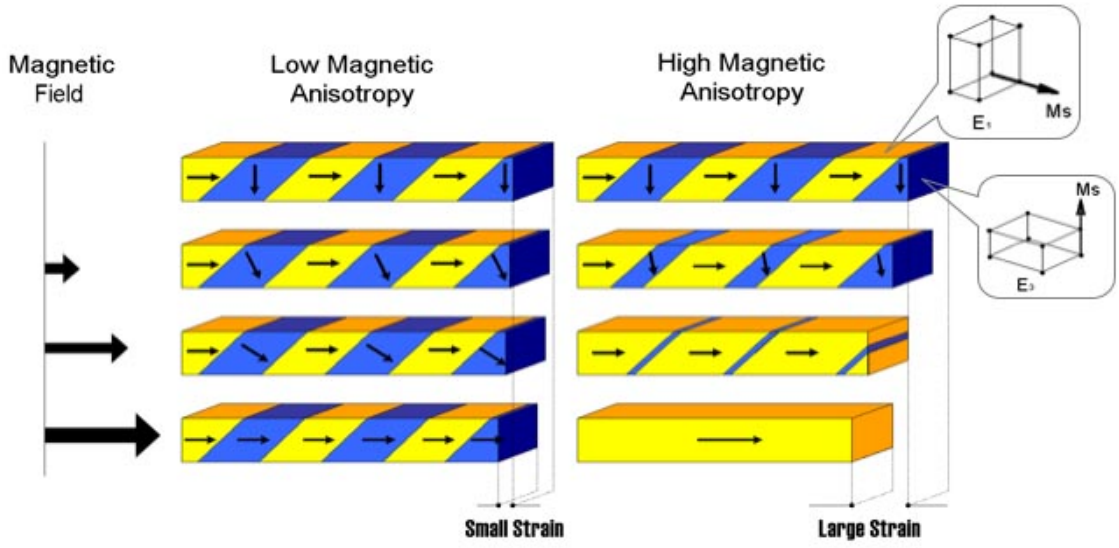

Figure 1.6: Comparing the two different process of magnetization by magnetic anisotropy.

edges with two variants of martensite. A uniaxial layered magnetic substructure is present within each variant as shown at zero applied field. When a field is applied along the long axis of the bar, the variant with horizontal magnetization is favored and its volume fraction increases at the expense of the other variant. For large enough fields, the specimen may be completely detwinned, resulting in a large shape change as shown. The high magnetic anisotropy is one of the most important properties of FSMA. It decides which magnetic process would require the lower energy.

1.4.2 Ferromagnetic Shape Memory Alloys Ni_2MnGa

The recent progress in designing of a new class of Ferromagnetic Shape Memory Alloys (FSMA) is based on the physical mechanism of the martensite–martensite

twin boundary motion driven by magnetic field. The main thermodynamic driving forces in this case have been magnetic in nature and are connected with high magnetization anisotropy and significant differences in magnetization free energies for different twin variants of martensite. By now, the largest magneto-strain effects were achieved in NiMnGa ferromagnetic shape memory alloys.

Heusler alloys Ni_2MnGa have two transformations: a ferromagnetic transition and a martensitic transformation. Depending on how the Curie temperature and the martensitic transformation temperature are ordered, the material could be expected to have different behaviors. The elasticity yields the information concerning the intrinsic properties of the materials for understanding the nature of these transformations.

Phase Transitions in Ni_2MnGa

Heusler alloy Ni_2MnGa belongs to the family of ternary intermetalic compounds, with X_2YZ composition and $L2_1$ lattice structure. The unit cell of Ni_2MnGa is shown in Figure 1.7. In Heusler alloys, the manganese atoms mainly carry the magnetic moment. Neutron diffraction experiments performed by Webster et al. (1984) [64] confirmed the ordered $L2_1$ structure in Ni_2MnGa, and measured a moment of $4.17\mu B$ for the manganese atoms, with a small moment, $< 0.3\mu B$, possibly associated with the Ni atoms. They also reported a martensitic transformation temperature of $-71°C$ with a small thermal hysteresis of less than $5°C$. In 2002, several kinds of martensitic phase have been found in nonstoichiometric Ni_2MnGa alloys in numerous studies. The structural, magnetic, and mechanical properties important for a giant magnetic field induced strain response in these alloys were reported. [54] Several research groups have succeeded in observation

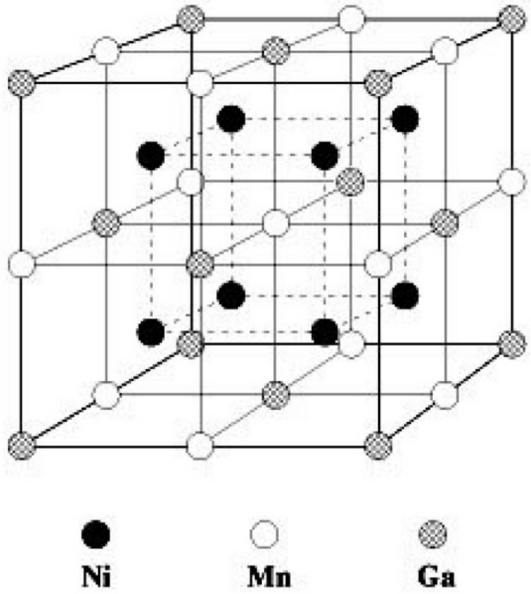

Figure 1.7: The Heusler $L2_1$ lattice structure in Ni_2MnGa.

and detailed the investigation of super large 6% magneto strain effect found in the five-layer modulated tetragonal martensitic phase[58, 38, 45, 53]. The Sozinov group reported the much larger, up to 10%, magnetic field induced strain in seven-layer modulated orthorhombic martensite[53]. The important properties of martensitic phases in Ni_2MnGa with different compositions are listed in Table 1.2. The properties of Ni_2MnGa are very sensitive to the composition. One of the crystal structures of the martensite phase was identified as tetragonal, which also has five-layer shuffling type modulation, 5M, and a tetragonality aspect ratio $c/a < 1$. [37, 34] Depending on the chemical composition and temperature there are also two other kinds of martensitic phases in Ni_2MnGa that have orthorhombic seven-layered and tetragonal non-layered crystal structures with $c/a > 1$ [54]. A $(110)[1\bar{1}0]$ shuffle (or modulation) is observed in both 5 M and 7 M phases. [53, 54]. The X-ray studies [54] showed that the martensitic transformation in Ni_2MnGa is

actually quite complex and exhibits a number of stress induced phases in addition to the thermal martensite formed upon cooling.

Phase transitions in Ni_2MnGa seven–layered martensite were studied by Sozinov. Figure 1.8 shows the temperature dependence of the low-field ac magnetic susceptibility of the alloy during heating and cooling. The abrupt change in the value of the susceptibility at 367$\sim$ 369 K is attributed to paramagnetic–ferromagnetic transformation of the $L2_1$ cubic phase. The Curie temperature is about $T_C = 368K$. During the cooling–heating cycle a sequence of martensitic and intermartensitic transformations was also observed. The martensitic transformation starts at 337 K (M_s) and is completed at 333 K (M_f) during cooling. At lower temperatures, starting at 245 K, the value of the magnetic susceptibility increased, indicating an intermartensitic transformation. During heating both structure transformations occur in reverse order and show some temperature hysteresis. In particular, the reverse intermartensitic transformation takes place during heating at 306–316K. The reverse martensitic transformation from the orthorhombic to the cubic parent phase upon heating takes place between $A_s = 338$ K and $A_f = 342$ K.

Moreover, Ni_2MnGa exhibits an intermediate, pre-martensitic state, in the temperature region between T_C and M_s. The Ni-Mn-Ga alloys with specific compositions show interesting precursor phenomena at temperatures above the martensitic transitions, which develops a micro-modulated structure. [6, 7, 20, 41, 43] This premartensitic transition is found to occur only for alloys with an electrons to atoms ration, e/a, smaller than 7.60. The two Ni_2MnGa crystals we studied have e/a of about 7.636 and 7.366, which are either lower or slightly higher than 7.60. Therefore we did anticipate finding a premartensitic transition in them. In addition to

Martensite Type	5M $(c/a < 1)$	T $(c/a > 1)$	7M $(a > b > c)$
Composition, $at.\%(\pm 0.5\%)$	$Ni_{49.2}$ $Mn_{29.6}$ $Ga_{21.2}$	$Ni_{52.1}$ $Mn_{27.3}$ $Ga_{20.6}$	$Ni_{48.8}$ $Mn_{29.7}$ $Ga_{21.5}$
Lattice Parameters, nm	$a = 0.594$ $b = 0.594$ $c = 0.559$	$a = 0.546$ $b = 0.546$ $c = 0.658$	$a = 0.619$ $b = 0.580$ $c = 0.553$
Cell volume, nm^3	0.197	0.196	0.199
$\varepsilon_0 = (1 - c/a)\,\%$	5.89	20.5	10.66
σ^s, MPa	1	12-20	1.1
σ^f, MPa	2.1	12-20	1.9
$(\mu_0 M_s)$, T	0.6±0.05	0.6±0.05	0.6±0.05
Magnetic anisotropy, $10^5 J/m^3$	1.45(K_u)	-2.01(K_u)	1.6(K_a) 0.7(K_b)
MSM strain, %	5.8	Less than 0.02	9.4
Valance electron ratio, e/a	0.7628	0.7739	0.7604

Table 1.2: Single-crystal samples of Ni-Mn-Ga with different martensitic structure at room temperature[53]

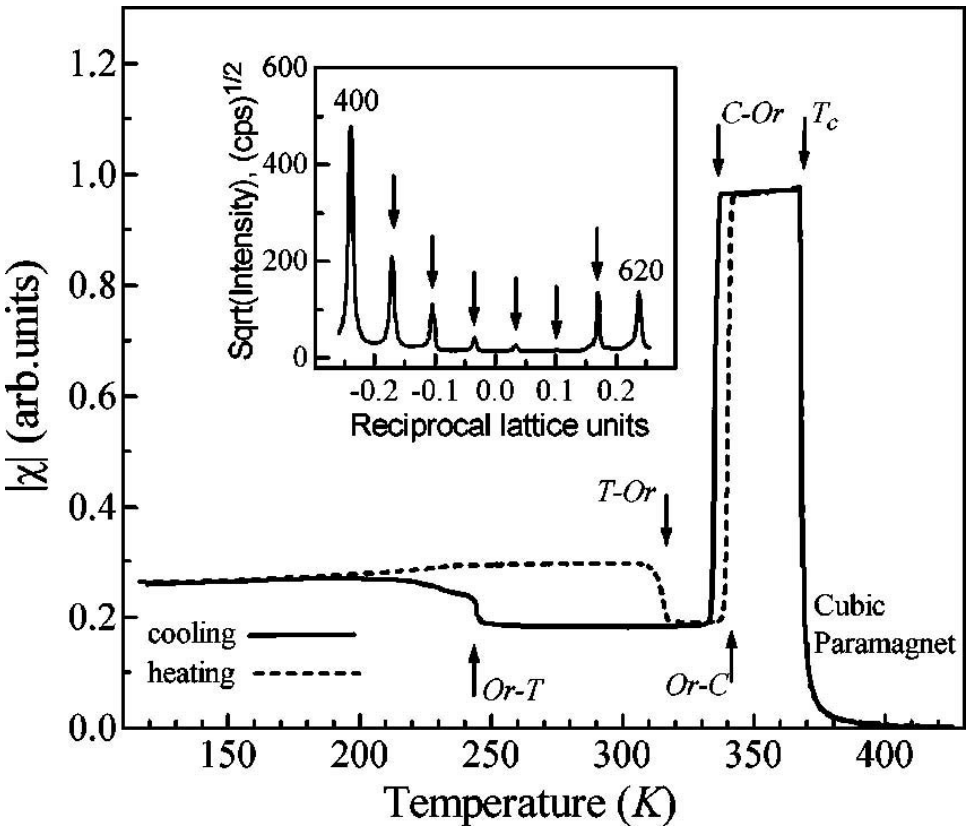

Figure 1.8: Temperature dependence of low-field ac magnetic susceptibility measured during cooling (solid line) and heating (dashed line) of the $Ni_{48.8}Mn_{29.7}Ga_{21.5}$ alloy. Arrows mark phase transformations. C: ferromagnetic cubic phase, Or: orthorhombic seven-layered phase, T: tetragonal nonmodulated phase. The inset shows the scattering intensity distribution in reciprocal space between (400) and (620) nodes in the orthorhombic phase of the $Ni_{48.8}Mn_{29.7}Ga_{21.5}$ alloy. Arrows mark additional peaks connected with seven-layered modulation of the lattice. [53]

the temperature near M_S, anomalous behavior of elastic moduli is expected to occur near the Curie temperature T_C. In previous elastic modulus studies, the lattice instability of the parent phase when approaching transformation temperature has been observed [19, 56], which is a manifestation of precursor events. An almost linear softening of the elastic modulus in the paramagnetic state may also be associated with it. Both ultrasonic investigations and neutron scattering studies of polycrystalline Ni_2MnGa alloys indicate that the slope of E(T), the Young's modulus as function of temperature, changes near the Curie point. [7]. According to our study on the elastic constants temperature dependence on the single crystalline Ni_2MnGa, the bulk elastic softening event is more pronounced in single crystals.

Magnetic Properties in Ni_2MnGa

The ferromagnetic shape memory effect, which differs from the ordinary magnetostriction by its mechanism, is driven by the magnetic anisotropy energy. The effect is based on the magnetic-field-induced redistribution of twin variants in the martensitic phase. When Ni_2MnGa alloy is cooled down, it undergoes a structural transformation from a cubic, austenitic phase, to a tetragonal structure, martensitic phase. In the cubic structure there are three equivalent crystallographic directions for the tetragonal deformation. Therefore, the martensitic phase consists of twin variants, which have different deformation directions and are separated by well-defined boundaries. Naturally, the local crystallographic structure determines the easy axis of magnetization, so that different variants have a different global direction for the easy axes i.e., the local magnetic moments in the different variants have different directions in the absence of an external magnetic field. Figure 1.9 represents the three variants that arise on cooling below martensitic transforma-

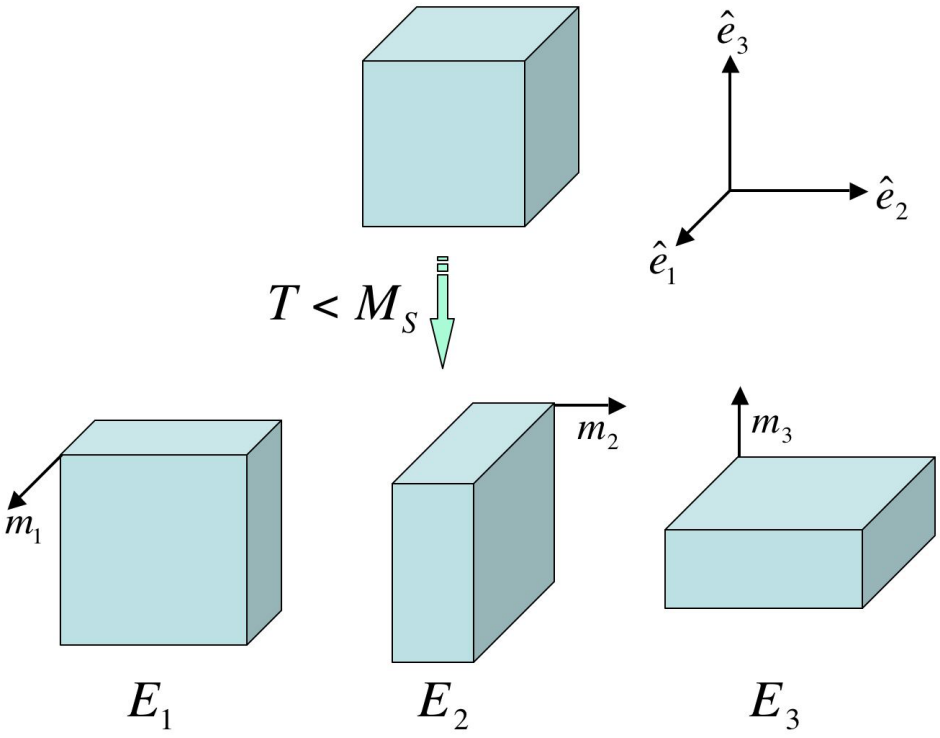

Figure 1.9: Tetragonal variants structure and associated magnetizations. The cubic axes are denoted using basis $\widehat{e}_i$, and the martensitic variants and associated magnetizations by E_i and m_i, where the compression axis along $\widehat{e}_i$ uniquely defines each variant.

tion temperature, M_s. The lattice deformation of a simple unit cell associated with each variant is shown with the strain exaggerated for clarity. Note that the magnetization could be also able to point in the $\pm$ directions of the m_i shown in Figure 1.9. When an external magnetic field is applied to the sample, the local magnetizations try to align with the external field. For fields below saturation and samples with a large enough magnetic anisotropy energy, it will be energetically favorable to redistribute the twin variants: instead of rotating the magnetizations with respect to their local crystal structure, the twin boundaries will move and the easy axes align with the field. This movement leads to the large shape changes observed in the Ni_2MnGa. The mechanism of the large strain is based on the magnetic field induced rearrangement of the crystallographic twin variants that lower magnetization energy. Macroscopically this strain appears as a magnetostrictive strain. The magnetic anisotropy energy, elastic energy and their association, magnetoelastic energy, are very important in FSMA. Figure 1.6 shows a schematic representation of the field-induced variant rearrangement process.

The martensitic anisotropy of a single variant of Ni_2MnGa martensite was determined by Tickle.[57] The specimen was compressed into a single variant microstructure using the small fixture shown to the right of Figure 1.10, and M-H curves parallel and perpendicular to the compression axis as shown were generated. The applied stress in the single variant state was required to prevent the nucleation of a second variant for applied fields perpendicular to the compression axis, and also allowed for a determination of the ordinary magnetostriction constant from stress anisotropy effects. Figure 1.11 presents the M-H curve of Ni_2MnGa. It shows the easy axis within a single variant is the c-axis, short axis, and the anisotropy is uniaxial in nature.

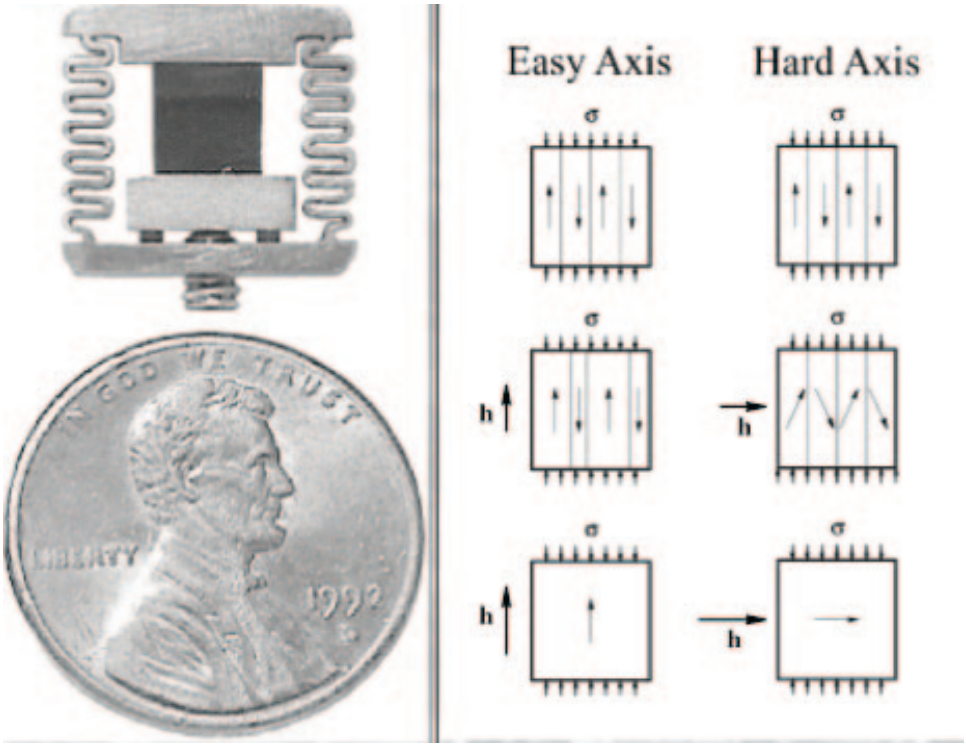

Figure 1.10: Schematically shows the M-H curves parallel and perpendicular to the compression axis (right). The fixture (left) was constructed from a non-magnetic CuBe spring alloy and sized to fit in the cooling fixture used with the VSM [57]

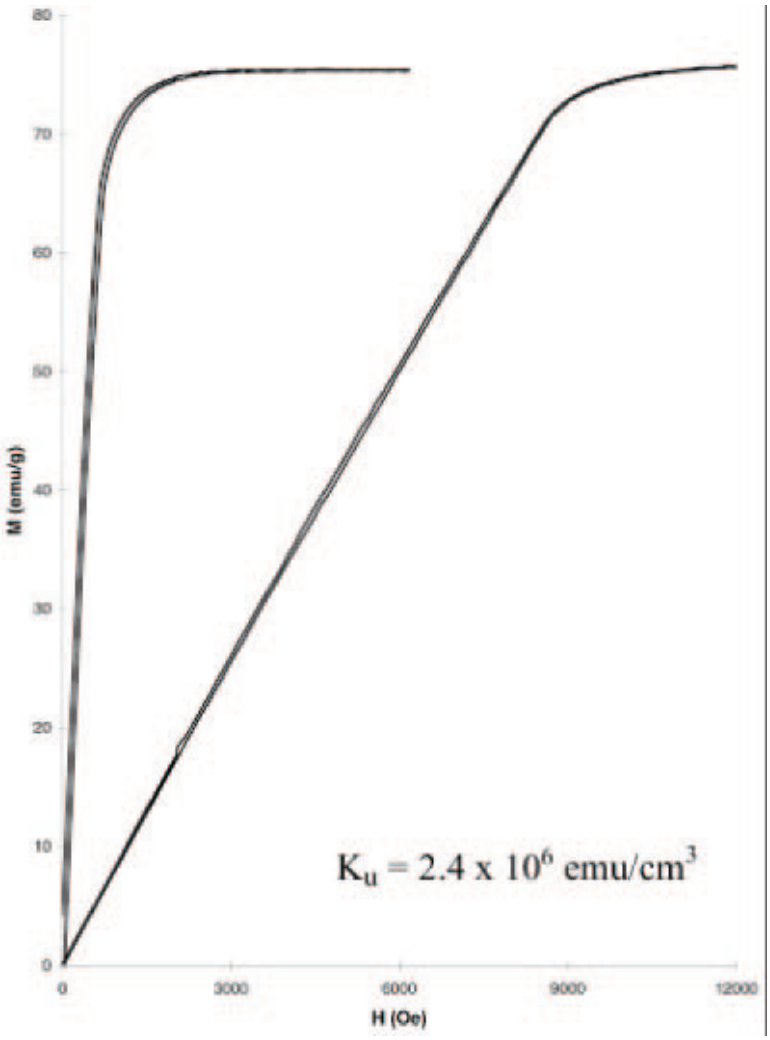

Figure 1.11: This graph shows the M-H curve along c-axis (easy axis) and a-axis (hard axis) determined at $-17°C$ with 1.9 MPa applied stress. The results show that the easy axis within a single variant is the c-axis as expected, and the anisotropy is uniaxial in nature. Uniaxial anisotropy constant K_U was calculated from the areas between these 2 curves and found to be $K_U = 2.4 \times 10^6 ergs/cc$.[57]

1.4.3 Ferromagnetic Shape Memory Alloys Fe_3Pd

Iron palladium alloys at certain compositions are ferromagnetic shape memory materials with high coercivity. The research in FePd was motivated by the potential of its use as a permanent magnet and in magnetic recording media. Alloys with composition near $Fe_{70}Pd_{30}$ undergo a highly reversible FCC to FCT transformation, and have high saturation magnetization, approximately 2/3 to that of Fe at room temperature. Therefore, they are good candidates for a ferromagnetic shape memory material.

The phase diagram of Fe-Pd is shown in Figure 1.12. The high temperature FCC phase, γFe, Pd, is a continuous solid solution. At lower temperatures, there exists α_1-FePd and α_2-FePd. These two ordered phases,α_1-FePd and α_2-$FePd_3$ are formed at about $790\pm20°C$ and $820\pm20°C$, respectively [35]. Their structural properties are listed in Table 1.3 and depicted in Figure 1.13. Notice that $L1_0$ has a tetragonal structure with alternate layers of atoms, *i.e.*, Fe or Pd atoms; $L1_2$ has a cubic structure with one kind of atom (Fe) at one corner, and the other kind of atom (Pd) at the face center. The first attempt to determine the lattice parameters vs. composition was made by Raub *et al.* in 1963 [47]. The results are listed in Table 1.4. Due to the limitation of the equipment at that time, the accuracy of the data can only be ±0.001Å.

In 2002, Cui [12] investigated a phase diagram to show the phase transformation temperature as function of palladium concentration as Figure 1.14. The phase diagram shows that for palladium concentration less than 29.25 at%, the phase transformation is FCC to BCT. The transition temperature increases as the concentration of palladium decreases. For palladium concentration more than 29.25 at%, the phase transformation is FCC to FCT, followed by FCT to BCT.

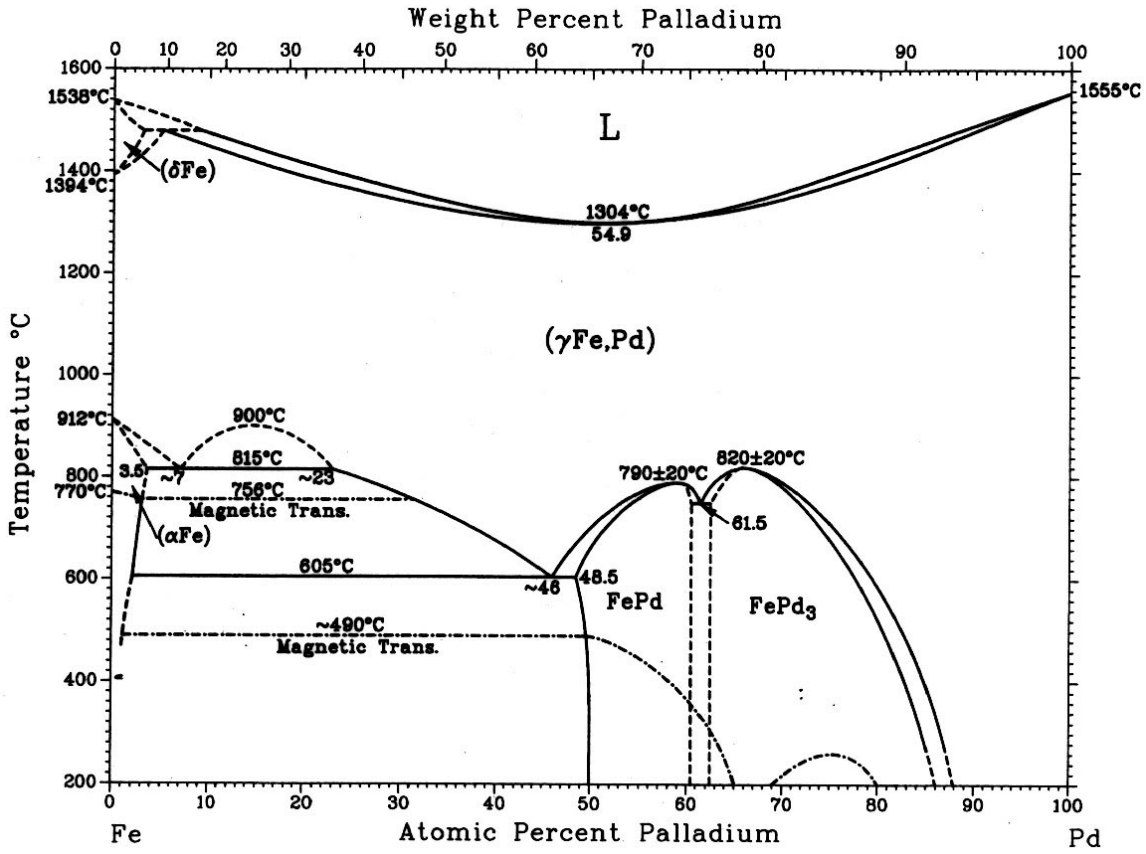

Figure 1.12: Phase diagram of Fe-Pd alloy system.

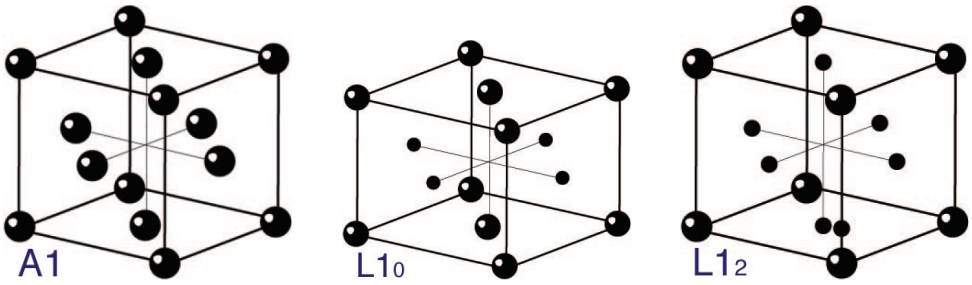

Figure 1.13: Schematic drawing of A1, $L1_0$ and $L1_2$ crystal structures. The radii of the atoms are exaggerated for clarity. The structure of γ-(Fe,Pd), γ_1-FePd, and γ_2-$FePd_3$ are A1, $L1_0$ and $L1_2$, respectively. [12]

Phase	Pearson Symbol	Space Group	Strukturbericht Designation	Lattice Parameters
α-Fe	cB2	$Fm\bar{3}m$	A2	2.866Å at 0%Pd [29]
				2.879Å at 2.4 at.%Pd
γ-(Fe, Pd)	cF4	$Fm\bar{3}m$	A1 (Cu)	a=3.770-3.867Å [47]
γ_1-FePd	tP2	P4/mmm	$L1_0$ (CuAu)	a=3.87-3.88Å,
				c/a=0.95-0.96 [47, 28]
γ_2-$FePd_3$	cP4	$Pm\bar{3}m$	$L1_2$ ($CuAu_3$)	a=3.837-3.853Å [47, 28]

Table 1.3: Crystal Structures and parameters of the phases in Fe-Pd Alloy System

Both of the transition temperatures decrease as the palladium concentration increases, but the decrease of the FCC to the FCT is slower than that of the FCT to the BCT. If the palladium concentration exceeds $29.7at\%$, only the FCC to FCT transition exists in the phase diagram.

Three phase transformations exist in $Fe_{70}Pd_{30}$. They are FCC to FCT, FCT to BCT, and FCC to BCT. The microstructures of FCT phases are twin bands and that of BCT have the shape of a spear-head. The phase transformation temperatures are sensitive to the composition. The phase diagram shows that the Fe-Pd alloys with palladium content ranges from 29.5 to 30.5 at.% are suitable for the study of ferromagnetic shape memory effect. Both x-ray analysis and DSC measurements show that the FCC to FCT transformation is a first order transition [12]. The average lattice parameters are a=3.8220 Å and c=3.6298 Å for the martensite, and a_0=3.7557 Å for the austenite. The latent heat is 1.244 J/g (10.698 J/cm^3) for the cooling and 1.267 J/g (10.896 J/cm^3) for the heating. The Curie temperature equals $300°C$. [12]

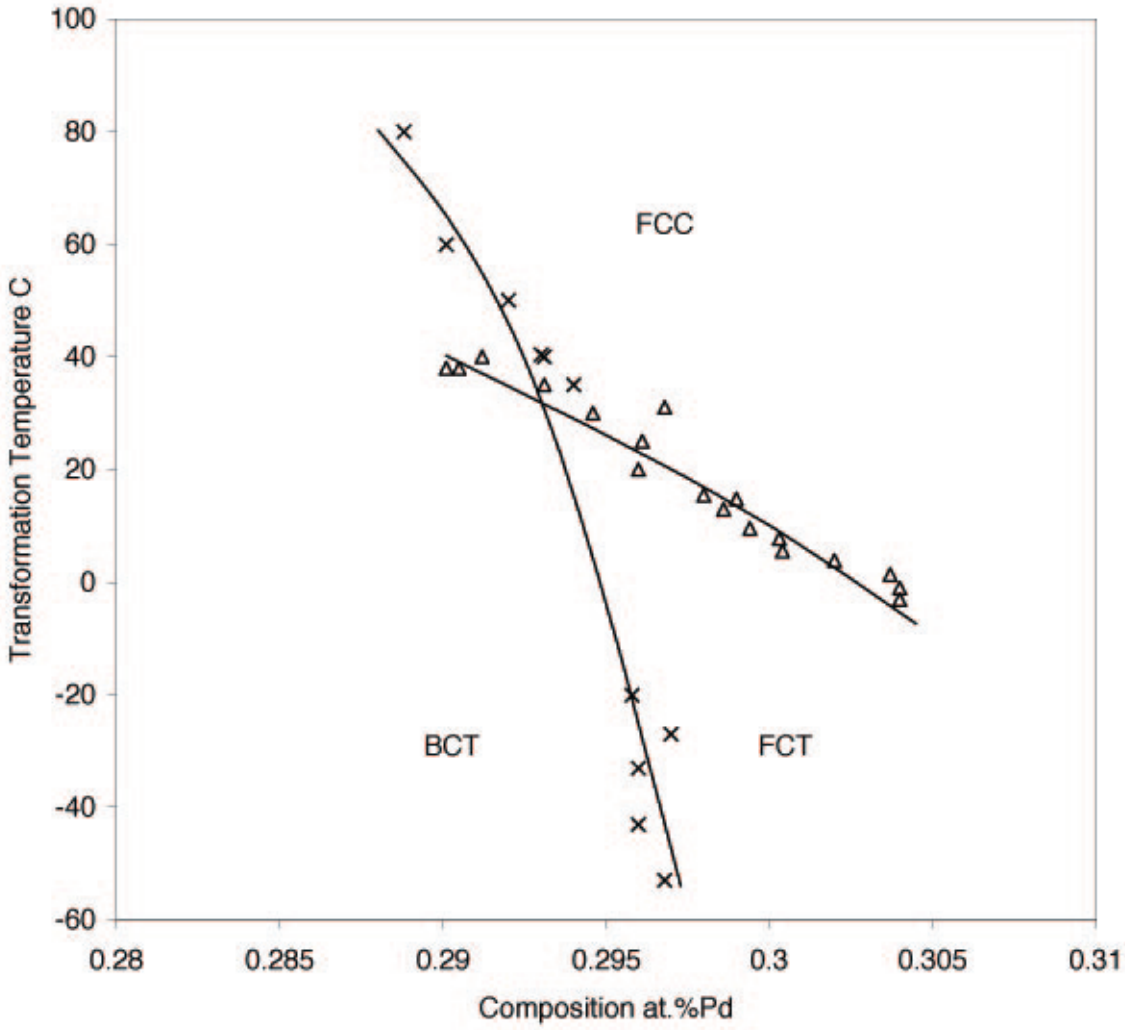

Figure 1.14: Phase transformation temperature as function of palladium concentration. [12]

γ-(Fe, Pd)		γ_1-FePd			γ_2-$FePd_3$	
At.%Pd	a (Å)	At.%Pd	a (Å)	c/a	At.%Pd	a (Å)
30	3.770	48	3.87	0.95	65	3.837
40	3.781	52	3.88	0.95	67	3.840
48	3.800	58	3.88	0.96	70	3.845
52	3.800	60	3.88	0.96	75	3.853
58	3.821					
60	3.826					
70	3.845					
75	3.853					
80	3.859					
85	3.867					

Table 1.4: Lattice parameters of the phases in Fe-Pd Alloy System[47]

Ferromagnetic shape memory alloys are currently studied for possible applications of actuation controlled by magnetic field. One application focuses on the martensitic variants rearrangement induced by an external magnetic field, as mentioned in the previous discussion. The other utilizes the forward and reverse martensitic transformation controlled by the magnetic field. The following discussion is concerned with the latter subject. Figure 1.15 depicts a case close to actual transformation, which has a temperature range of the transformation and hysteresis. The definition of the solid and dotted line in Fe-30.5% is that the solid line refers to an applied magnetic field whereas the dotted line to the state without magnetic field. This is consistent with the magnetization of the alloy in austenite and martensite.[36] Austenite is more stable under a magnetic field. To conduct a simple examination, the amount of the forward and reverse transformation is assumed to linearly depend on temperature change from the start of forward or reverse transformation. If an alloy belongs to category (a), the reversible magnetic actuation is possible. If an alloy has the transformation characteristic of (b), the reversible magnetic actuation is not achieved. FePd belongs to case (a), thus the

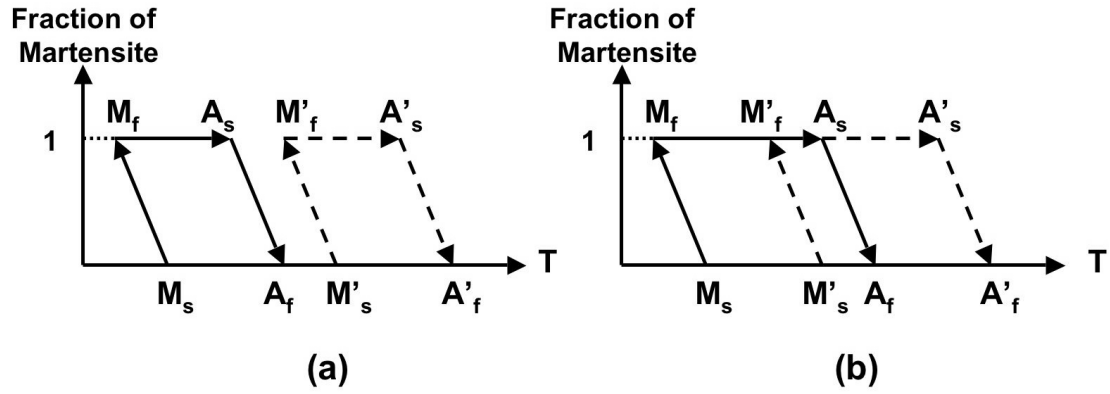

Figure 1.15: Schematically shows the relation between martensite fraction and temperature. (a) No overlapping case where reversible actuation is possible between A_s and M'_f and (b) overlapping case where reversible actuation is not possible. [36]

reversible magnetic actuation is achievable with properly selected compositions.

Figure 1.16 shows that Fe-30.5% Pd belongs to the category described by Figure 1.15(a). When a specimen was slowly heated under no magnetic field after the completion of the transformation and the reverse transformation partially progressed as shown in Figure 1.16(a), a magnetic field of 1T was applied at 2°C. Then some martensite plates disappeared as shown in Figure 1.16(b). When the field was removed, the same martensite plates reappeared as in (a). The reversible change between Figure 1.16(a) and (b) was confirmed by Liang etc. [36]

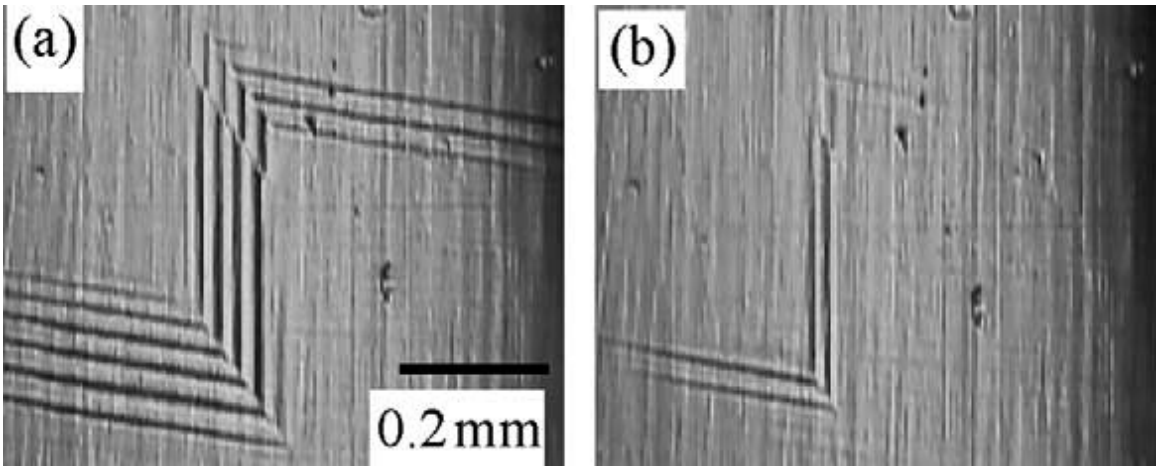

Figure 1.16: Metallographic observation of magnetic field-induced reverse transformation (martensite to austenite) in Fe-30.5% Pd at 2°C. (a) martensite plates under no magnetic field. (b) Some pleats disappear when a field of 1 T was applied [36]

Chapter 2

Elastic Constants And The Experimental Method

2.1 Elastic Constants

Elastic properties govern the behavior of a material subjected to stress over a region of strain where the materials behave reversibly. A solid material changes its shape when subjected to stress. Provided the stress is below the elastic limit, the strain is recoverable. The body returns to its original shape when the stress is removed. Hooke's law states that for sufficiently small stresses the amount of strain is directly proportional to the applied stress, so that the strain components are linear functions of the stress components as Equation (2.1). The proportionality constant relating stress and strain in the region of elastic behavior is the elastic constant, C_{ij}.

$$\sigma_i = \sum_{i,j=1}^{6} C_{ij}\epsilon_j \tag{2.1}$$

where σ is the stress and ϵ is the strain. There are three conditions defining ideal elastic behavior, which are implicit in Equation (2.1): (a) that the strain response

to each level of applied stress (or vice verse) has a unique equilibrium value; (b) that the equilibrium response is achieved instantaneously; (c) that the response is linear. There are six equations as when Equation (2.1) written in expanded form, which results in a 6×6 C_{ij} matrix. In this thesis, the work was conducted with cubic and tetragonal crystals. These two simplified matrices take the form as listed below.

$$\underbrace{\begin{pmatrix} C_{11} & C_{12} & C_{12} & 0 & 0 & 0 \\ & C_{11} & C_{12} & 0 & 0 & 0 \\ & & C_{11} & 0 & 0 & 0 \\ & & & C_{44} & 0 & 0 \\ & & & & C_{44} & 0 \\ & & & & & C_{44} \end{pmatrix}}_{(Cubic)}, \quad \underbrace{\begin{pmatrix} C_{11} & C_{12} & C_{13} & 0 & 0 & 0 \\ & C_{11} & C_{13} & 0 & 0 & 0 \\ & & C_{33} & 0 & 0 & 0 \\ & & & C_{44} & 0 & 0 \\ & & & & C_{44} & 0 \\ & & & & & C_{66} \end{pmatrix}}_{(Tetragonal)} \tag{2.2}$$

Still further simplifications of Hooke's law for crystals can be effected if, instead of the usual components of stress and strain, six independent linear combinations of the usual components were chosen, which possess certain fundamental symmetry properties associated with the crystal in question. These linear combinations, which are known as symmetry coordinates of stress or stain, or as symmetrized stress and strain, are obtained by means of group theory [42].

The complete matrices of symmetrized elastic constants and compliances for the cubic and tetragonal are listed below.

$$\left.\begin{aligned} C_{11} &= \tfrac{S_{11}+S_{12}}{(S_{11}-S_{12})(S_{11}+2S_{12})} \\ C_{12} &= \tfrac{S_{12}}{(S_{11}-S_{12})(S_{11}+2S_{12})} \\ C_{44} &= \tfrac{1}{S_{44}} \end{aligned}\right\} \Rightarrow \begin{pmatrix} \frac{1}{3}(C_{11}+2C_{12}) & & \\ & \frac{1}{2}(C_{11}-C_{12}) & \\ & & C_{44} \end{pmatrix} \tag{2.3}$$

$$\left.\begin{array}{ll} C_{11}+C_{12}=\frac{S_{33}}{S_{33}(S_{11}+S_{12})-2S_{13}^2}, & C_{44}=\frac{1}{S_{44}} \\ C_{13}=\frac{S_{13}}{S_{33}(S_{11}+S_{12})-S_{13}^2}, & C_{11}-C_{12}=\frac{1}{(S_{11}-S_{12})} \\ C_{33}=\frac{(S_{11}+S_{12})}{S_{33}(S_{11}+S_{12})-2S_{13}^2}, & C_{66}=\frac{1}{S_{66}} \end{array}\right\} \Rightarrow$$

$$\begin{pmatrix} C_{11}+C_{12} & \sqrt{2}C_{13} & & & & \\ \sqrt{2}C_{13} & C_{33} & & & & \\ & & C_{11}-C_{12} & & & \\ & & & C_{66} & & \\ & & & & C_{44} & \end{pmatrix} \tag{2.4}$$

The main purpose of this thesis work is to investigate the elasticity of ferromagnetic shape memory alloys. Elasticity always relates to the intrinsic properties of the materials. An accurate and proper method to study the elasticity is very important. Ultrasonic measurements determined the elastic constants of single crystals by using the Ultrasonic Continuous Wave (UCW) technique.[16]

2.2 Experimental Technique

The ultrasonic continuous wave (UCW) method is one of the most versatile modulus measurements and nondestructive evaluation techniques available. It is applicable to a wide variety of materials and environments. The physics and technology of ultrasonic measurements and testings, which were used for basic research or routine materials characterization, have always required more than a little sophistication in their instruments and procedures. The UCW technique is certainly an easier method of making such measurements.

In 1936, Quimby used continuous wave resonance technique to measure Young's

moduli and torsion moduli of cylindrical rods of single crystals at low frequencies, of 100kc [52]. Bolef in 1960 [1] described the UCW resonance technique for measurement of the velocity of sound in solids. Bolef also discussed the calculation of the correction, which is due to the presence of the transducer and coupling film. In 1999, Haluska, et. al., studied the elastic constants of C_{60} near its T_C by the UCW technique.[22]

The advantages of the UCW technique made it to be one of the most important ultrasound measurements methods. The most important advantage of this technique is the good accuracy. Since the measurements use continuous waves the correction factor for end effects can easily be calculated. The factors in the correction terms involve only the length and density of the specimen, coupling film, and transducers. All of the quantities in the corrected expression for the velocity of sound can be measured to better than one part in 10^3 [1]. Therefore, the over all accuracy of the continuous wave method is comparable to the best methods now available. Another very important advantage to use ultrasonic method is that ultrasonic vibrations can be produced in any sort of materials, and they are convenient to process with a various external fields, as temperature field, magnetic field or stress field, et al., which is very hard to achieve by other methods. In addition, it has the virtue of simplicity in instrumentation.

In an anisotropic medium there are only certain directions along which elastic waves can propagate in pure longitudinal and transverse modes. It is desirable to know these modes. Brugger, in 1965, determined the pure modes for all crystal point groups belonging to the orthorhombic, tetragonal, cubic, rhombohedral, and hexagonal systems. [4].

2.2.1 Elastic Wave Modes in Crystals

The purpose of this work is to determine the different elastic constants of the ferromagnetic shape memory materials by measuring the velocities of different elastic wave modes. The structures of the crystals are mainly cubic or tetragonal in our work. Therefore the following discusses details of the elastic wave modes corresponding to the elastic constants of cubic and tetragonal single crystals.

In an anisotropic medium small amplitude elastic plane waves can propagate along a given direction in three distinct, mutually orthogonal modes. These modes are generally neither longitudinal nor transverse. The knowledge of these special directions and modes is very important for the determination elastic coefficients from sound velocity measurements in a crystalline media. A complete discussion of the pure mode directions of the point groups belonging to the orthorhombic, tetragonal, cubic, rhombohedral, and hexagonal system is provided by Brugger [4]. This thesis work mainly concerns the crystalline structures of Ni_2MnGa and FePd, which are mostly cubic and tetragonal. Cuboidal samples have four $< 110 >$ normal faces and two $< 100 >$ normal faces. This orientation ensures enough wave modes to determine all the independent elastic constants in cubic and tetragonal crystals. Table 2.1 and Table 2.2 list all the elastic wave modes in the cubic and tetragonal phases, including the relationship between the wave propagation and polarization directions. The quantities $\hat{H}$, $\hat{W}$, $\hat{P}$, denote the magnetic field, wave propagation and wave polarization directions, respectively. Figure 2.1 shows the applicable effective elastic constants for the three modes of elastic waves in the principal propagation directions in cubic crystals.

Because the crystalline orientation of the samples is four $< 110 >$ normal faces and two $< 100 >$ normal faces, not all the elastic wave modes are practicable,

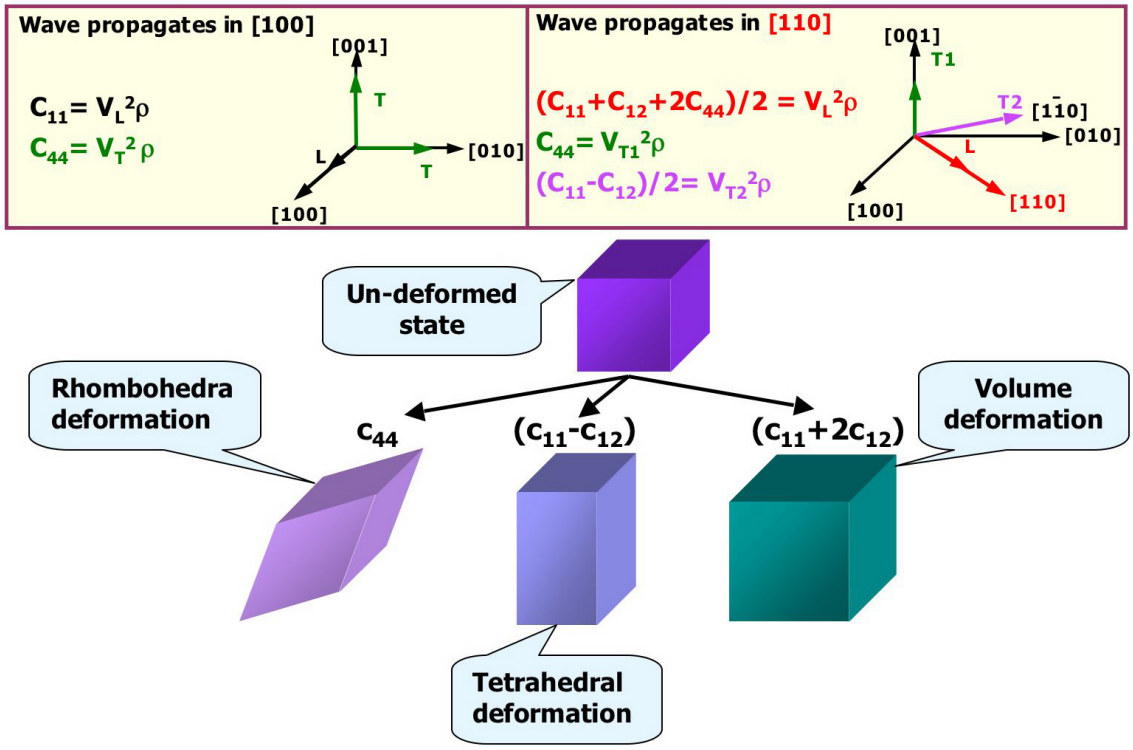

Figure 2.1: Effective elastic constants for the three modes of elastic waves in the principal propagation directions in cubic crystals. The two transverse modes are degenerate for propagation in the [100] and [111] directions(K: wave vector; L: longitudinal wave; T: transverse wave) [32]

Modes	$\hat{\mathrm{W}}$	$\hat{\mathrm{P}}$	Elastic Constants: $C = \rho V^2$
L	[100]	[100]	C_{11}
T		[001], [010]	C_{44}
L	[110]	[110]	$\frac{C_{11}+C_{12}+2C_{44}}{2}$
T_1		[001]	C_{44}
T_2		$[1\bar{1}0]$, [010]	$\frac{C_{11}-C_{12}}{2}$
L	[111]	[111]	$\frac{C_{11}+2C_{12}+4C_{44}}{3}$
T		$[11\bar{1}]$, $[1\bar{1}0]$	$\frac{C_{11}-C_{12}+C_{44}}{3}$

Table 2.1: Elastic wave modes in cubic crystal. The wave propagation and polarization directions are represented by $\hat{\mathrm{W}}$ and $\hat{\mathrm{P}}$, respectively. The L and T denote the longitudinal wave and transverse wave mode, respectively.

especially the waves propagating along $< 111 >$ could not be studied. There are five wave modes for determining the three independent elastic constants in cubic and eleven wave modes for determining the six independent elastic constants in tetragonal as shown in Table 2.1 and 2.2. Moreover there are different wave modes to determine the same elastic constants, C_{44}. The elastic constants could thus be and were checked self consistently. Therefore the elastic constants in both cubic and tetragonal systems are over-determined.

The key to conducting the measurements of elastic constants in tetragonal martensitic phase is to obtain martensitic single variants. In our experiments, we use an external magnetic field to bias the FSMA samples into their various single variant states. The magnetic easy axis of Ni_2MnGa is on the short axis as shown in Figure 1.9 [57]. Thus after applying saturation magnetic field, the [001] direction of the specimen, the short axis, will align with the direction of the external magnetic

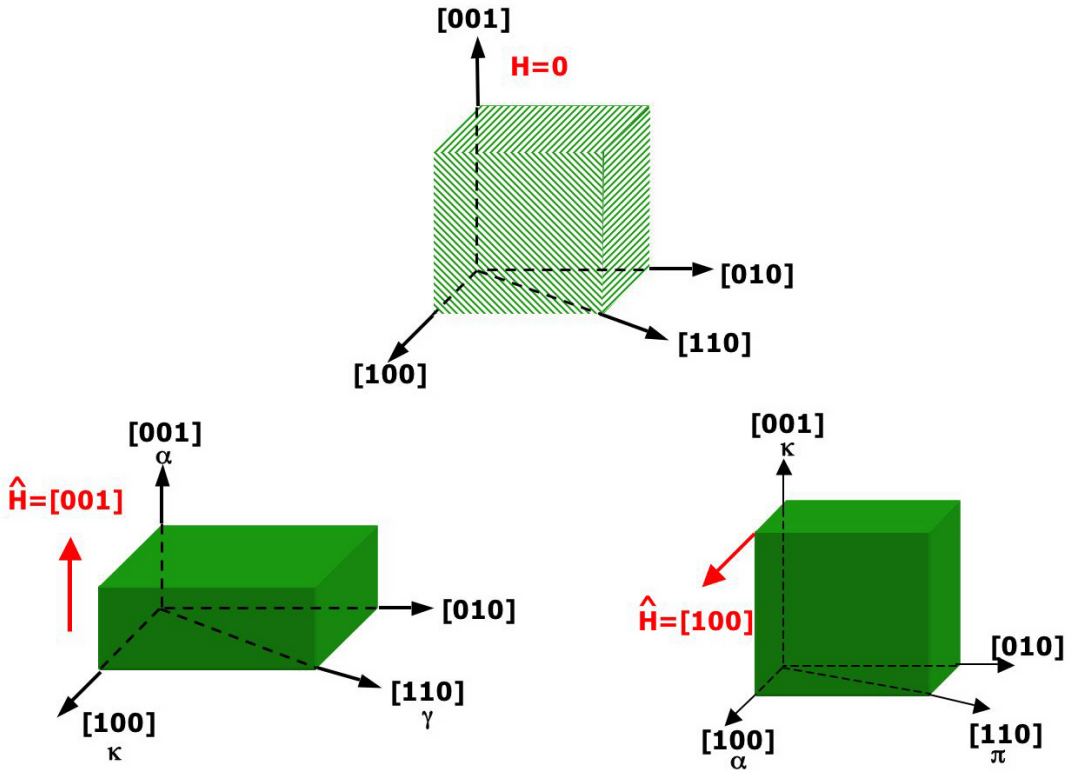

Figure 2.2: Magnetic field de-twinned the martensitic Ni_2MnGa to obtain single variant tetragonal martensite with c/a<1.

field. By changing the direction of the magnetic field, the sample can switch from one variant to other as shown in Figure 2.2, such that a sound wave can travel along different directions and various modes can be realized. The detail of all the available elastic wave modes are depicted in Figure 2.3 and listed in Table 2.2.

In tetragonal crystals there are eleven of fourteen wave modes for determining the six independent elastic constants with the orientation of the sample. Moreover there are three different wave modes to conduct the same elastic constants, C_{44}. The elastic constants were also checked self consistently in tetragonal system.

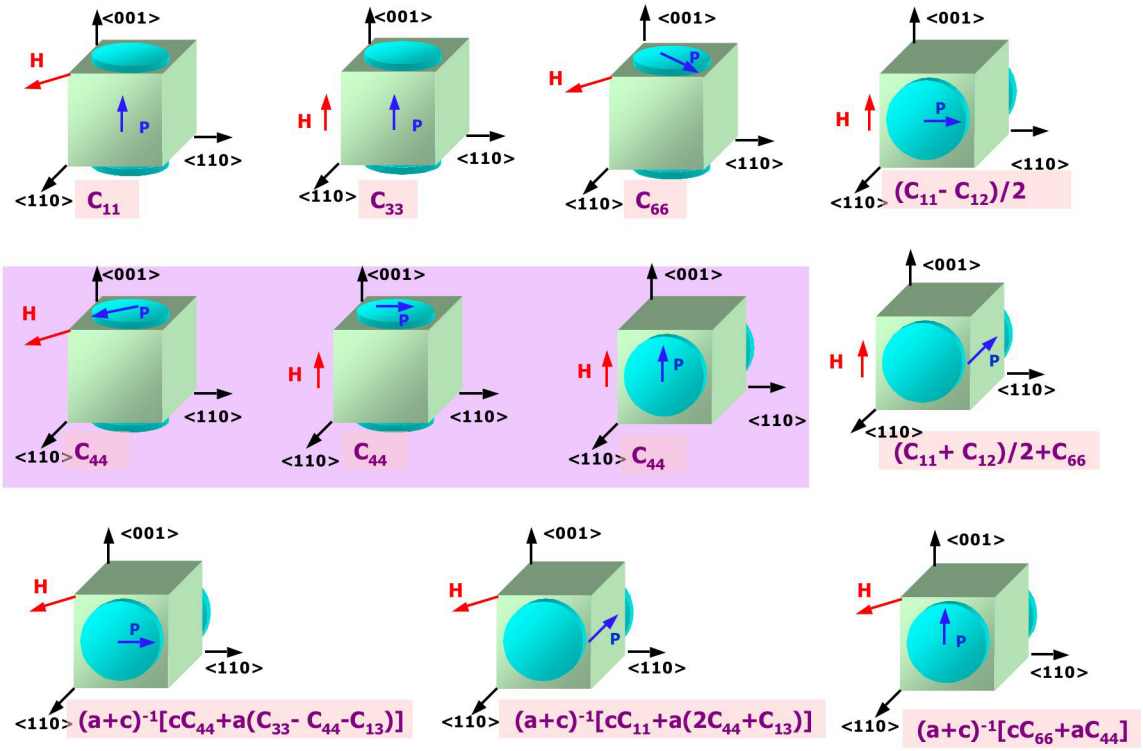

Figure 2.3: All the applicable elastic wave modes in the tetragonal phase. H and P present the magnetic field direction and wave polarization direction, respectively. The wave propagation direction is along the directions normal to the faces of transducers.

Modes	$\hat{\mathrm{H}}$	$\hat{\mathrm{P}}$	$\hat{\mathrm{W}}$	Elastic Constants: $C = \rho V^2$
L	[001]	[001]	[001]	C_{33}
T		[100]		C_{44}
L	[001]	[111]	[111]	$\frac{c(C_{11}+2C_{66}+C_{12})+(2a-b)(2C_{44}+C_{13})}{2a-b+2c}$
T_1		$[1\bar{1}0]$		$\frac{c(C_{11}-C_{12})+(2a-b)C_{44}}{2a-b+2c}$
T_2		[101]		$\frac{2cC_{44}+(2a-b)(C_{33}-C_{44}-C_{13})}{2a-b+2c}$
L	[100]	[110]	[110]	$[cC_{11}+a(2C_{44}+C_{13})]/(a+c)$
T_1		[001]		$[cC_{66}+aC_{44}]/(a+c)$
T_2		$[1\bar{1}0]$		$C^* = (cC_{44}+a(C_{33}-C_{44}-C_{13}))(a+c)$
L	[001]	[110]	[110]	$(C_{11}+2C_{66}+C_{12})/2$
T_1		$[1\bar{1}0]$		$C' = (C_{11}-C_{12})/2$
T_2		[001]		C_{44}
L	[100]	[001]	[001]	C_{11}
T_1		[010]		C_{66}
T_2		[100]		C_{44}
$a = C_{11}-2C_{44}-C_{13}; b = C_{11}-2C_{66}-C_{12}; c = C_{33}-2C_{44}-C_{12}$				

Table 2.2: Elastic wave modes in tetragonal crystal. The magnetic field, wave propagation and polarization directions are represented by $\hat{\mathrm{H}}$, $\hat{\mathrm{W}}$ and $\hat{\mathrm{P}}$, respectively. The L and T denote the longitudinal wave and transverse wave modes. The a, b and c are three constant coefficients, which are different combinations of elastic constants as shown in the table. They equal to each other in cubic crystal which yields the Table 2.1

2.2.2 Principle of Ultrasonic Continuous Wave Technique

A sound wave is the motion of material in response to a periodically varying force. The speed with which it travels is related to the speed with which the atoms in the material are able to move back and forth in response to an applied force. This depends on the elastic constants, which indicate the stiffness of the material, the density of the atoms, and the type of sound wave being propagated. The elastic constants were determined from the measurements of the velocity of sound in the single crystals by an ultrasonic continuous wave resonance technique:

$$C = V^2 \times \rho \tag{2.5}$$

where V represents the sound wave velocity and ρ means the sample density and C is the elastic constant. This technique depends upon setting up standing waves in a composite oscillator consisting of transducers, coupling film, and specimen, which is shown in the cartoon of Figure 2.4. The velocity is then obtained in terms of length, density, and frequency.

The sound velocity is the product of the wave frequency and wavelength as:

$$V_n = \nu_n \times \lambda_n \tag{2.6}$$

where, V_n, ν_n and λ_n are the velocity, the frequency and wave length of the nth order harmonic wave, respectively.

The wave length of the nth order harmonic wave is related to the sample length and the order level as shown in Figure 2.4.

$$\lambda_n = 2l_s/n, \tag{2.7}$$

where l_s is the samples length. Substitute Equation (2.7) into the Equation (2.6) to get the relation of the velocity, sample's length, harmonic order and resonant

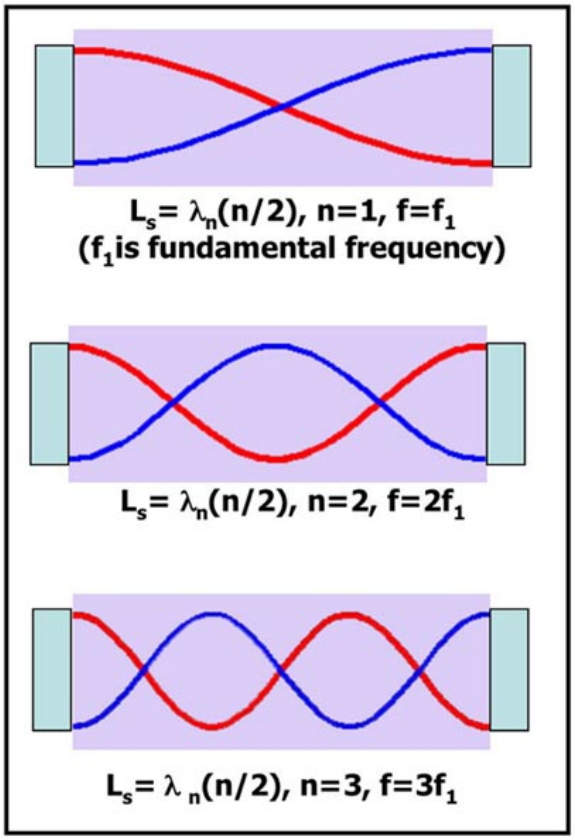

Figure 2.4: Cartoon shows the different harmonic order standing waves

frequency :

$$V_n = \nu_n \frac{2l_s}{n} \quad (a)$$
$$V_{n+1} = \nu_{n+1} \frac{2l_s}{n+1} \quad (b) \tag{2.8}$$

The wave velocity is unique with different harmonic orders, yielding $V_n = V_{n+1}$. Then the frequency can be written as the function of the different resonant frequencies between two adjacent harmonic waves, $\Delta\nu$, as:

$$\Delta\nu = \frac{\nu_n}{n} \tag{2.9}$$

Substitute Equation (2.9) into Equation (2.8) (a), the velocity of the wave can be presented as:

$$V_n = 2l_s \times \Delta\nu \tag{2.10}$$

The waves velocity can be converted into elastic constants by substituting Equation (2.10) as:

$$C = V_n^2 \times \rho = (2l_s \times \Delta\nu)^2 \times \rho \tag{2.11}$$

Above all, the experimental principle of determining elastic constants using continuous wave method is two-fold. First, velocity of the sound wave is the product of samples length and the difference of the two adjacent natural frequencies of harmonic standing waves; second, elastic constant is the product of the square of the velocity of sound waves and density of the specimen. Therefore, to measure elastic constants is to measure the different resonant frequency between the adjacent harmonic standing waves of different elastic wave modes.

2.2.3 Experimental Set Up and Arrangement

The elastic constants of FSMA are determined applying a ultrasonic continuous wave method by measuring the velocities of different elastic waves modes. The

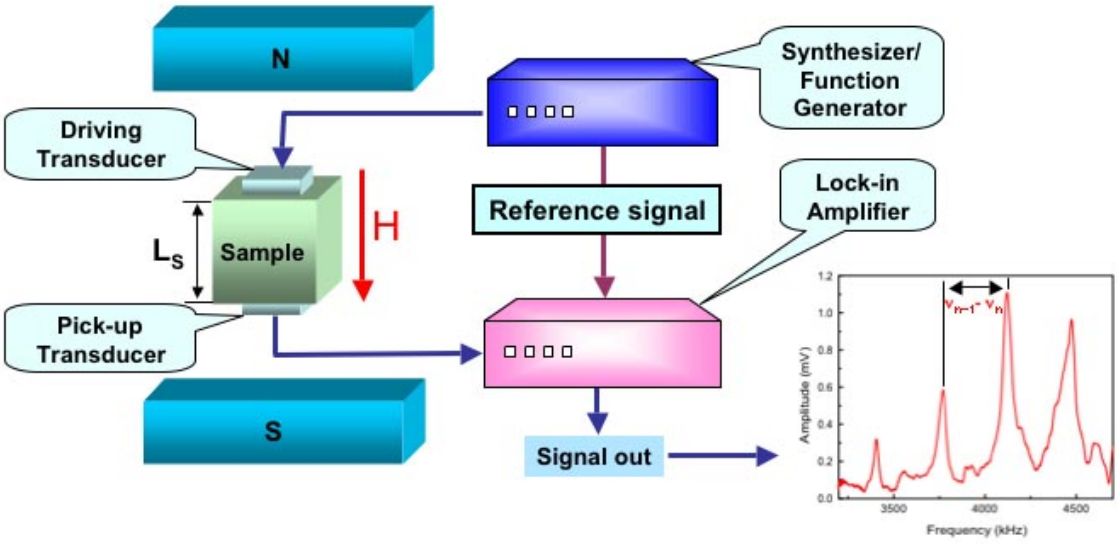

Figure 2.5: Experimental set up of the continuous ultrasonic wave technique

experimental setup is schematically shown in Figure 2.5. An electro-magnet is used to bias the specimen into different single variant states. The function generator and lock-in amplifier represent the electronics to generate and analyze sound wave signals through the transducers. Commercially available PZT based pressure and shear transducers with a resonance frequency of 1.5MHz are coupled to the samples. They are used to generate and detect the desired standing waves. A thin layer of vacuum grease is applied between the sample and the transducers for better connection. In addition, a 2mm thick rubber bands were fitted in the spaces between the transducers and the sample holder for applying proper pressure. The vacuum grease and rubber band were used to improve the coupling between the transducers and sample. This arrangement allows to make the measurements over a range of temperatures including those, in which large deformations are expected. A picture of the sample holder is shown as Figure 2.6. According to the experimental principle, an automatic system was designed to measure the elastic constants. It

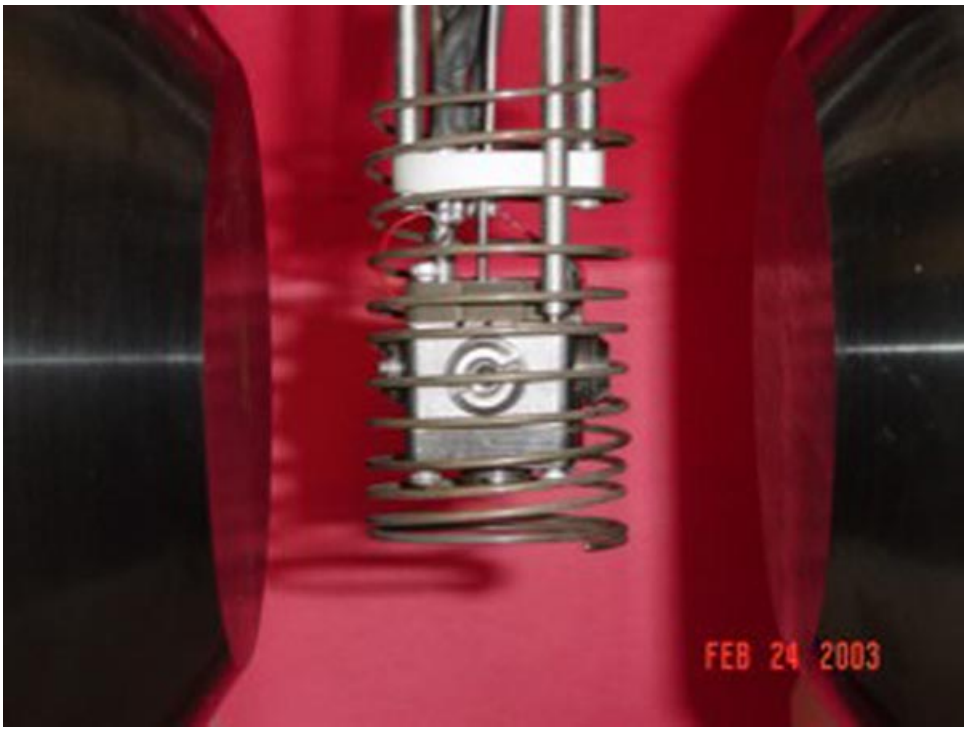

Figure 2.6: Sample holder of the experimental set up of the continuous ultrasonic wave technique.

is shown in Figure 2.6 and Figure 2.7. The system is automatically controlled by a Labview program. The platform of this program is shown in Figure 2.7.

This chapter represents the experimental principle of ultrasonic continuous wave technique. It described the automatic system for measuring the elastic constants by UCW technique with applicable external fields. The following chapters discuss the elasticity study of ferromagnetic shape memory alloys, Ni_2MnGa and Fe_3Pd, by this experimental method.

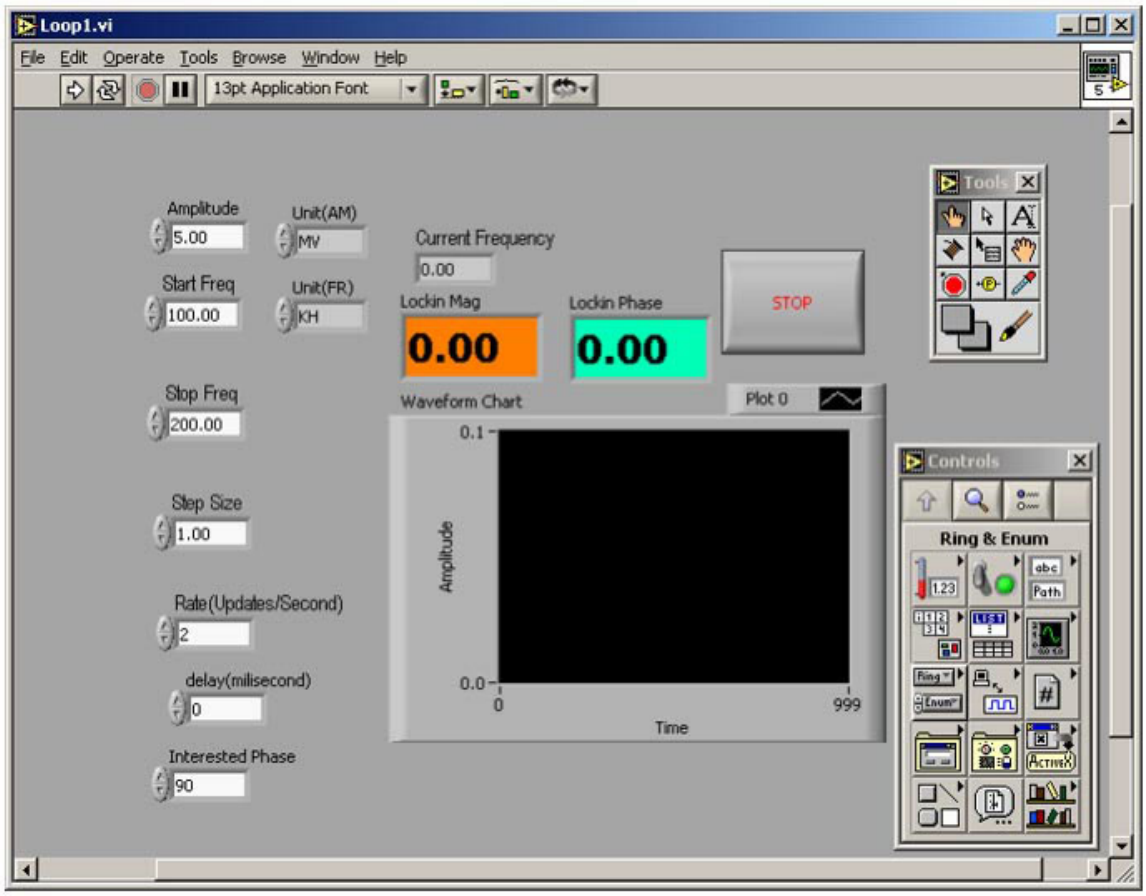

Figure 2.7: Labview program for automatically controlling measurement process.

Chapter 3

Elasticity of Ni_2MnGa

Ferromagnetic shape memory alloy Ni_2MnGa has a large magnetic field induced strain, which results in a large shape change. The elastic energy is a crucial parameter for this effect. The main purpose of this work is to study the elasticity of the FSMA, especially the temperature dependence of elastic constants. The dependence of a solid's elastic properties on temperature in the vicinity of a structural transformation provides the nature of the transition and has been the focus of many studies.

3.1 Sample Description

The present experiments were conducted with Ni_2MnGa single crystals, which were prepared at Adaptive Materials Technology Ltd. (Yritysiha 5, FIN-00390 Helsinki, Finland) Two samples, $Ni_{0.5}Mn_{0.284}Ga_{0.216}$ and $Ni_{0.49}Mn_{0.234}Ga_{0.276}$, were studied. The cuboidal samples, 10mm long on each side, are oriented so that four opposing faces have a $\langle 110 \rangle$ normal, whereas the other two faces have a $\langle 100 \rangle$ normal. The samples were cut by the company. In the martensitic state of these samples the c-

axis is the easy magnetization axis, which turns to align with the external magnetic field. Pressing the materials with a low load, $2 \sim 3$ MPa reorients the c-axis along the pressing direction. When a martensitic sample of these materials is put with its c-axis perpendicular to the external magnetic flux path, the c-axis reorients to the direction of the field and the sample expands perpendicular to the magnetic field. Both samples have the tetragonal martensitic structure with 0.94 aspect ratio, c/a, and their Curie temperatures are both around 95°C, which are shown by the SQUID (Super-conducting Quantum Interference Device) results as Figure 3.1 and 3.3.

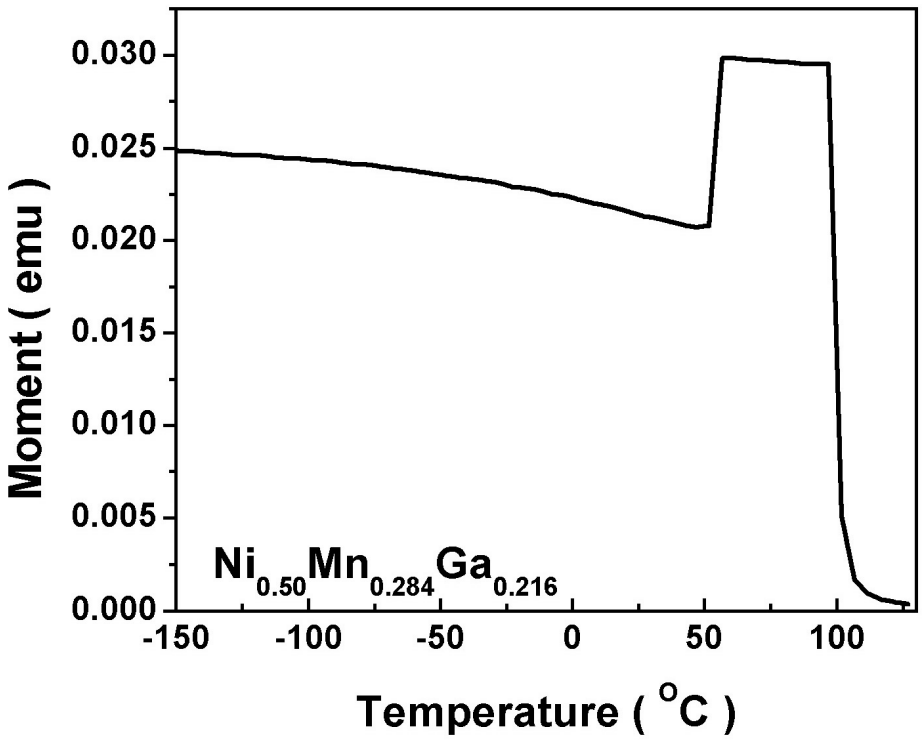

Figure 3.1: SQUID results of $Ni_{0.5}Mn_{0.284}Ga_{0.216}$ clearly show the Curie Temperature is around 95°C and the martensitic transformation temperature is around 42°C.

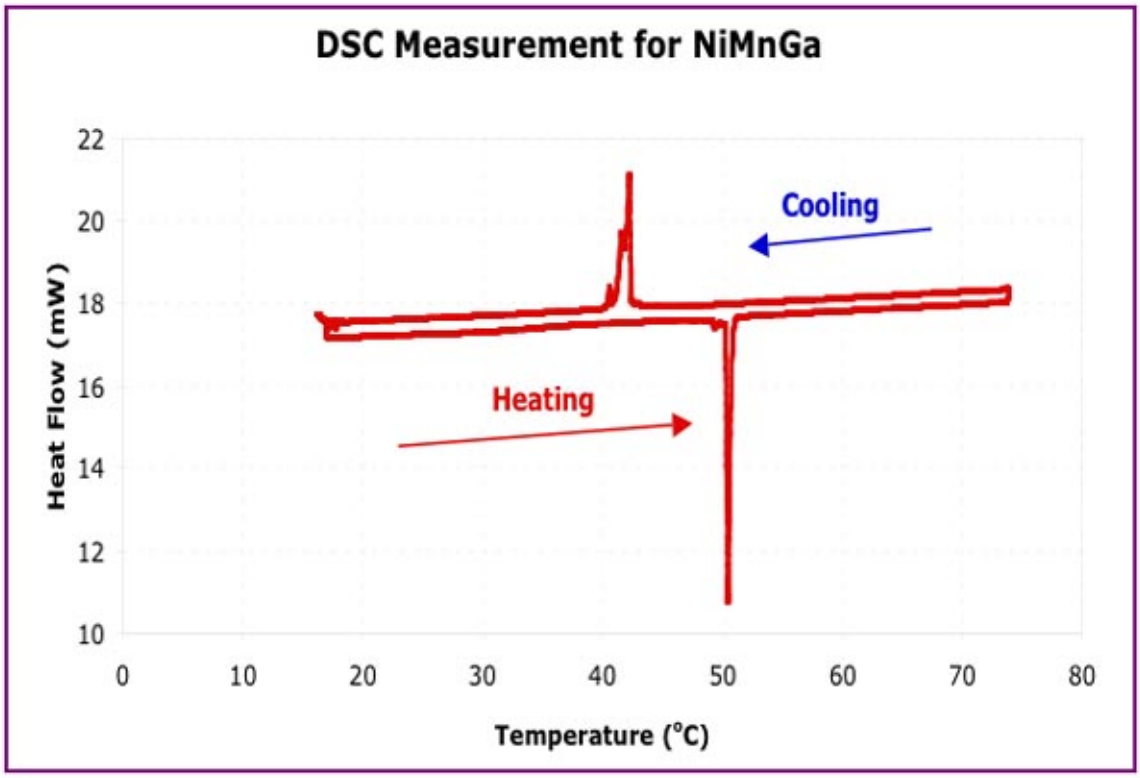

Figure 3.2: DSC measurement of $Ni_{0.50}Mn_{0.284}Ga_{0.216}$

$Ni_{0.5}Mn_{0.284}Ga_{0.216}$ has the martensite start temperature around 42°C. Figure 3.1 depicts the results of the SQUID measurements, which confirmed the magnetic and structural transformation temperatures. Figure 3.2 shows the results of DSC (Differential Scanning Calorimetry) measurements of $Ni_{0.5}Mn_{0.284}Ga_{0.216}$, which indicates the martensitic transformation temperature is around 42°C and Austenitic transformation temperature is around 50°C. $Ni_{0.49}Mn_{0.234}Ga_{0.276}$ has martensite start temperature around 3°C. Figure 3.3 shows the SQUID results, which indicates the martensitic transition temperature and the Curie temperature.

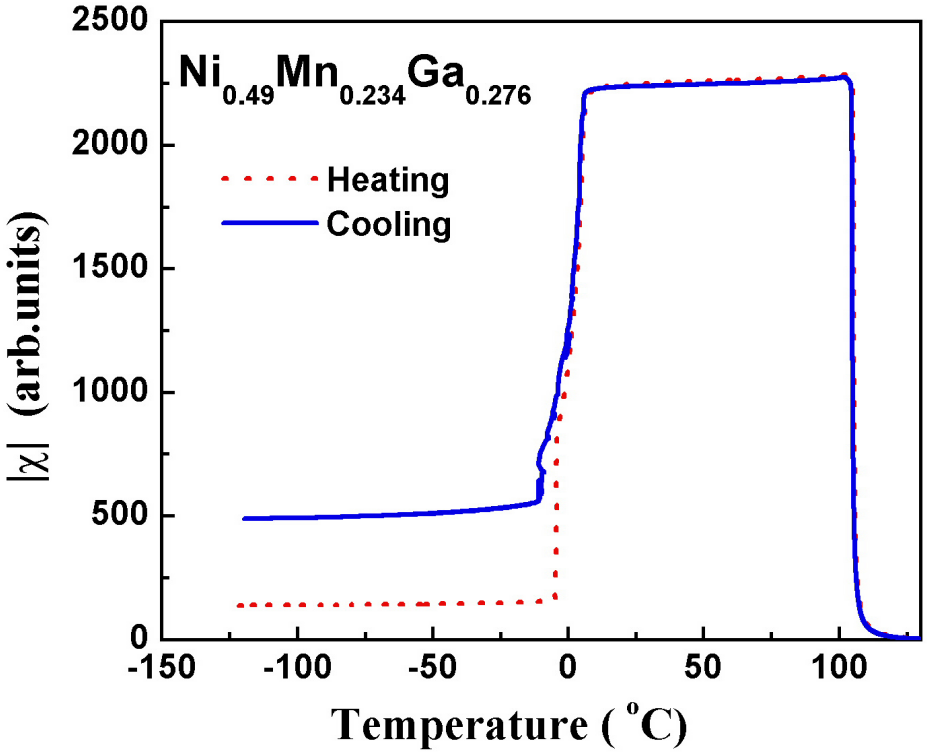

Figure 3.3: SQUID result of $Ni_{0.49}Mn_{0.234}Ga_{0.276}$ clearly shows the Curie temperature is around 95°C and the martensitic transformation temperature is around 3°C.

3.2 Elasticity of Ni_2MnGa in the High Temperature Phase

The high temperature phase in Ni_2MnGa is the austenitic cubic phase. It is often found that one of the shear moduli, most often $C_{11} - C_{12}$, tends to decrease as the martensitic start temperature, M_S, is approached from above, in some cases becoming as small as one or two GPa at the transformation temperature. This softening of the modulus is the result of the tendency of the crystal lattice to transform to a new structure that is obtainable from the austenite by a continuous deformation of

the lattice. In certain NiMnGa alloys, the Martensitic transformation is preceded by a transition that freezes in place a shuffling of atomic planes, with a period of three or more lattice spaces. These transitions can have a significant effect on the elastic constants.

We investigated the elastic constants in high temperature phase of two single crystals, $Ni_{0.50}Mn_{0.284}Ga_{0.216}$ and $Ni_{0.49}Mn_{0.234}Ga_{0.276}$. Anomalies in the temperature dependences of all the constants were observed at below T_C, as well as in the vicinity of M_S. In what follows, we describe our findings and discuss possible interpretations of the anomalous behavior of the elastic constants at and below T_C.

3.2.1 Elastic Constants of $Ni_{0.50}Mn_{0.284}Ga_{0.216}$ High Temperature Phase

This section pertains to the present study of the high temperature phase of $Ni_{0.50}Mn_{0.284}Ga_{0.216}$. The ultrasonic continuous wave method [16, 1, 15] was used to determine the velocities of [100] and[110] longitudinal, and [100][001] (T1) and [110][$1\bar{1}0$](T2) transverse elastic waves, as shown in Figure 2.1. The experimental set up was detailed in Chapter 2. All measurements were conducted in a magnetic field of 0.8T, sufficiently large to create single domain conditions in the austenite. Two different field orientations were used, [001] and [100]. The measurements were taken as the temperature was lowered from 428K down to 268K in the presence of the field.

The results of the temperature dependence of all the elastic constants are depicted in Figure 3.4. Anomalous behavior of the elastic constants was observed, especially an abrupt 15% softening of C_{11} at the Curie temperature, as shown in Figure 3.5. The latter anomaly was found to be strongly influenced by the presence

and orientation of applied magnetic fields.

The measurements described above and exhibited in Figure 3.4 and Figure 3.5 may be summarized as follows: Figure 3.4 shows the temperature dependence of the directly measured elastic constants in austenitic $Ni_{0.50}Mn_{0.284}Ga_{0.216}$. All four elastic constants of the cubic phase of the alloy have been determined from 428K down to and just below the onset of the Martensitic phase transition. The three symmetry constants, $C_{11}+2C_{12}$, C_{11}-C_{12} and C_{44} show anomalous behavior near the Curie temperature, to varying extent. The shear constants undergo changes in slope right at T_C, while the C_{11} shows two very different behaviors in the two magnetic field orientations as shown in Figure 3.5. The softening of C', (C_{11}-C_{12})/2, as the martensitic temperature is approached has been observed in prior studies in other NiMnGa alloys. Similar shear softening phenomena has also been found in other ferromagnetic alloys, such as CoNiGa and NiFeGa [55, 65, 66]. The anomalies in C' and C_{44} are small in comparison with the variation in C_{11} at T_C, as can be seen in Figure 3.4. This combination of behaviors is somewhat similar to that often observed in Invar alloys like Fe-Ni[23, 25] and Fe-Pt[25]. They differ in that in the latter, C' shows the normal increase with decreasing temperature above the Curie point, leading to a maximum at T_C, while in the present study, C' decreases monotonically as the temperature is lowered, showing only a slight inflection at T_C.

The largest effect of the onset of magnetic order occurs in the temperature dependence of C_{11}, which contains both tetragonal shear and volume responses. However, it is the volume contribution that is most strongly effected at T_C. This becomes evident when the bulk modulus is calculated from the measured C_{11} and C_{12}. When the field was parallel to the propagation axis, there was a smooth

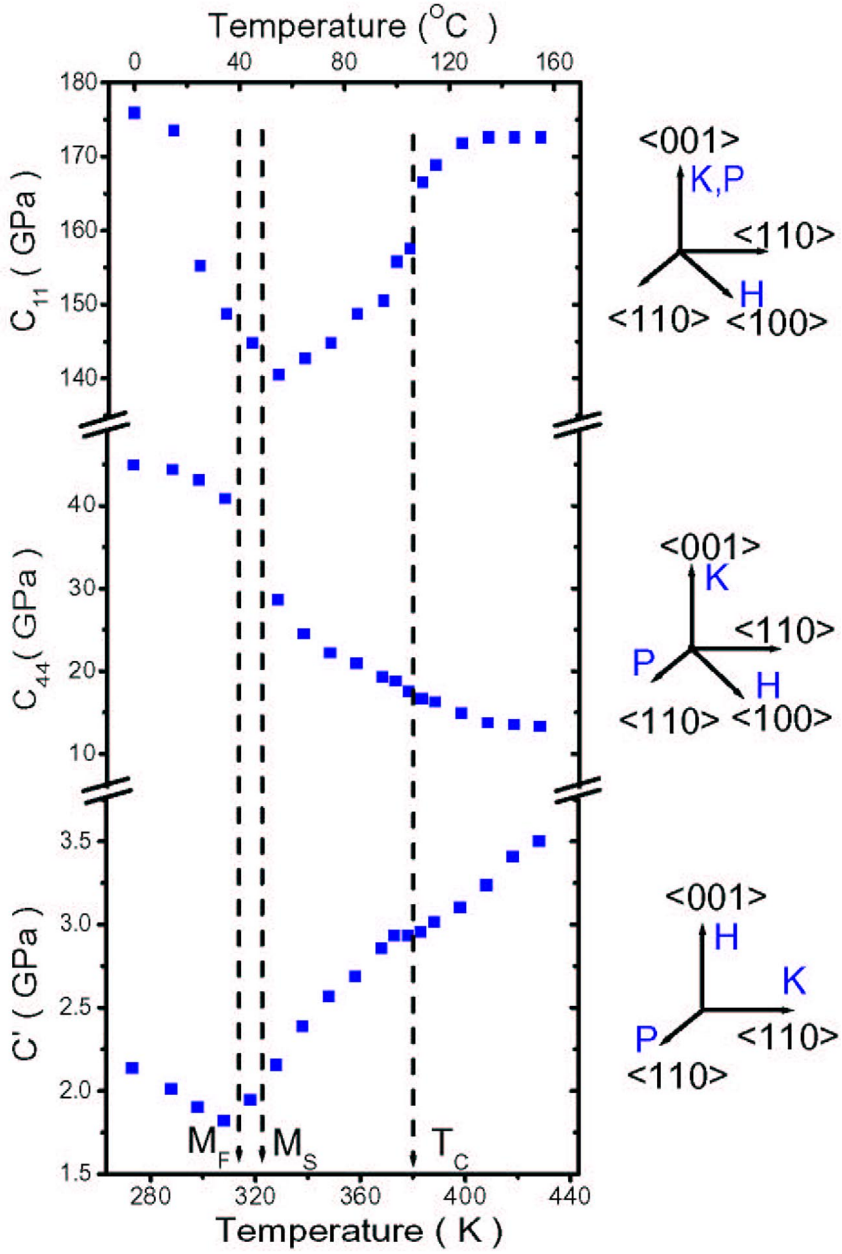

Figure 3.4: The elastic constants, C_{11}, C_{44} and C', of $Ni_{0.50}Mn_{0.284}Ga_{0.216}$ vs. temperature. The propagation and polarization directions used to obtain the data are shown on the right.

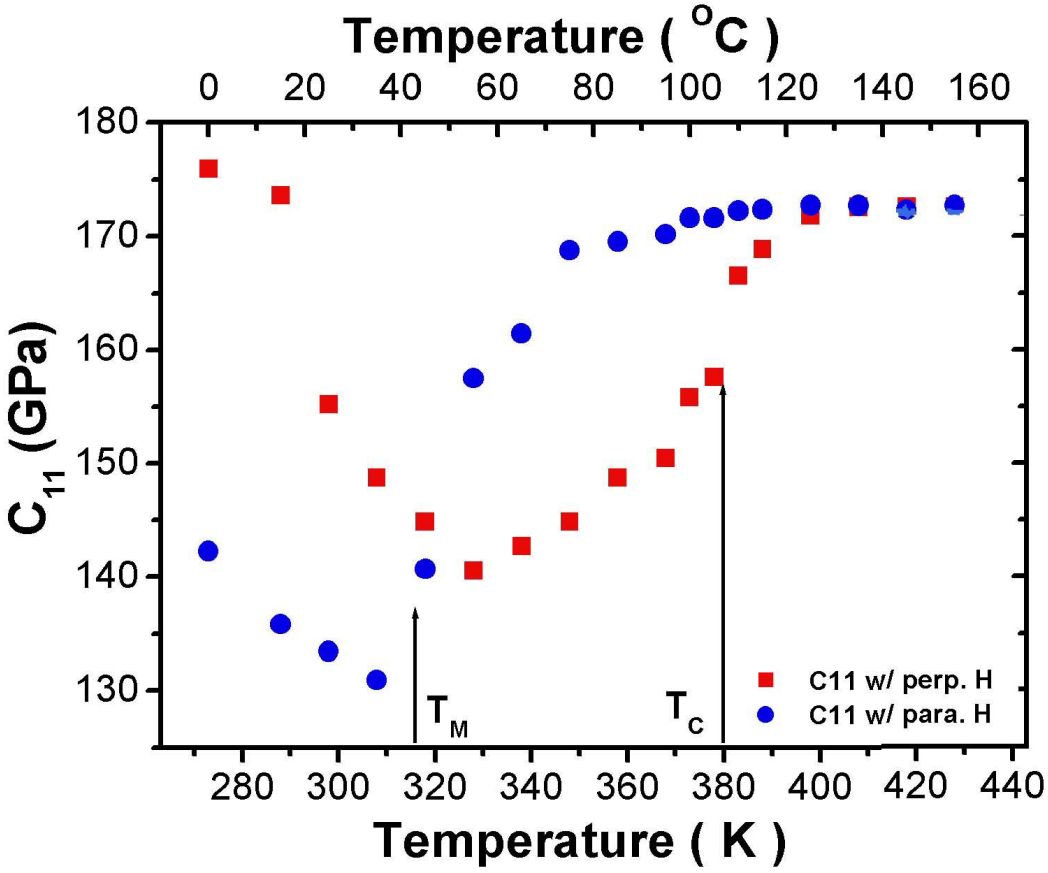

Figure 3.5: The elastic constant, C_{11}, is sensitive to the direction of applied magnetic field: The change of C_{11} is plotted vs. temperature. Measurements were taken with a longitudinal wave along $\langle 001 \rangle$ with applied a 0.8 Tesla magnetic field along $\langle 001 \rangle$ (solid circle) and $\langle 100 \rangle$(solid square).

variation in the bulk modulus through T_C. With the field applied perpendicular to the propagation direction, this modulus drops abruptly at T_C, and continues to decrease until the fall is interrupted at the Martensite temperature, M_S, as shown in Figure 3.5. The latter is similar to the anomalous behavior of the bulk modulus found in some invar alloys, such as FeNi[23, 59, 24, 26, 56], FePt[59, 26], FeMn[23], and MnNiCr [23]. In those alloys, the phenomena were explained as being due to volume magnetostriction. That mechanism, however, cannot explain the dependence on magnetic field orientation observed in our experiments. Instead, the orientation dependence leads us to propose that the Curie point also marks a transition between a cubic and a premartensitic phase, i.e., a modulated phase[7, 6, 56]. The large difference of the C_{11} mode with the field along two different $\langle 100 \rangle$ directions when the temperature was lower than T_C can be accounted for by assuming that the field reorients the modulation direction, in effect creating a tetragonal state. Thus the cubic C_{11} mode splits at the transition into two modes, similar to the splitting observed in that mode at the martensitic transition.

For the purpose of checking the experimental data, $(C_{11} + C_{12} + 2C_{44})$ was obtained from the longitudinal mode velocity for waves propagating along the $\langle 110 \rangle$ direction. The same quantity was also extracted from the data in Figure 3.4 using the equation

$$(C_{11} + C_{12} + 2C_{44}) = 2C_{11} - (C_{11} - C_{12}) + 2C_{44} \tag{3.1}$$

The measured and calculated combination $(C_{11} + C_{12} + 2C_{44})$ agreed within 2% over the entire temperature range of our measurements.

3.2.2 Elastic Constants of $Ni_{0.49}Mn_{0.234}Ga_{0.276}$ High Temperature Phase

The experimental method and set up of the elastic constants in high temperature phase of $Ni_{0.49}Mn_{0.234}Ga_{0.276}$ is similar with $Ni_{0.50}Mn_{0.284}Ga_{0.216}$. This sample has 273K martensitic transformation temperature, which is lower than the 318K of $Ni_{0.50}Mn_{0.284}Ga_{0.216}$. All measurements were conducted in a magnetic field of 0.8T. Two different field orientations were used, [001] and [100]. The measurements were taken as the temperature was lowered from 428K down to room temperature in the presence of the field. The results of the elastic constants of $Ni_{0.49}Mn_{0.234}Ga_{0.276}$ high temperature phase are presented in Figures 3.6, 3.7, 3.8, 3.9.

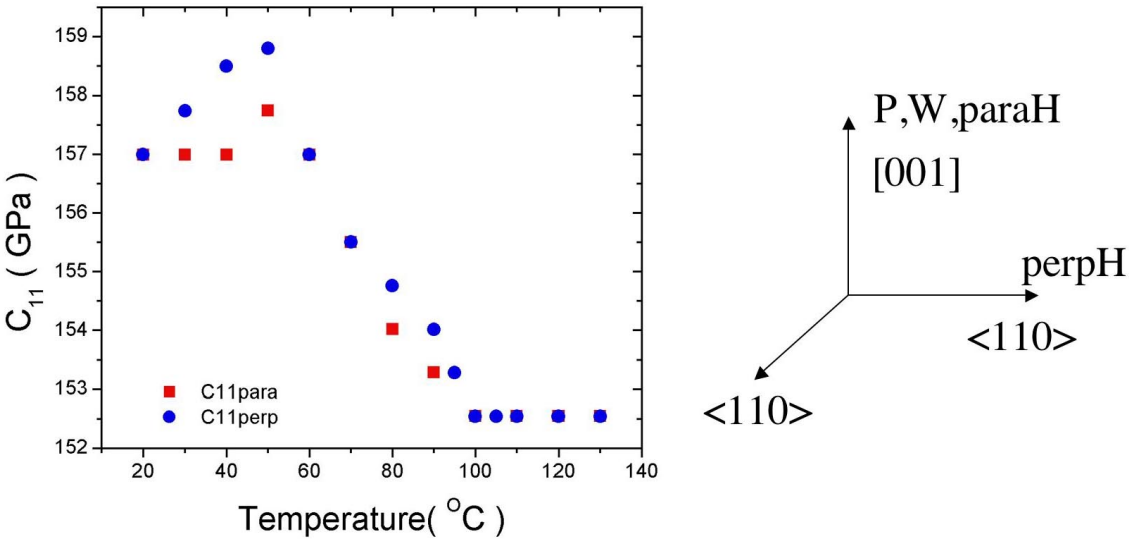

Figure 3.6: C_{11} measured by a longitudinal wave along [001]. The temperature dependence of the C_{11} were studied with magnetic field parallel and perpendicular to the wave propagation direction. This plot clearly shows a premartensitic transition around 60°C.

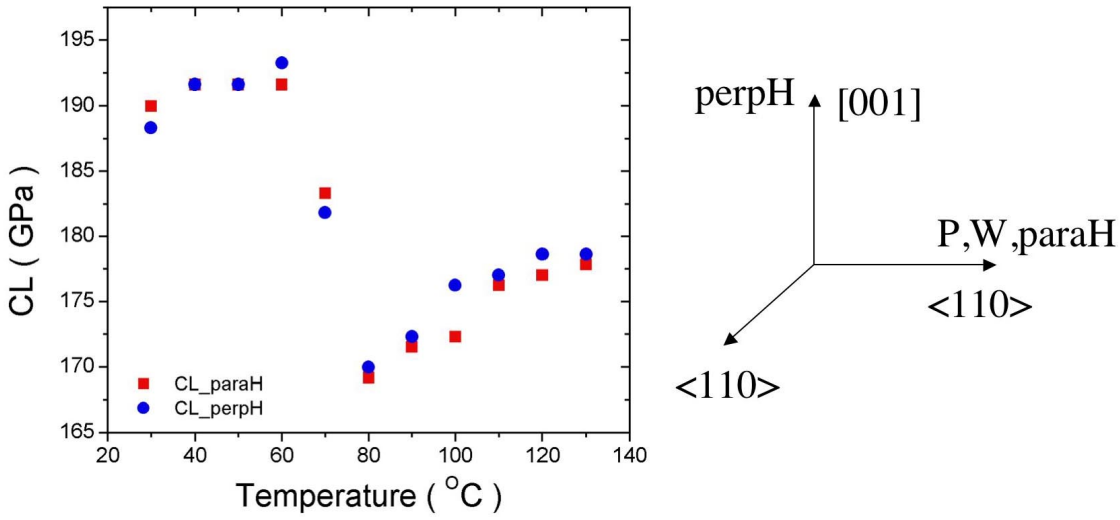

Figure 3.7: C_L measured by a longitudinal wave along $\langle 110 \rangle$. The temperature dependence of the C_L were studied with magnetic field parallel and perpendicular to the wave propagation direction.This plot clearly clearly shows a premartensitic transition around 60°C.

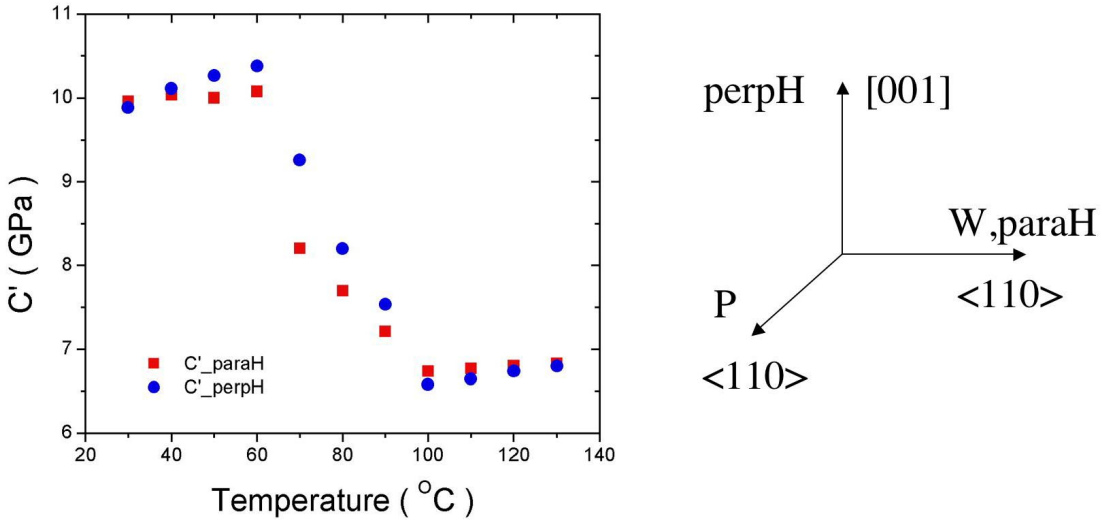

Figure 3.8: C measured by a transverse wave along ⟨110⟩ with ⟨110⟩ polarization direction. The temperature dependence of the C' were studied with magnetic field parallel and perpendicular to the wave propagation direction.This plot clearly clearly shows a premartensitic transition around 60°C.

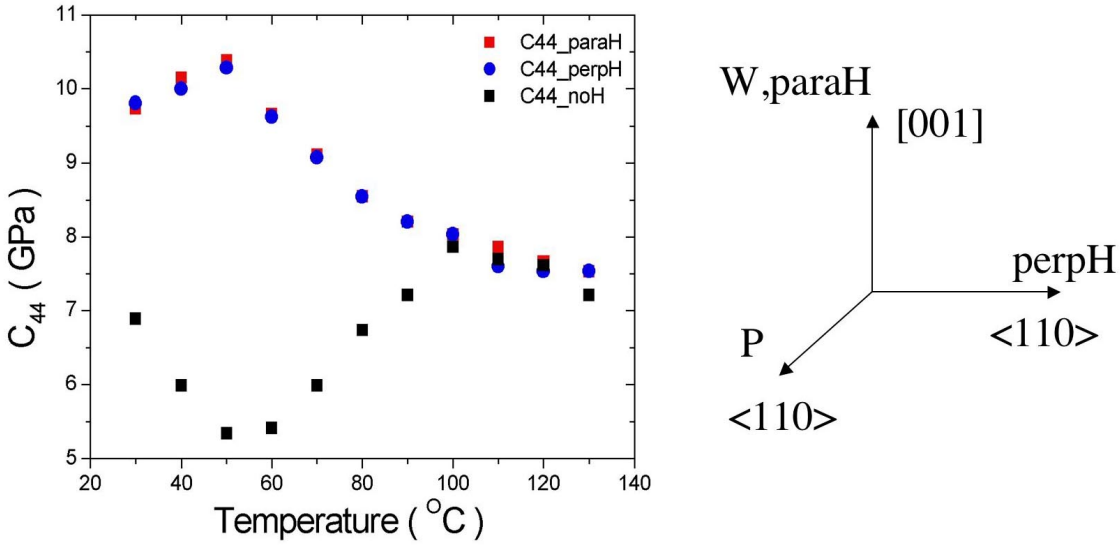

Figure 3.9: C_{44} measured by a transverse wave along [100] with $\langle 110 \rangle$ polarization direction. The temperature dependence of the C_{44} were studied with magnetic field parallel and perpendicular to the wave propagation direction. The temperature dependence of C_{44} has a large different between with and without magnetic field. This plot clearly clearly shows a premartensitic transition around 60°C.

All these results clearly show a premartensitic transition around 60°C. There is almost no change with different orientations of external magnetic field. This discrepancy with our expectation might be caused by the different compositions of samples. The properties of Ni_2MnGa Heusler alloys are sensitive to the composition. The temperature dependence of C_{44} has a large difference between with and without magnetic field, as shown in Figure 3.9. The elastic constants could not satisfied the equation $(C_{11} + C_{12} + 2C_{44}) = 2C_{11} - (C_{11} - C_{12}) + 2C_{44}$. This anomaly could not be completely understood. In order to look more into this discrepancy, X-ray diffraction of the high temperature phase of $Ni_{0.49}Mn_{0.234}Ga_{0.276}$ was studied.

Austenitic Ni_2MnGa has a fcc $L2_1$ Heusler structure (space group Fm3m, No. 225). If the Mn and Ga sites are not distinguished, the structure can be viewed as being composed of eight CsCl-type units (a_{CsCl}=$a_{fcc}/2$), with Ni at the cube center and Mn and Ga at the corners. Three types of Bragg reflections exist: (1) the order-independent principal bcc reflections with $h + k + l = 4n$ (structure factor $F = 4\,(2b_{Ni} + b_{Mn} + b_{Ga}) \approx 9.66 \times 10^{-12} cm$); (2) reflections of type $h + k + l = 4n + 2$ ($F = 4\,(2b_{Ni} - b_{Mn} - b_{Ga}) \approx 6.82 \times 10^{-12} cm$) corresponding to a B2 (Cs-Cl type) structure; (3) the fcc superlattice reflections with h, k, l all odd ($F = 4\,(b_{Mn} - b_{Ga}) \approx -4.41 \times 10^{-12} cm$).

Figure 3.10 shows the 3D view of the temperature dependent X-ray diffraction spectrums and the temperature dependence of the elastic constant, C_{44}. The intensity of the Xray peaks decrease rapidly from 60°C to 80°C. The X-ray results indicate the transition at the temperature higher than the martensitic transformation. Nevertheless, the temperature dependence of the lattice parameter only shows the ordinary thermal expansion. The nature of the transition is not clear.

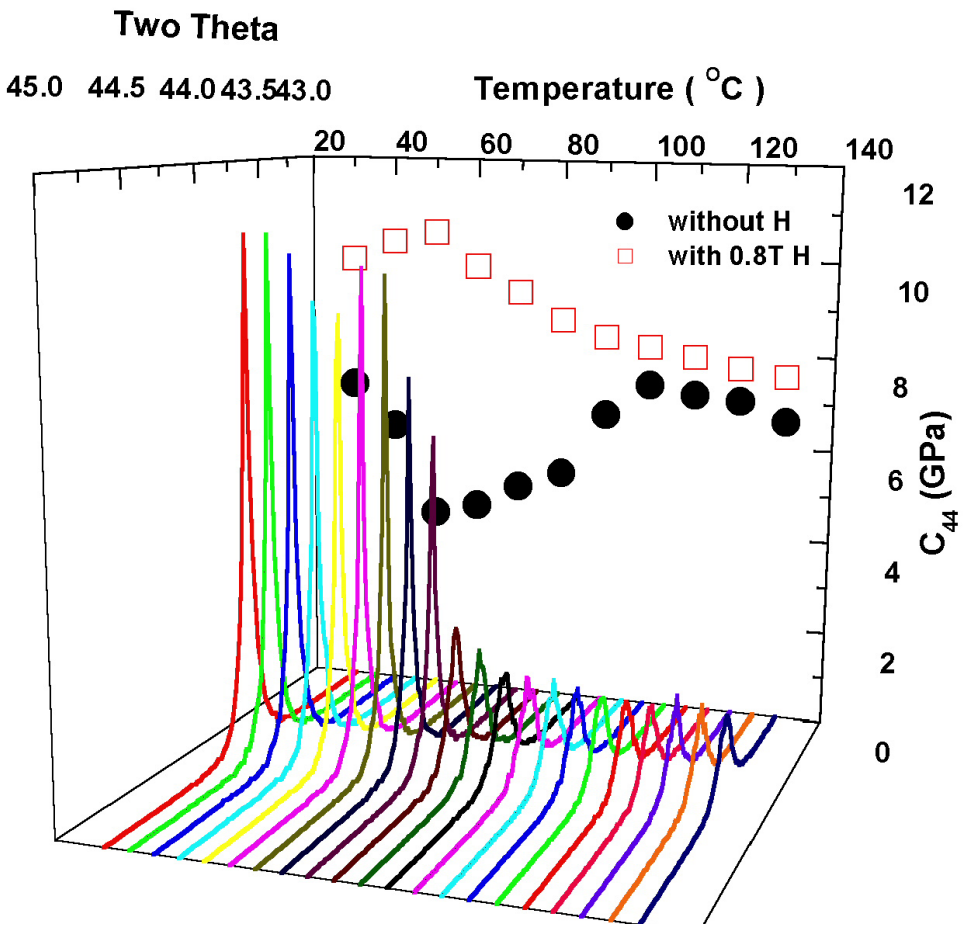

Figure 3.10: 3D view of the temperature dependent X-ray diffraction $< 220 >$ spectrum and the temperature dependence of the elastic constant, C_{44}.

This would be an interesting question for further study.

3.2.3 Discussion

The temperature dependence of the elastic constants of both of the samples clearly shows there is a transition before the martensitic phase transformation.

There is experimental evidence of a number of precursor phenomena when bcc solids approach a martensitic transformation.[31, 56, 5, 7] These precursors have been observed by many different experimental techniques such as x-ray, electron,

and neutron scattering and ultrasonic measurements among others[61, 55, 56]. In recent years much attention has been give to precursor effects where acoustic anomalies, phonon dispersion curves, and diffuse elastic scattering in the parent phase give an indication of the eventual martensitic structure.[69, 41] Some of these phenomena, such as the observation of an intermediate tweed structure [48, 50] are not common to all systems transforming martensitically but others, which are intimately related to the transformation mechanism, have been reported to occur in all materials investigated so far. This is the case of the anomalous dynamical response of the lattice to some specific displacements; all bcc austenitic materials exhibit a low TA_2, [110] propagation and $[1\bar{1}0]$ polarization, phonon branch which is accompanied by a low value of the elastic constant C', $(C_{11}\text{-}C_{12})/2$.[41] Both the elastic constant and the phonon branch soften on approaching the transition.

Heusler alloys undergo a martensitic transformation. Precursor phenomena have been recently reported for this alloys system. Inelastic neutron-scattering experiments have evidenced a well-defined dip in the TA_2 phonon branch close to q=0.33.[70, 68] The existence of these soft phonon modes gives rise to diffuse x-ray [18] and electron scattering [70] at temperatures above the martensitic transformation temperature, M_S. When the sample is cooled down, this dip becomes more pronounced, but the softening is always incomplete and below a given temperature still above M_S the frequency of the soft modes starts to increase again.[70] The prototype alloy system where similar softening effects have been observed is Ni-Al [49]; however, the amount of softening measured in Ni_2MnGa is larger and in Ni-Al there is not an increase of the frequency below a given temperature. Also, measurements by some of the present authors have shown that[33], at the temperature of phonon condensation the thermal expansion and elastic modulus versus

temperature curves exhibit a minimum, which is accompanied by an increase in the internal friction. Moreover a latent heat around 9 J/ mol was measured using a highly sensitive calorimeter.[46] All these experimental evidences suggest that the appearance of the mciro-modulated structure is a true phase transition.

The elastic properties in the vicinity of the premartensitic transformation were investigated by Trivisonno's group with ultrasonic study.[65] The temperature dependence around the transition temperature of the longitudinal, fast shear and slow shear are shown in Figure 3.11(a). The martensitic transformation temperature of this sample is around 260K. In all the modes, the velocity began to decrease with temperature in a dramatic way before the martensitic transformation. This behavior is more consistent with the results obtained in the electromagnetic generation (EMG) study by Vasil'ev et al.[63]. All the ultrasonic studies show that the velocity decreases dramatically as the intermediate phase transformation is approached. This decrease in the velocity for all three modes above the transformation temperature is clearly the signature of an incipient structural instability.

Ultrasonic attenuation measurements provide additional information about the transformation. Figure 3.11(b) also shows the temperature dependence of the attenuation for the longitudinal and shear modes. A large increase in the attenuation occurs along with a more rapid decrease in velocity as the intermediate transformation temperature, T_I, is approached. Ultrasonic attenuation and velocity measurements associated with the C' mode clearly are very sensitive probes of the structural instability, which is not surprising this mode is anomalously low. Premartensitic transformation effects in the slow shear velocity and attenuation are clearly observed 20K above the martensitic transformation.

It was shown that Ni-Mn-Ga alloys with specific compositions develop a mod-

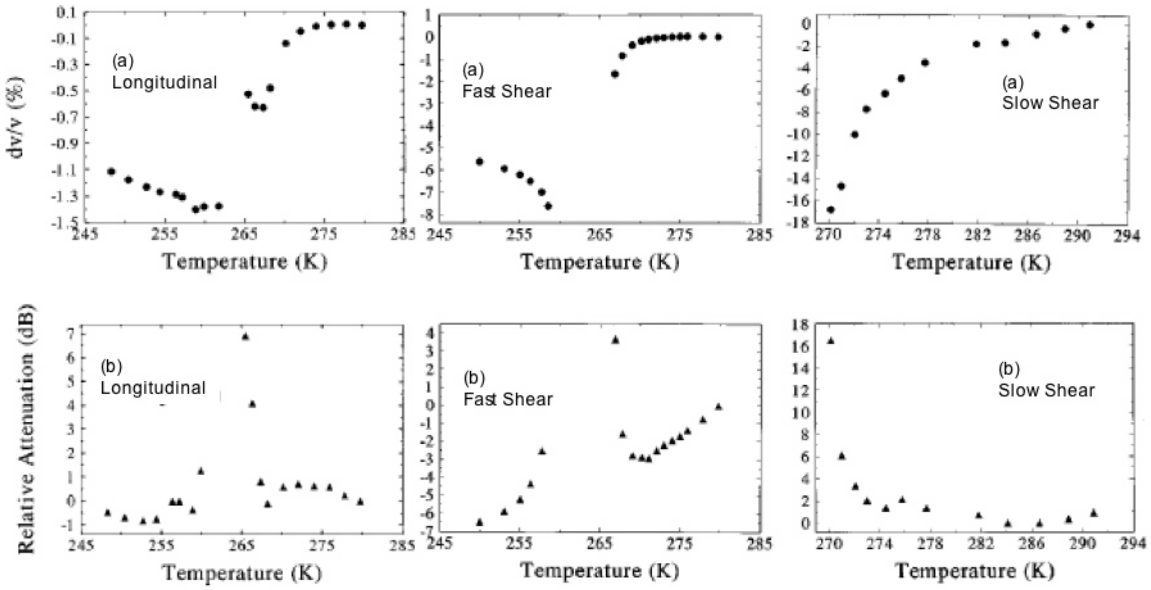

Figure 3.11: Temperature dependence of the relative velocity (a), V_L V_{44} and V', and the relative attenuation (b) associated with the elastic constant [65]

ulated structure [46, 43, 41, 20, 6, 7] at temperatures above the martensitic transition. This premartensitic transition is found to occur only for alloys with an electron to atom ration, e/a smaller than 7.60. Figure 3.12 presents the martensitic transformation, premartensitic transformation, and Curie temperature of Ni_2MnGa alloys vs. concentration of valence electrons (e/a). The crystal we studied, $Ni_{0.50}Mn_{0.284}Ga_{0.216}$, $Ni_{0.49}Mn_{0.234}Ga_{0.276}$ have e/a about 7.636 and 7.366, respectively. They are either near or below 7.60. We therefore did not anticipate finding a premartensitic transition in it. In addition to the temperature near M_S, anomalous behavior of elastic moduli is expected to occur near the Curie temperature, T_C. Both ultrasonic investigations and neutron scattering studies of polycrystalline Ni-Mn-Ga alloys[7] indicate that the slope of E(T), the Young's modulus as function of temperature, changes near the Curie point.

Our elastic constants study and said previous investigations clearly show that

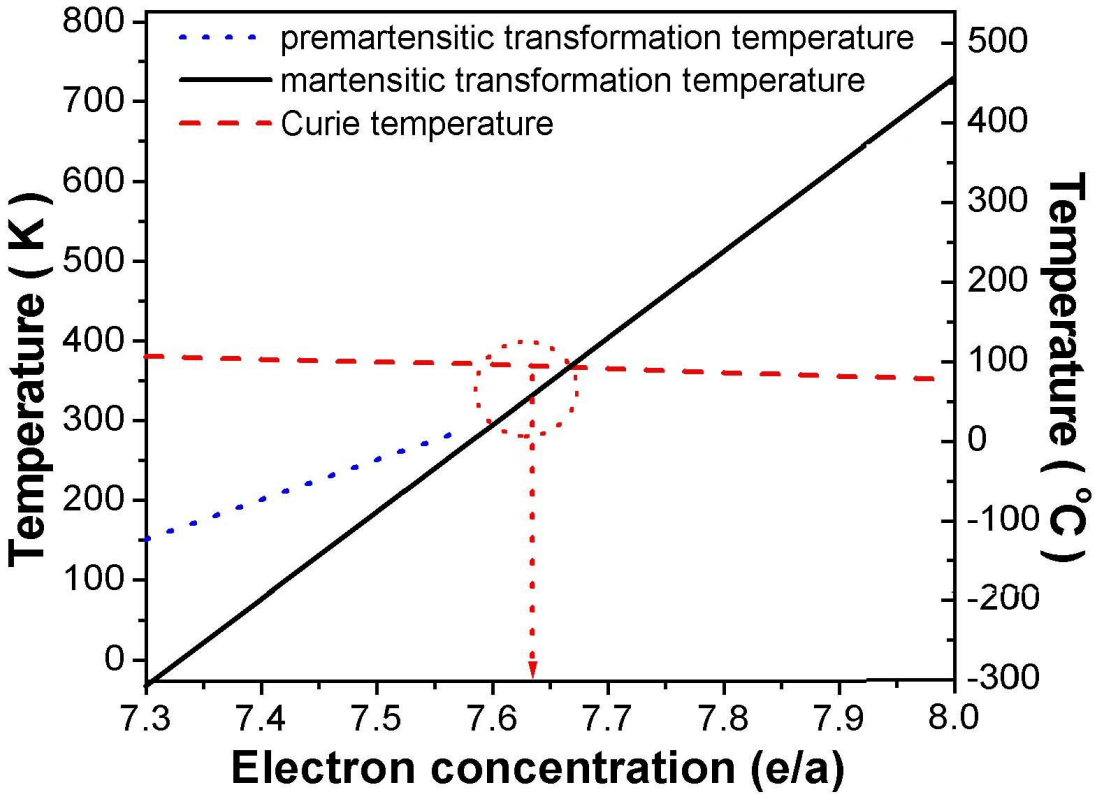

Figure 3.12: Schematic representation of the martensitic transformation, premartensitic transformation, and Curie temperature of Ni_2MnGa alloys vs. concentration of valence electrons (e/a). The crystals investigated have concentrations of e/a = 7.636 and 7.366, which are lower or slightly higher than 7.60. It therefore falls into an intermediate region, where the premartensitic transformation temperature has merged with the martensite, which is still lower than the Curie temperature.

in certain Ni_2MnGa alloys the martensitic transformation is preceded by a pre-martensitic transition. However the nature of this transition is not completely understood yet.

3.3 Elasticity of Ni_2MnGa Low Temperature Phase

3.3.1 Elastic Constants of $Ni_{0.50}Mn_{0.284}Ga_{0.216}$ in Low Temperature Phase

The temperature dependence of the elastic constants in $Ni_{0.50}Mn_{0.284}Ga_{0.216}$ martensitie were studied in the temperature range from 318K down to 200K. Measurements were conducted using the ultrasonic continuous wave method in a 0.8 T magnetic field.

In a previous section, we reported our elastic constants measurements in the austenite phase of $Ni_{0.50}Mn_{0.284}Ga_{0.216}$. The same cuboidal sample, 10mm long on each side, had been oriented so that four opposing faces have a $\langle 110 \rangle$ normal, whereas the other two faces have a $\langle 100 \rangle$ normal. The experimental method and setup were as the same in the high temperature phase study. All measurements were conducted in a magnetic field, $\hat{H}$ of 0.8T. The magnetic field was applied at 420K and remained on as the sample was cooled down to 190K. This was done in an attempt to create single variant conditions in the non-cubic phases[62]. In anticipation of the formation of two different orientations of a field-induced tetragonal crystal two field orientations were used, [100] and [001] as shown in Figure 2.3. According to the sample's orientation and the elastic wave propagation ($\hat{W}$) and polarization ($\hat{P}$) directions, there are five modes with $\hat{H}$ along [001] and six modes with $\hat{H}$ [100] available to measure[39]. For example, as shown in Table 2.2,

waves propagating in [110] with [1$\bar{1}$0] polarization directly determine C' with [001] $\hat{H}$ and C* with [100] $\hat{H}$. The latter is a combination of the usual tetragonal constants as shown in Table 2.2. For the purpose of checking the experimental data, we have eleven modes to measure six independent elastic constants; therefore the elastic constants were over determined. Moreover there are three different elastic wave mode to measure the same elastic constants, C_{44}, which was shaded in Figure 2.1. They gave the same result within 2%. These conditions allowed us to check for consistency in the determination of several of the constants.

The measurements described above, the elastic constants in tetragonal martensitic state, may be summarized as follows. Velocities of eleven elastic waves were measured and from them the six independent elastic constants of the tetragonal phase were determined consistently. Figure 3.13 shows the temperature dependence of six of the modes so determined in the temperature range below the 318K transition. C_{66} is very near C_{44} in that temperature range and C_{33} shows similar behavior to C_{11} as expected. All six elastic constants show the abrupt change around 220 K, clearly indicating that there is a transition from the tetragonal phase to another phase. It indicates a structural phase change from the tetragonal (5M) martensite to a second, probably tetragonal, phase (non-layered) at lower temperature. We have no direct evidence for the nature of the new phase. However from our data we can give some insight into what it might be. Moreover we made a Landau model to understand the anomalous behavior of the small elastic constants in the inte-rmartensitic transformation, which agrees the experimental data of the small elastic constants, C', reasonably well.

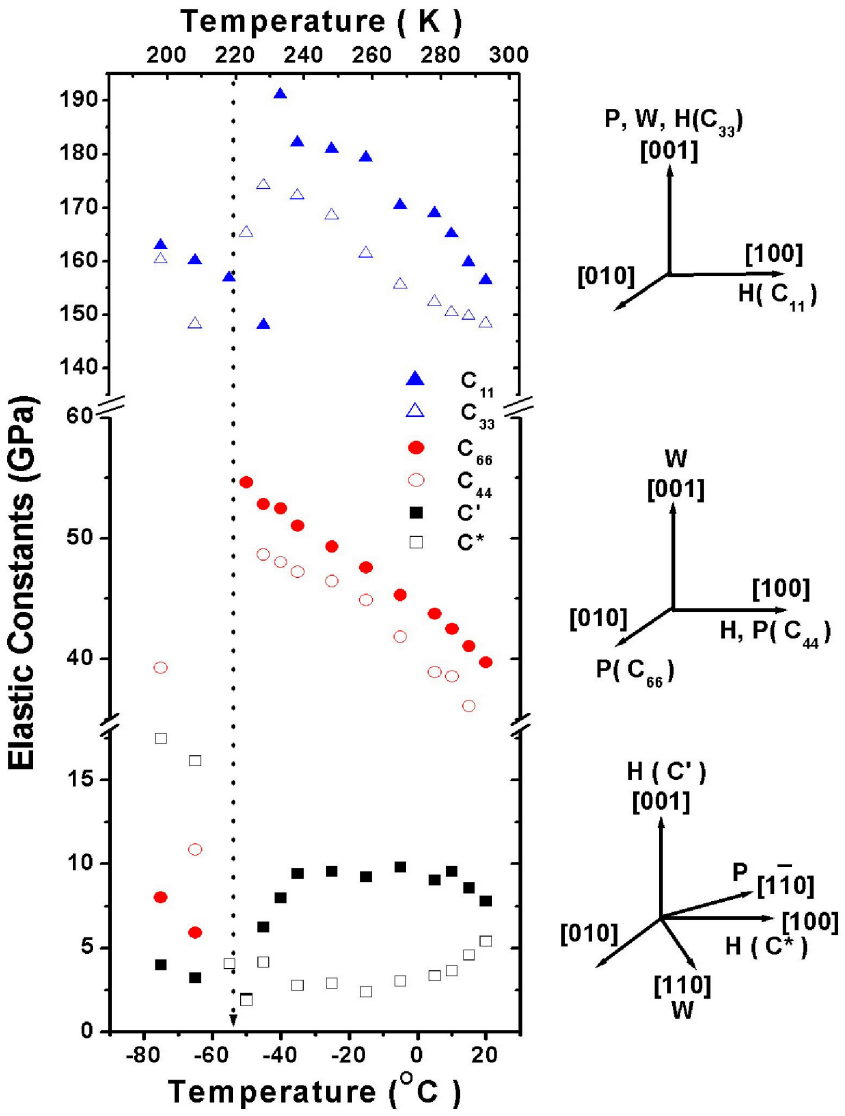

Figure 3.13: Temperature dependence of six elastic constants, C_{11}, C_{33}, C_{44}, C_{66}, C*and C' of $Ni_{0.50}Mn_{0.284}Ga_{0.216}$ below the first martensitic transformation temperature. The C* is defined in the Table 2.2. The data points below the inter-martensitic transformation only show the continuous change of the wave velocities. The elastic constants notation of the tetragonal, c/a<1 phase, is not suitable anymore. Since we propose the second martensite to be the tetragonal, c/a>1 phase, those data points merely show some combination of the true elastic constants. The propagation and polarization directions used to obtain the data are shown on the right. The field directions used to create the single-variant states are also shown.

3.3.2 Discussion

Figure 3.14 displays a temperature vs. valence electron concentration (e/a) phase diagram, which we developed on the basis of these results and those of earlier work[53, 54]. The most important part of this diagram is in the regime of e/a around 7.636, because it shows that the plausible low temperature phase at this e/a ratio is the tetragonal phase with c/a greater than 1, while c/a is known to be less than one in the first tetragonal phase. The elastic constants in the low temperature phase make this a reasonable picture. To do this we refer to Figure 3.15, where we show the two smallest elastic constants over the entire temperature range starting from 380K. In the cubic phase they are degenerate and equal to C', and below 318K they are split into two by the tetragonal distortion. The upper mode is the tetragonal C' mode, describing the stiffness of the tetragonal distortion in the xy plane. The lower, C*, is actually a combination of the five elastic constants. Physically it represents the stiffness for further tetragonal distortion in the xz or yz planes. As the 220 K transition is approached, C' again goes soft and becomes degenerate with C*. If only C' were getting soft in the tetragonal phase, one would expect the low temperature phase to be orthorhombic. However the fact that the C* is also very small, indicates a reentrant behavior, that is, a return to the cubic phase (c/a=1) and then further distortion to a c/a>1 phase at around 220K.

This section presents our study of the temperature dependence of the elastic constants of martensitic $Ni_{0.50}Mn_{0.284}Ga_{0.216}$ from 428K down to 200K. All the elastic constants have been measured as shown in Figure 3.13. Abrupt changes of all the elastic constants were found at around 220K. These changes indicate a structural phase change in the martensitic state. According to the previous investigations and the data of elastic constants, we found there is inter-martensitic

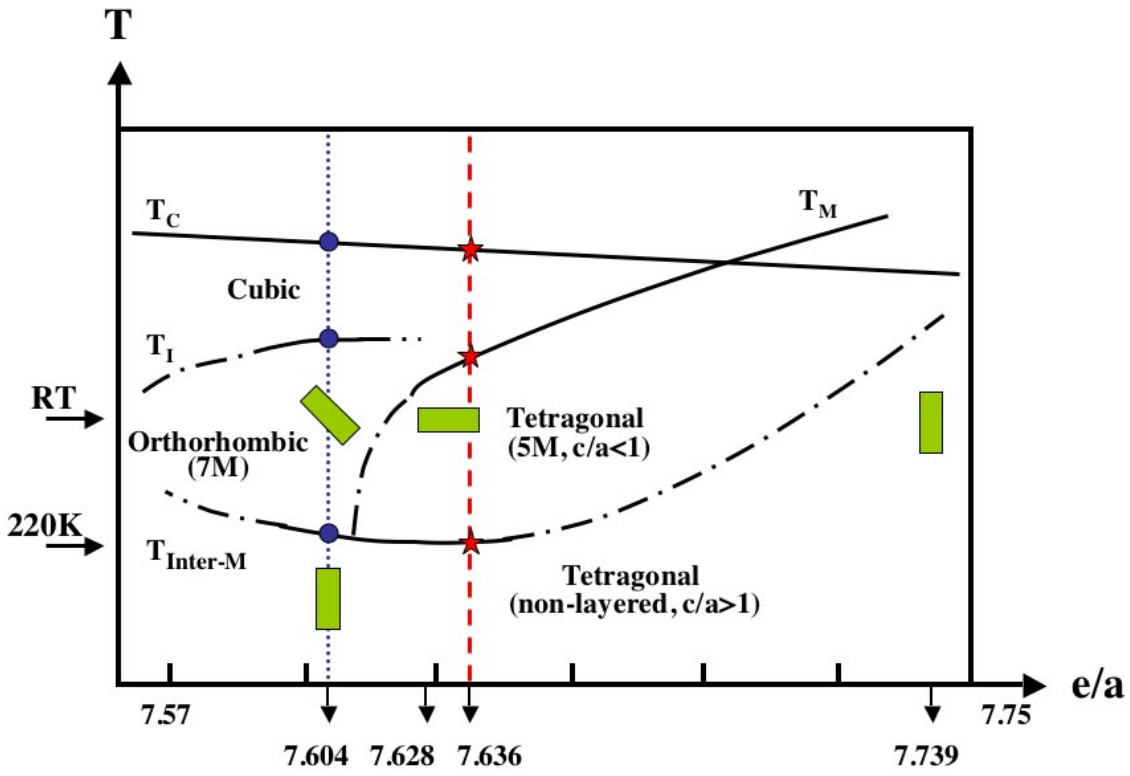

Figure 3.14: Schematic representation of structural and magnetic transformations in NiMnGa alloys vs. concentration of valence electrons (e/a). The different transformation temperatures, namely Curie temperature, Martensitic Transformation, Cubic to Orthorhombic transformation and inter-Martensitic transformation are depicted by T_C, T_M, T_I and TInter-M, respectively. The crystal investigated in this work has a concentration of e/a= 7.636, as marked. The diagram was assembled with the help of the results obtained on three other crystals of similar composition, whose e/a values are also marked. According to our elastic constant data, we found the inter-martensitic transformation at around 220K. The tetragonal non-layered phase has c/a>1. The dash-dot line was drawn so to allow the sample with e/a equal 7.74 to be in the non-layered tetragonal phase at room temperature consistent with earlier work

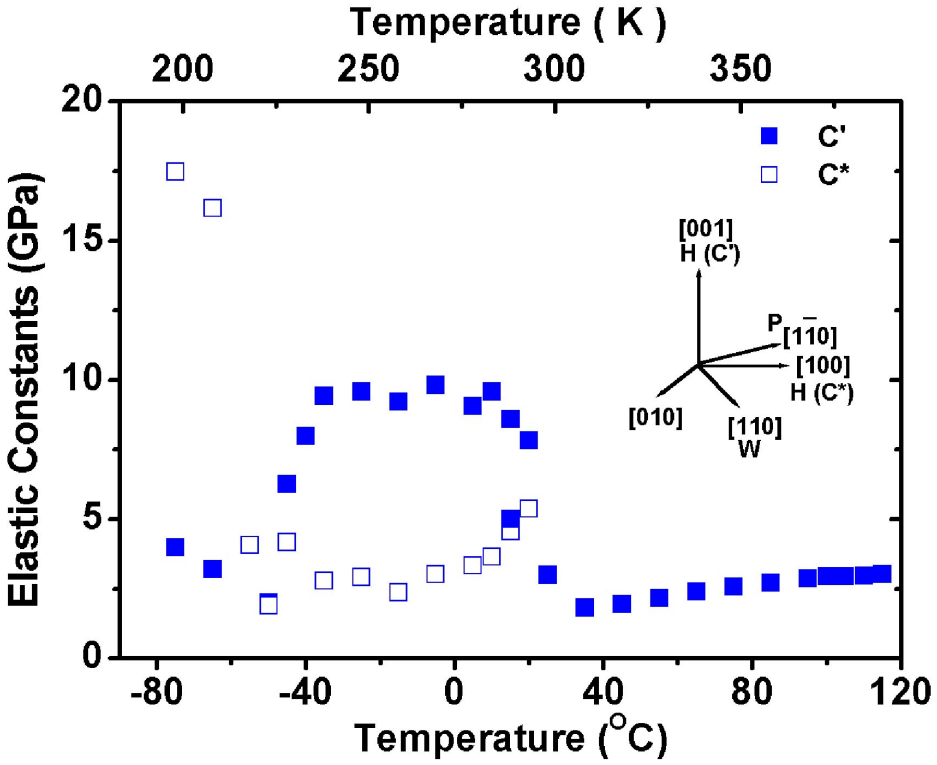

Figure 3.15: The elastic constants, C and C* are plotted vs. temperature from 380K (above the Curie point) to 200K. Measurements were taken with transverse waves along [110] with polarization [110]. C' was determined with magnetic field along [001] (solid square); and C* was determined with H parallel to [100] (open square). In the austenite, which is at the temperature higher than 318K, the two modes are degenerate. Notice how the C' mode drops rapidly below 233K, so that the two modes again degenerate at around 220K

transformation in NiMnGa alloys and developed a reasonable schematic phase diagram as shown in Figure 3.14. The degeneracy of C* and C' at around 220K, as depicted in Figure 3.15, indicates the possibility that the tetragonal (5M) martensite returns to the cubic-like phase and then further distorts to the tetragonal (non-layered) phase at lower temperature.

3.4 Model for the Elastic Behaviors Near Intermartensitic Transitions

The Heusler alloy Ni_2MnGa is a class of materials which undergoes martensitic transitions at temperatures which vary from 220K for stoichiometric samples to room temperature and above as the stoichiometry changes.[54] The alloys are ferromagnetic at room temperature; T_C is around 380K and varies only slightly as the composition changes.[61] Many of these alloys display a shape memory effect which can be activated by the application of a magnetic field. This property, called magnetic shape memory, has motivated a considerable amount of research into the physical properties of these materials. Much of this work has been centered on the cubic to tetragonal or orthorhombic transitions. Lately, however, there have been reports of intermartensitic transformations[54, 53]. Transitions between different martensitic states have been observed in $Ni_{50}Mn_{28.4}Ga_{21.6}$ using elastic constants measurements [16], and in $Ni_{48.8}Mn_{29.7}Ga_{21.5}$ using X-ray and DSC measurements [53]. The elastic constant measurements are particularly interesting.

Transitions between different martensitic states of $Ni_{50}Mn_{28.4}Ga_{21.6}$ have been observed using elastic constants measurements [16], and in $Ni_{48.8}Mn_{29.7}Ga_{21.5}$ using X-ray, DSC measurements [53]. The constant, C', which softened in the

austenitic phases, split into two at the M_S, 318K, temperature. One of the two new shear modules stiffens before softening again at the lower transformation M_{S2}, 220K. The other modulus was shown to remain very soft, around 5GPa, from M_S to M_{S2}. The standard Landau theory of structural transitions, where strain is the order parameter, assumes that the appropriate elastic modulus softens to zero as a function of temperature while the coefficients of the higher order terms in the expression of the free energy are independent of temperature. This model cannot describe the observed re-entrant behavior of C'. Here we assume that the coefficient of the third-order term also has significant temperature dependence. This assumption results in a C' vs. temperature in good agreement with observation. The temperature behavior of the other soft modulus, C*, is not as well described in this model. The model and possible modifications to it are discussed and compared to the elastic constant data.

The standard Landau theory of structural transitions, where strain is the order parameter, assumes that the appropriate elastic modulus softens to zero as a function of temperature while the coefficients of the higher order terms in the expression of the free energy are independent of temperature. Here, we assume that the third-order term also varies with temperature significantly. In terms of the strain order parameters the free energy function has the general form:

$$\Psi = \frac{1}{2}(C_{11}+2C_{12})\varepsilon_1^2+C'(\varepsilon_2^2+\varepsilon_3^2)+\frac{1}{4}C_{44}(\varepsilon_4^2+\varepsilon_5^2+\varepsilon_6^2)+\frac{1}{3}b\varepsilon_3(\varepsilon_3^2-3\varepsilon_2^2)+\frac{1}{4}d(\varepsilon_2^2+\varepsilon_3^2)^2 \tag{3.2}$$

$$\textit{where} \qquad \varepsilon_1 = (\varepsilon_{xx}+\varepsilon_{yy}+\varepsilon_{zz})/\sqrt{3}, \qquad \varepsilon_2 = (\varepsilon_{xx}-\varepsilon_{yy})/\sqrt{2}$$

$$\varepsilon_3 = (2\varepsilon_{zz}-\varepsilon_{yy}-\varepsilon_{xx}), \qquad \varepsilon_4 = \varepsilon_{xy}, \varepsilon_5 = \varepsilon_{yz}, \varepsilon_6 = \varepsilon_{zx}$$

$$C' = (C_{11}-C_{12})/2, \qquad b = (C_{111}-C_{112}+C_{123})/6\sqrt{6}$$

$$d = (C_{1111}+C_{1112}-3C_{1122}-8C_{1123})/48.$$

C' is taken to depend linearly on temperature, as usual. However, we will also take b to be temperature dependent in what follows. For the purpose of this study the significant terms of the free energy in Equation (3.2) are:

$$\Psi = C'(\varepsilon_2^2 + \varepsilon_3^2) + \frac{1}{3}b\varepsilon_3(\varepsilon_3^2 - 3\varepsilon_2^2) + \frac{1}{4}d(\varepsilon_2^2 + \varepsilon_3^2)^2 \tag{3.3}$$

The first and third terms of the Equation (3.2) were ignored, because $C_{11}+ 2C_{12}$ and C_{44} are much bigger than C' in either phases, austenite or martensite.

It is convenient to introduce polar coordinates for ε_2 and ε_3. Take $\varepsilon_2 = \rho sin\theta, \varepsilon_3 = \rho cos\theta$. $(cos3\theta = cos^3\theta - 3sin^2\theta cos\theta)$, $\rho > 0$. If b$\neq$0, the low energy tetragonal states are those that minimize $b\rho^3 cos3\theta$. For $b < 0$, the choice of $\theta = 0, \frac{2\pi}{3}\frac{4\pi}{3}, ...$ gives the lowest free energy. When $\rho \neq 0$, this corresponds to a tetragonal state with $c/a < 1$. For $b > 0$, another set, $\theta = \frac{\pi}{3}\pi, \frac{5\pi}{3}, ...$, would result in the lowest free energy and correspond to $c/a > 1$. The possible states are schematically shown in Figure 3.16 and Figure 3.17. Either sign of b gives the same result for the effective modulus in the martensite.

For b$<$ 0, we focus on the $\theta = 0$ solution. Then the Equation (3.3) simplifies as:

$$\Psi(\rho) - \Psi_0 = C'\rho^2 - \frac{1}{3}b\rho^3 + \frac{1}{4}d\rho^4 \tag{3.4}$$

We take d$>$0 and rescale Ψ by dividing it by d, therefore $b \Rightarrow \frac{b}{d}$, $C' \Rightarrow \frac{C'}{d}$. Further minimization with respect to ρ gives the stable solutions:

$$\begin{cases} \rho_0 = 0 & cubic\ phase,\ C' > \frac{1}{9}b^2 \\ \rho_+ = \frac{b}{2c} + \sqrt{\left(\frac{b}{2c}\right)^2 - 2C'} & tetragonal\ phase,\ C' < \frac{1}{9}b^2 \end{cases} \tag{3.5}$$

There is a first order transition, ρ_0 to ρ_+ at the $C'_{boundary}$. The elastic constant, C', at the cubic to tetragonal transition boundary was calculated as:

$$C'_{boundary} = \frac{1}{9}b^2 \tag{3.6}$$

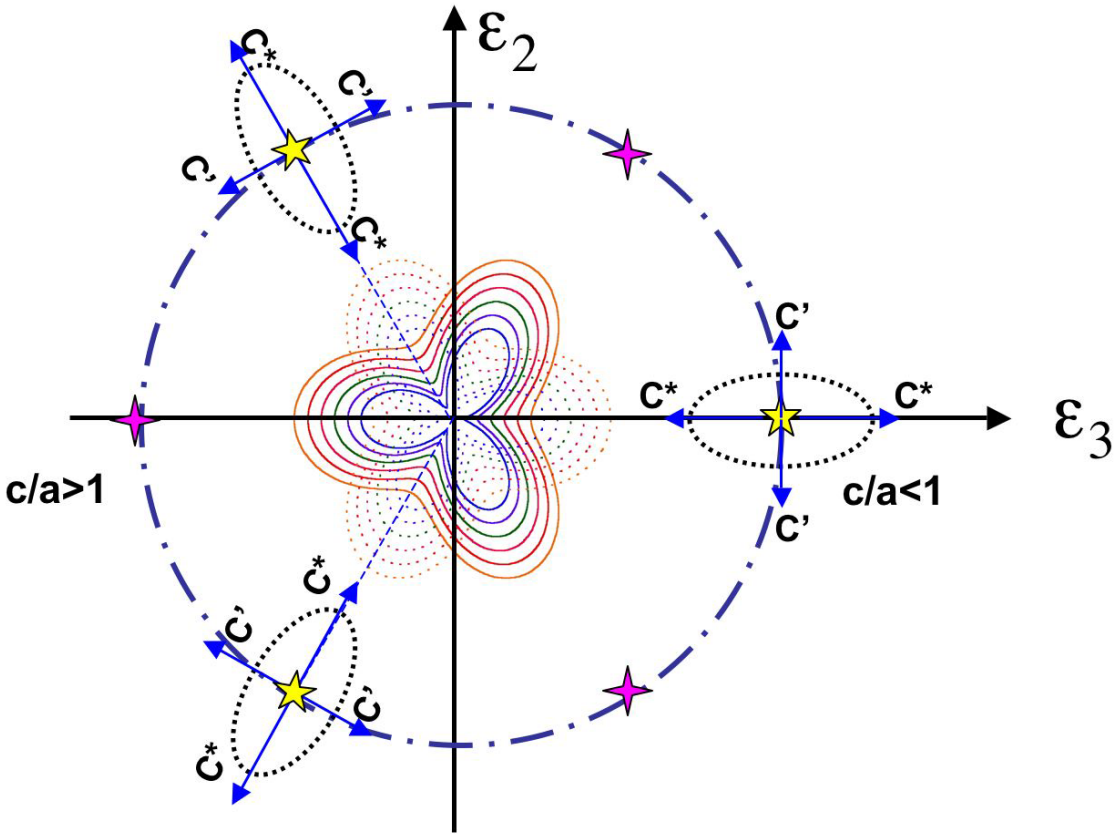

Figure 3.16: A Strain-space map showing the possible phase equilibrium and distortions from one of them. The radius of the dotted circle is the value of ρ, the C' and C* are the moduli corresponding to orthorhombic and tetragonal distortions, respectively. θ is the angle between the structure's position and ε_3 axis. If θ equals zero, C' and C* correspond to the deformation along ε_2 and ε_3, respectively. The center shows the free energy contour with respect to different sign of b.

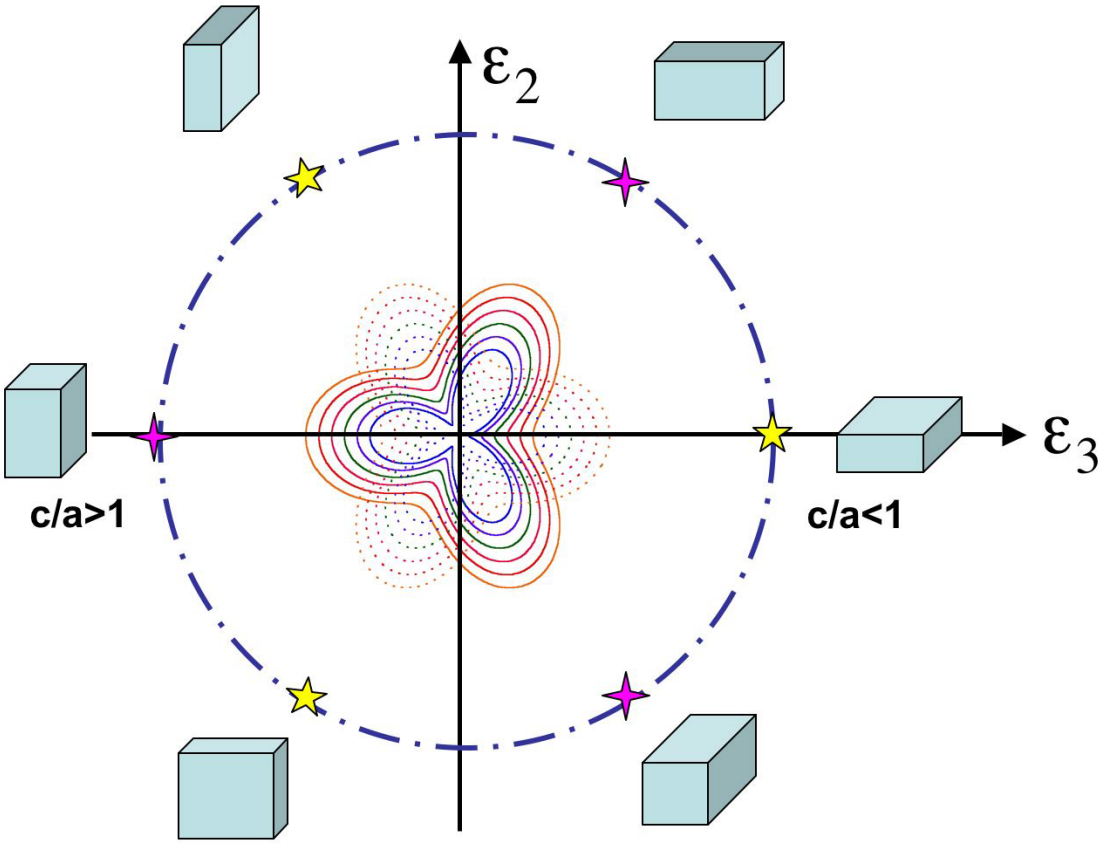

Figure 3.17: Shows at different sets of θ value, there are different types of tetragonal with respect to the c/a ratio.

Therefore the tetragonal state has the same energy as the cubic phase at $C' = \frac{b^2}{9}$, where $\rho_+ = \frac{b}{2} + \sqrt{(\frac{b}{2})^2 - 2C'} = \frac{2}{3}b$.

For $b > 0$, the energy favorable angle is: $\theta = \frac{\pi}{3}, \pi, \frac{5\pi}{3}, ...$ The equivalent result for $b < 0$ is:

$$\begin{cases} \rho_0 = 0 & \textit{cubic phase, } C' > \frac{1}{9}b^2 \\ \rho_+ = \frac{b}{2c} + \sqrt{\left(\frac{b}{2c}\right)^2 - 2C'} & \textit{tetragonal phase, } C' < \frac{1}{9}b^2 \end{cases} \tag{3.7}$$

To find expressions for the two lowest moduli in the tetragonal phase, we expand the free energy around $\rho = \rho_+,\ \theta = 0$, to second order in ε_2 and ε_3 and obtain the energy formula:

$$\Psi = \Psi(\rho_+) + \frac{1}{2}C'_{tet}(\varepsilon_2 - 0)^2 + \frac{1}{2}C^*(\varepsilon_3 - \rho_+)^2 \tag{3.8}$$

Substitute $\varepsilon_3 = \rho_+ + \delta\varepsilon_3$ into Equation (3.3):

$$\begin{aligned} \Psi &= C'\left(\varepsilon_2^2 + (\rho_+ + \delta\varepsilon_3)^2\right) \\ &\quad -\frac{1}{3}b\left(\rho_+ + \delta\varepsilon_3\right)\left((\rho_+ + \delta\varepsilon_3)^2 - 3\varepsilon_2^2\right) + \frac{1}{4}d\left(\varepsilon_2^2 + (\rho_+ + \delta\varepsilon_3)^2\right)^2 \end{aligned} \tag{3.9}$$

Assuming $\frac{\partial\Psi}{\partial\varepsilon_3} = 0$ and neglecting the terms higher than the 3th order. Equation (3.9) is simplified to

$$\Psi - \Psi_0 = C'\varepsilon_2^2 + b\rho_+\varepsilon_2^2 + \frac{1}{2}c\rho_+^2\varepsilon_2^2 + C'\left(\delta\varepsilon_3\right)^2 - b\rho_+\left(\delta\varepsilon_3\right)^2 + \frac{3}{2}d\rho_+^2\left(\delta\varepsilon_3\right)^2 \tag{3.10}$$

The two shear elastic constants are then found to be:

$$(C')_{Tet} = \frac{3b}{2}\left(\frac{b}{2} + \sqrt{\left(\frac{b}{2}\right)^2 - 2C'}\right) \tag{3.11}$$

$$C^* = -2C' + \frac{b}{2}\left(\frac{b}{2} + \sqrt{\left(\frac{b}{2}\right)^2 - 2C'}\right) \tag{3.12}$$

From our previous discussion that C' at cubic-tetragonal boundary is equal to $\frac{b^2}{9}$. Therefore the C' in tetragonal around the cubic to tetragonal transition boundary is:

$$(C')_{Tet} = \frac{3b}{2}\left(\frac{b}{2} + \sqrt{\left(\frac{b}{2}\right)^2 - 2C'}\right) = b^2 \tag{3.13}$$

C* is the elastic constant for $\delta\varepsilon_3$. Therefore at cubic phase C*=C'$_{cub}$, which equals $\frac{b^2}{9}$ at the cubic-tetragonal boundary approached from the cubic side. The value of C* at the boundary from the tetragonal side could be calculated as:

$$(C^*)_{Tet} = -2C' + \frac{b}{2}\left(\frac{b}{2} + \sqrt{\left(\frac{b}{2}\right)^2 - 2C'}\right) = \frac{1}{9}b^2 \tag{3.14}$$

Therefore the elastic constant, C', has a nine times jump at the cubic-tetragonal boundary. This phenomenon was clearly experimentally proved in Figure 3.18. The calculation also shown that the C' and C* are degenerate at the boundary as shown experimentally.

This model also yields a C'$_{tet}$ vs. temperature dependence that is in good agreement with observations. The theory was compared to the experimental data by choosing suitable coefficients $b = b_0\frac{T-225}{225}$ and $C' = C'_0\frac{T-300}{300}$,where b_0 was chosen to set the overall scale to coincide with the data and C'$_0$ was chosen to fit C' in the austenitic phase. The choices will not affect the shape of the curve. The experimental results and the model results of C' are depicted in Figure 3.18. In the first tetragonal phase, C' rises with decreasing temperature, reaches a maximum, then decreases to zero at the second transition. Moreover C'$_{tet}$ increases by a factor of nine at the first martensitic transformation, which agrees with the experimental result very well. The temperature behavior of the other soft modulus, C*, is not as well described in this model. It remains positive. We have studied the effects of an applied magnetic field on both moduli, showing that C' is not altered, while

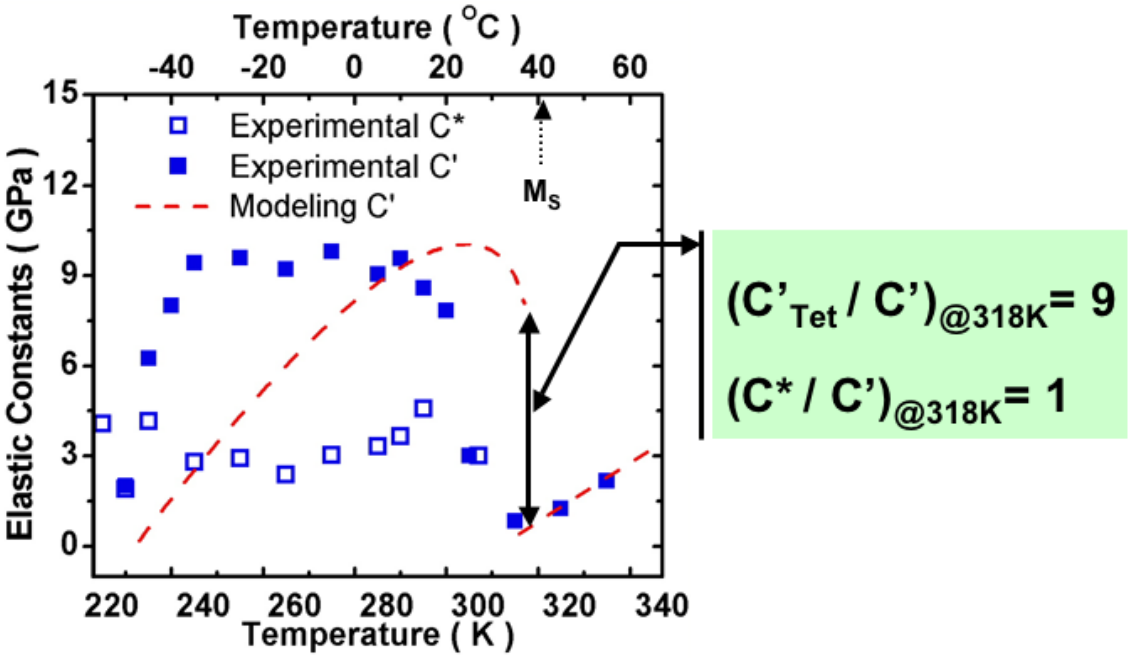

Figure 3.18: This graph shows that the result of the model fit the experimental data reasonably well. The elastic constant C has a nine times jump at the cubic-tetragonal boundary, which was experimentally proved. The calculation also shows that the C and C* degenerate at the boundary, which also was observed in the experiments. Result of modeling reproduces the major aspects of the temperature dependence of the shear elastic constant C.

C* is softened by its presence, due to magneto elastic coupling. In the followed section, the possible modifications to it will be discussed to find the modified term of C*, which make the model fit the experiment data better.

According to the discussion above, the temperature dependence of effect modulus, C*, in the model with only considered the elastic energy was not fitted with the experimental data well. Therefore in order to correct the calculation of C*, we took into account of the magnetic field effect. The free energy of the system with considering the magnetic field effects could be expressed as following:

$$\Psi(\delta\varepsilon) = \Psi(\rho) + \frac{1}{2}\Psi_{\parallel}"(\delta\varepsilon)^2 + \frac{1}{2}\Psi_{\perp}"\phi^2 + \Psi_{me} + \frac{1}{2}\chi^{-1}(\delta M_z)^2 \tag{3.15}$$

$$\begin{aligned} where\ \ \Psi_{me} &= -BM_3(\rho+\delta\varepsilon)\left(1-\tfrac{\phi^2}{2}\right) = -2BNM_s\delta M_z(\rho+\delta\varepsilon) \\ M_z = M_s - \delta M_z,\ \ M_3 &= N\left(M_z^2 - M_x^2 - M_y^2\right),\ \ M_z^2 = M_s^2 - 2M_s\delta M_z \\ \varepsilon_3 = \rho + \delta\varepsilon,\ \ &\Phi = 0 + \phi,\ \ cos\phi = 1 - \frac{\phi^2}{2} \end{aligned} \tag{3.16}$$

Substitute Equation (3.16) into Equation (3.15) with adding a stress, σ, for the strain, ε, yields free energy $\Psi = \Psi(\delta\varepsilon) - \Psi(\rho)$ as following:

$$\Psi = \frac{1}{2}\Psi_{\parallel}"(\delta\varepsilon)^2 + \frac{1}{2}\chi^{-1}(\delta M_z)^2 - 2BNM_s\delta M_z\delta\varepsilon - \sigma \bullet \delta\varepsilon \tag{3.17}$$

$$\begin{cases} \dfrac{\partial\Psi}{\partial(\delta M_z)} = \chi^{-1}(\delta M_z) - 2BNM_s\delta\varepsilon = 0 \quad (a) \\ \dfrac{\partial\Psi}{\partial(\delta\varepsilon)} = \Psi_{\parallel}"\delta\varepsilon - 2BNM_s\delta M_z - \sigma = 0 \quad (b) \end{cases} \tag{3.18}$$

From the Equation (3.18) (a) the δM_z could be obtained as the following expression:

$$\delta M_z = \frac{2BNM_s\delta\varepsilon}{\chi^{-1}} \tag{3.19}$$

Substituting Equation (3.19) into Equation (3.18) (b) yields the expression for $\delta\varepsilon$ as:

$$\Psi_{\parallel}"\delta\varepsilon - \frac{4B^2N^2M_s^2 \bullet \delta\varepsilon}{\chi^{-1}} - \sigma = 0 \Rightarrow \delta\varepsilon = \frac{\sigma}{\Psi_{\parallel}" - \dfrac{4(BNM_s)^2}{\chi^{-1}}} \tag{3.20}$$

Since the elastic constant, C*, is the stiffness according to the deformation $\delta\varepsilon$. Therefore the C^* with magnetic field effect could be represented as:

$$C^* = \Psi_{\parallel}\text{"} - \frac{4B^2N^2M_s^2}{\chi^{-1}} = -2C' + \frac{b}{2}\left[\frac{b}{2} + \sqrt{\left(\frac{b}{2}\right)^2 - 2C'}\right] - \frac{4B^2N^2M_s^2}{\chi^{-1}} \quad (3.21)$$

The calculation above results in the corrected effective elastic constant, C*, with a correction term, $\frac{4B^2N^2M_s^2}{\chi^{-1}}$. This term decreases the calculated C* in the model, so that the theoretic prediction agrees more closely with the experimental results.

3.5 Conclusion

In this chapter, the elasticity of ferromagnetic shape memory alloys, Ni_2MnGa, was studied in the austenitic and martensitic phases. Elasticity was investigated by the ultrasonic continuous wave method. According to the temperature dependence of elastic constants in Ni_2MnGa, the martensitic transformation, intermartensitic transition and premartensitic transitions were observed. A Landau model was designed to understand the reentry phenomenon of the small elastic constants at the intermartensitic transition. The model agrees our experimental results reasonably well.

Chapter 4

Elasticity of Fe_3Pd

In this chapter, the results of the magnetic field and temperature dependence of elastic constant in Fe_3Pd were studied. A magnetic field induced transformation was found by the study of the magnetic field dependence of elastic constants. It is possible that this phenomenon relates to the magnetic filed induced reversible actuation [36]. A premartensitic transformation was investigated by the temperature dependence of the elastic constants.

4.1 Sample Information

In this section the ferromagnetic shape memory alloy, Fe_3Pd was grown Bridgman method by Dr. Cui [12]. Both x-ray analysis and DSC measurements show that the FCC-FCT transformation is a weak first order thermoelastic transition. The average lattice parameters are a=3.822 Å and c=3.6298 Å for the FCT martensite, and a_0=3.7557 Å for the cubic austenite. The latent heat is 10.79±11 J/cm^3. The Curie temperature is 300°C. The saturation magnetization is m_s=1217 emu/cm^3 for the martensite and m_s=1081 emu/cm^3 for the austenite in Fe_3Pd alloy; the easy

axis of the austenitic Fe_3Pd is [111], where in martensitic Fe_3Pd [001] evidently is the hard axis and [100] and [010] are equally to be the easy axis, which is inverse with Ni_2MnGa. The magnetic anisotropy is -4.8×10^3 erg/cm^3 for the austenite at 60°C, and it is 3.46×10^5 erg/cm^3 for the martensite at -20°C. [12] The maximum ferromagnetic strain in this material is about 0.9%. The blocking stress is about -4 MPa. Furthermore, stress has large effect on the phase transformation temperature, for the compressive stress, it is 0.7°C/MPa. [12] The phase transformation temperature can also be changed by applying a magnetic field during cooling or heating. The cuboidal sample with 10mm on each side had been oriented so that six opposing faces have a ⟨100⟩ normal. In order to measure all the elastic constants with different wave modes, two corners, as shown in Figure 4.1 by dot line, of the sample were cut to obtain two ⟨110⟩ normal faces. The sample's orientation is shown in Figure 4.1.

4.2 Results and Discussion

All the elastic constants of the Fe_3Pd were measured by the ultrasonic continuous wave technique. The detail of this method and all the elastic wave modes were discussed in Charpter 2.

In order to study the temperature and magnetic field dependence of elastic constants, two types of measurements were designed for the study of the elasticity in Fe_3Pd. First is to measure the elastic constants by a various temperature range from room temperature to 80°C. The other type of measurement is at 70°C with applying magnetic field from 0 to 10000 Oe.

First, the temperature dependence of the elastic constants was studied. Figure 4.2 shows the resonance frequencies of longitudinal wave along $< 100 >$, which

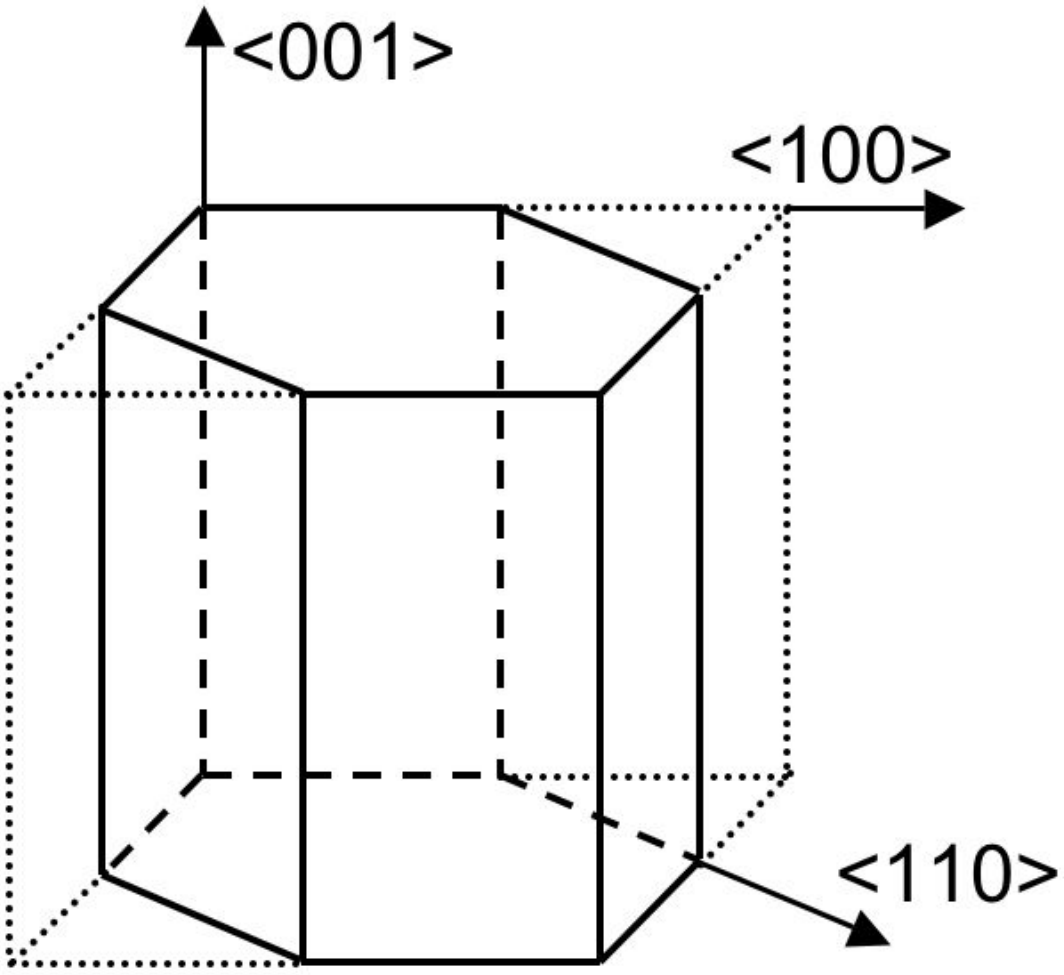

Figure 4.1: Sample orientation of $FePd_{30\pm0.5at\%}$

yields C_{11}. The peaks shows significant difference around 45°C. The results of C_{11}, converting from these spectrums, were depicted in Figure 4.3.

The temperature dependence of C', which is conducted by the shear wave with $[1\bar{1}0]$ polarization and [110] propagation direction was also studied. Figure 4.4 shows the spectrums with different temperatures. The peaks lost the periodic resonance frequencies around 45°C. And the spectrums shows the tendency to getting clearer with increasing temperature higher than 70°C. Even the peaks were hard to derive the elastic constant, C', it clearly shows a transition around 45°C, which is consistent with the result of the temperature dependence of C_{11}.

The temperature dependence of C_{11} and C' clearly shows a transformation around 45°C. The elastic constants results indicate probably a premartensitic transformation prior to the martensitic transformation.

The magnetic field dependence of the elastic constants was also studied. All the elastic constants were measured in 70°C, which is surely in the austenitic state, with applying magnetic field from 0 to 1T. All the elastic constants showed a magnetic field induced transformation. This transition might be the magnetic field induced reverse transition as the previous discussion. Moreover, the result shows reverse hysteresis of the C_{11}.

Figure 4.5 listed the spectrums of [001] longitudinal wave at 70°C with applying different magnetic field. The data was converted into elastic constant, C_{11}, which was depicted in Figure 4.6.

The magnetic field dependence of the shear wave with $[1\bar{1}0]$ polarization and [110] propagation direction was also depicted in Figure 4.4, which shows the spectrums with different magnetic field. It also shows that the peaks of the resonance frequencies were hard to analyze when the field is larger than 0.25T. Even it is

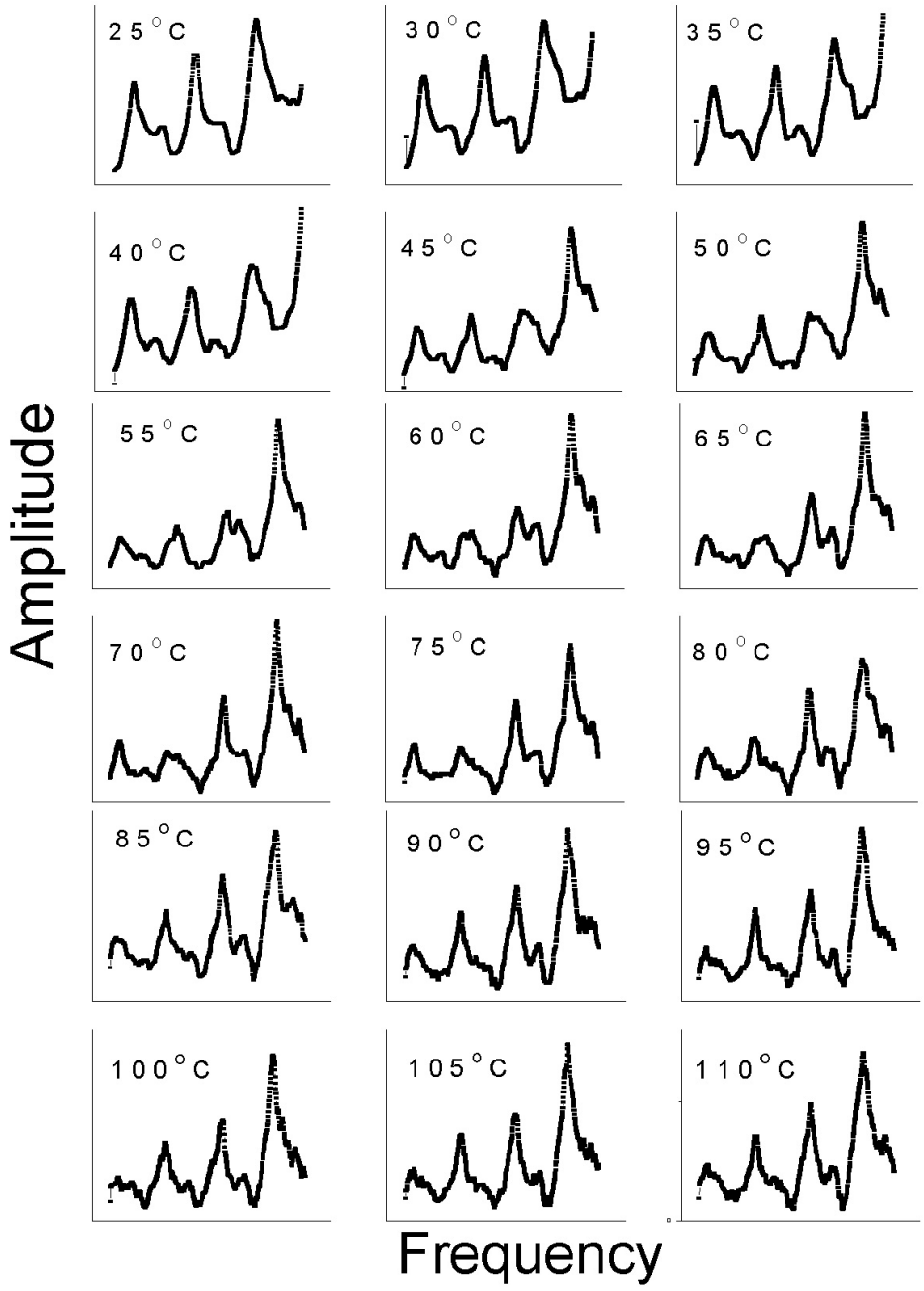

Figure 4.2: The wave spectrum of longitudinal elastic wave along [001] crystalline direction, which is for conducting the elastic constant, C_{11}, in ferromagnetic shape memory alloy, Fe_3Pd. The spectrums show significant changes around 45°C

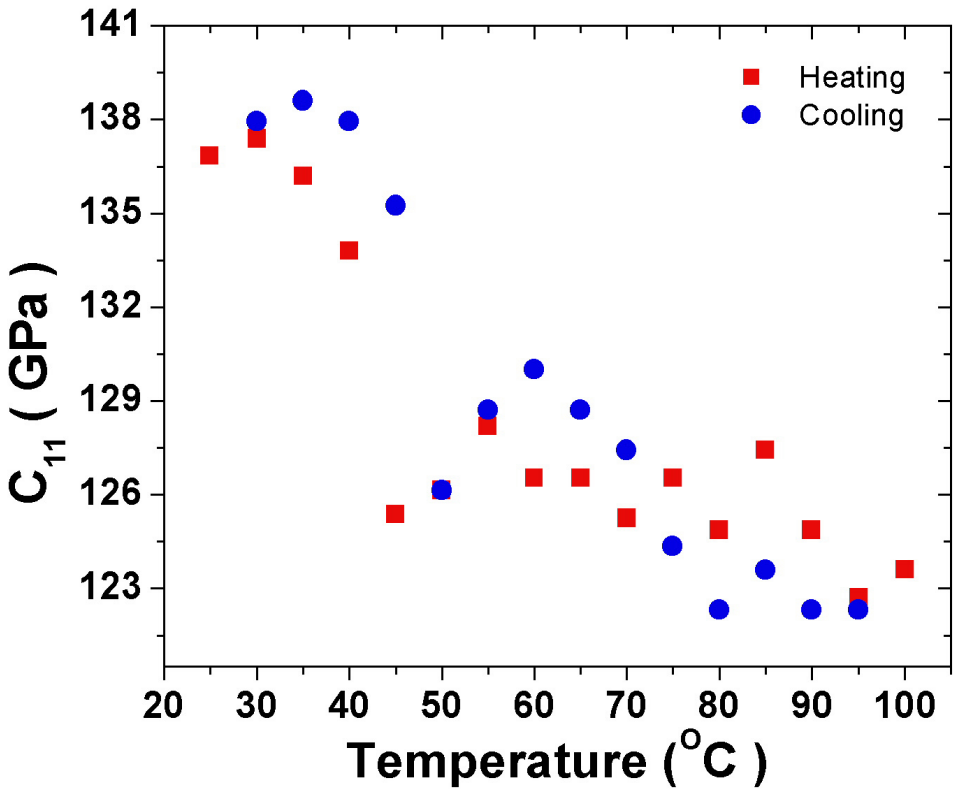

Figure 4.3: Magnetic field dependence of Elastic constant, C_{11}, in ferromagnetic shape memory alloy, Fe_3Pd.

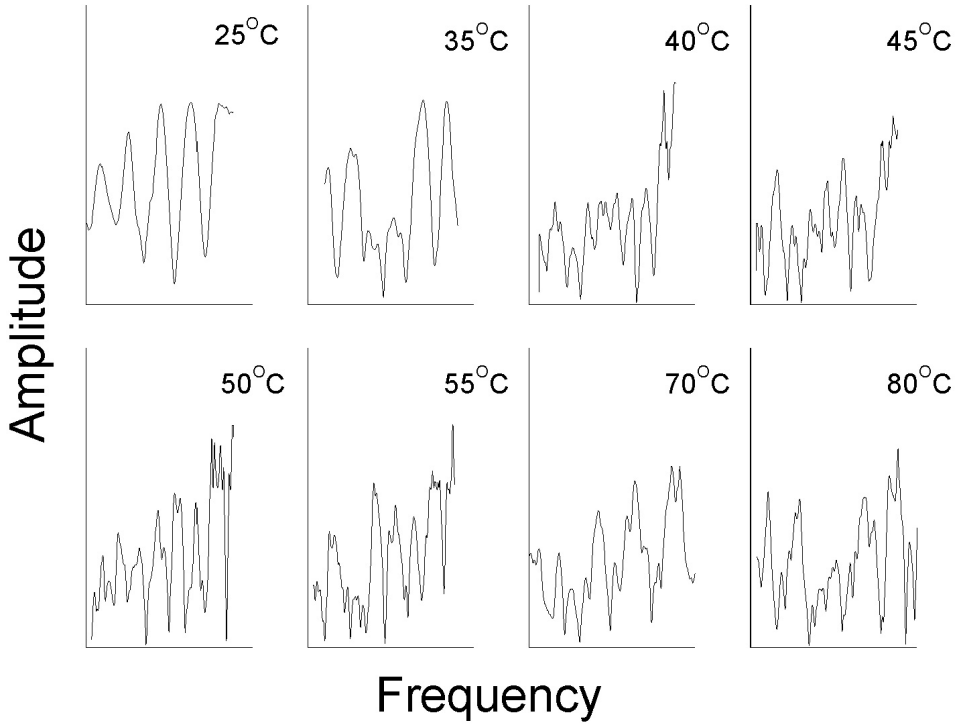

Figure 4.4: The wave spectrum of the temperature dependence of the shear elastic wave with polarization direction along $[1\bar{1}0]$ and propagation direction along [110], which is for conducting the elastic constant, C', in ferromagnetic shape memory alloy, Fe_3Pd. The spectrums show significant changes around 45°C

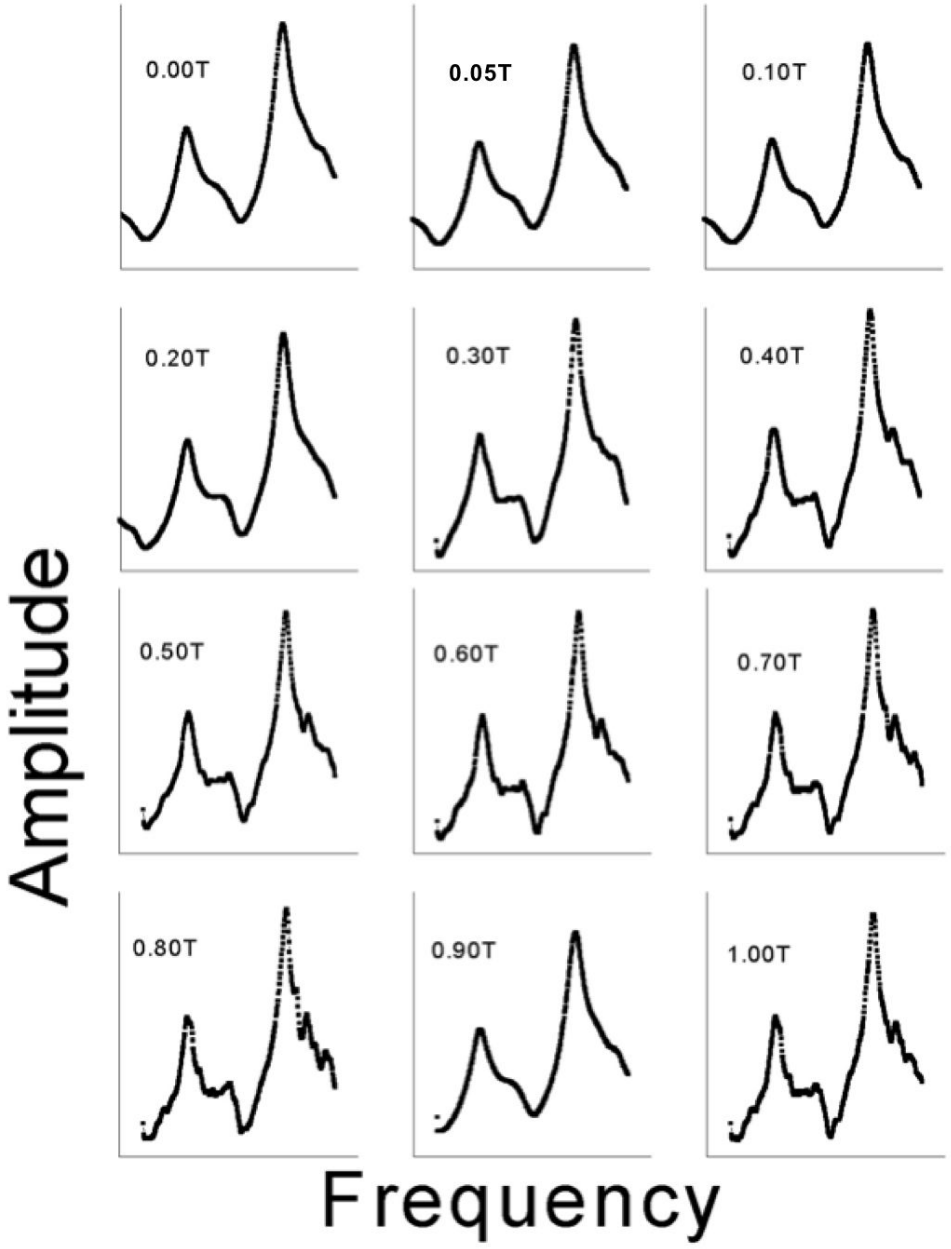

Figure 4.5: The wave spectrums of longitudinal elastic wave along [001], which is for conducting the elastic constant, C_{11} at 70°C with various magnetic field from 0 to 1T. The spectrums show significant changes around 0.25T

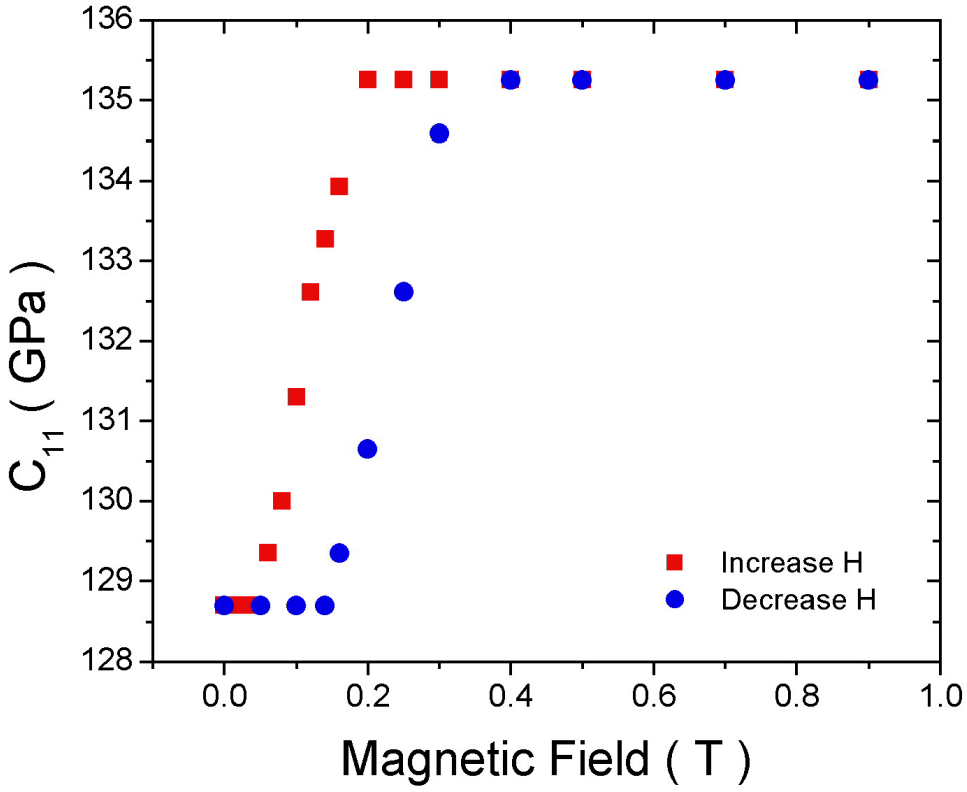

Figure 4.6: Magnetic field dependence of elastic constant, C_{11}, in ferromagnetic shape memory alloy, Fe_3Pd.

hard to directly show the magnetic field dependence of C', the spectrum indicate a magnetic field induced transition around 0.25T and it indicate the tendency of the change of C'. Another proof to confirm this field induced transition is the magnetic field dependence of shear wave propagating along [001] with [110] polarization direction, which correspond to the elastic constant, C_{44}. The spectrums were listed in Figure 4.8. The result is consistent with the magnetic field dependence of C_{11} and C', which indicates the magnetic field inducing transition.

The results of the magnetic field dependence of the elastic constants clearly show there is a transition with an external field around 0.25 T.

4.3 Conclusion

This section studied the elasticity of ferromagnetic shape memory alloy, Fe_3Pd. All the elastic constants in its austenitic state were measured by the ultrasonic continuous wave method with external temperature and magnetic field. The magnetic field and temperature effects of the elastic constants were investigated and discussed. The temperature dependence of the elastic constants shows a probably premartensitic transformation around 50°C. And the magnetic field inducing a transformation was observed in the elastic constants results.

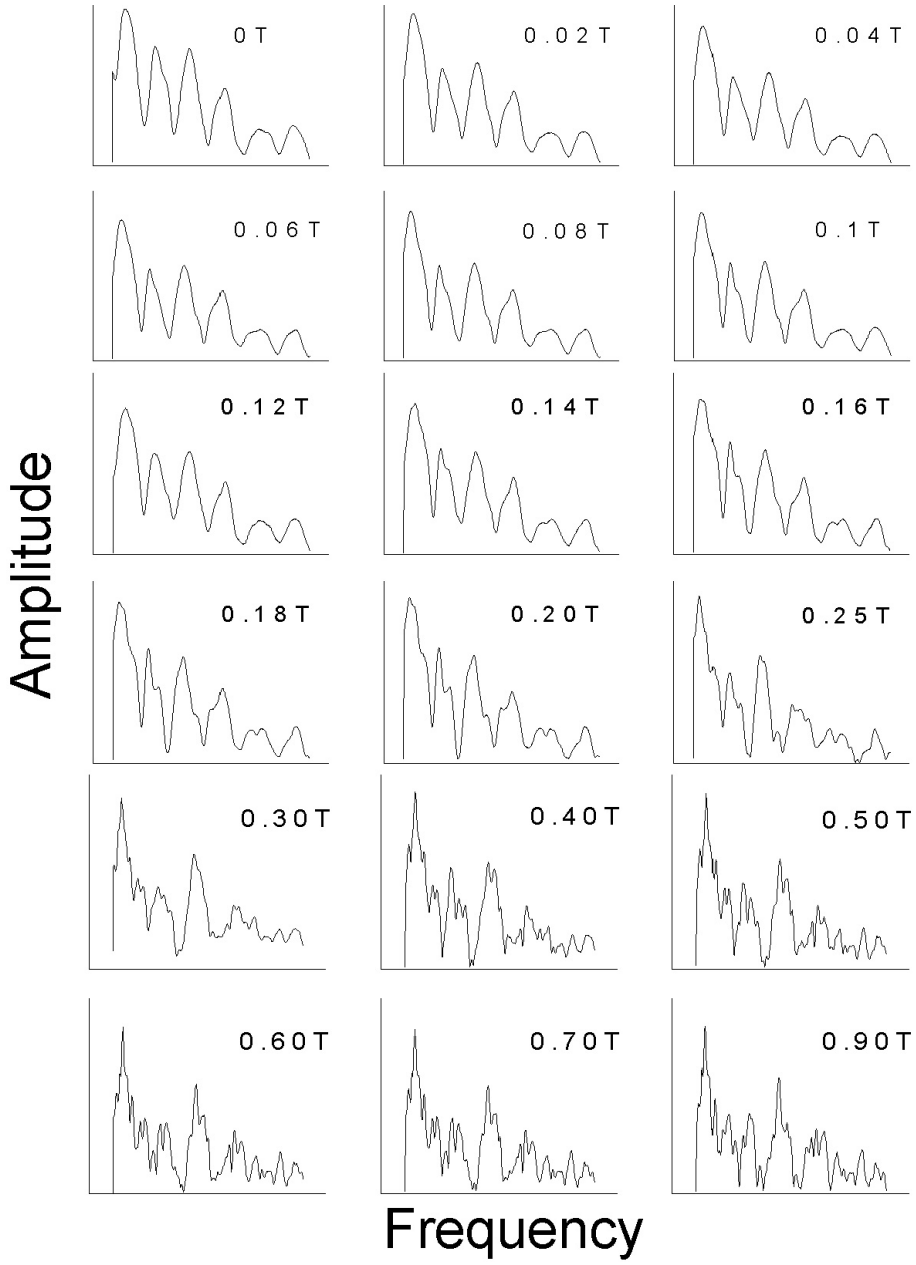

Figure 4.7: The wave spectrum of the magnetic field dependence of the shear elastic wave with polarization direction along $[1\bar{1}0]$ and propagation direction along [110], which is for conducting the elastic constant, C'. The spectrums show significant changes with an external magnetic field around 0.25T

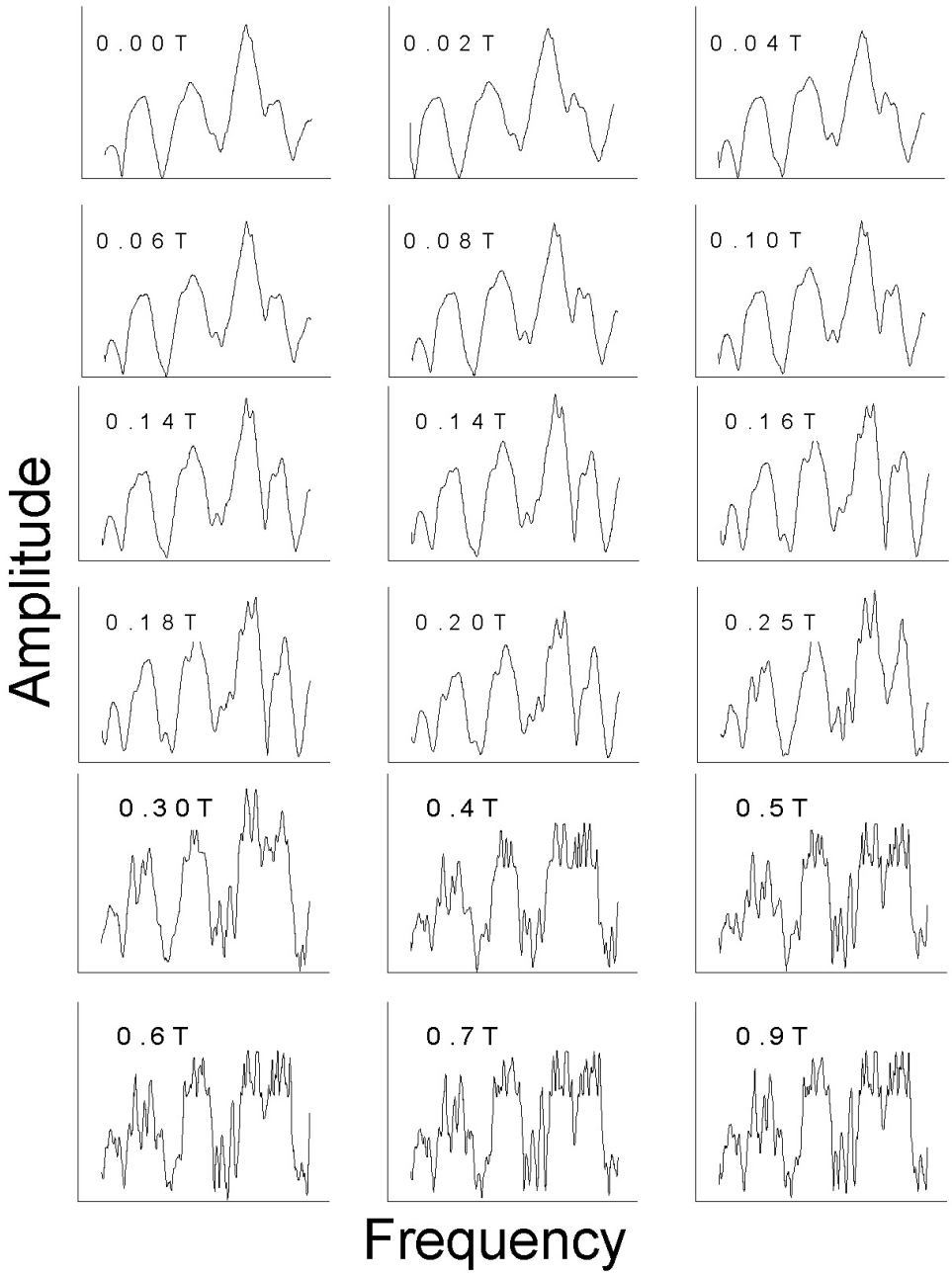

Figure 4.8: The wave spectrum of the magnetic field dependence of the shear elastic wave with polarization direction along [110] and propagation direction along [100], which is for conducting the elastic constant, C_{44}. The spectrums show significant changes with a external magnetic field around 0.25T

Chapter 5

Summary

Ferromagnetic shape memory alloys (FSMA) have been scientifically interesting due to the possibility of inducing the shape memory effect with an external applied magnetic field. They can produce very large repeatable strains and can produce large work output against smaller applied loads. The loads and magnetic field can be both used to bias the microstructure. The variants rearrangement phenomenon is a complicated one that depends on twin boundary mobility, the magnetic properties of the materials, proper biasing of the initial microstructure, proper specimen orientation, and specimen shape, among others.

The main purpose of this thesis study was centered on the elasticity study, which could provide insight into the nature of the materials. Since the elastic constants are very sensitive, a good experimental method was chosen as ultrasonic continuous wave method. An automatic control system was design and set up for all these elastic constants measurements with capability of applying magnetic field and wide temperature range. The results of all the elastic constants of FSMAs, Ni_2MnGa and Fe_3Pd, were reported and discussed in Chapter 3 and Chapter 4, which were briefly concluded as:

1. The dependence of a solid's elastic properties on temperature of $Ni_{0.5}Mn_{0.284}Ga_{0.216}$, $Ni_{0.49}Mn_{0.234}Ga_{0.276}$ and Fe_3Pd were studied. Measurements were conducted by the ultrasonic continuous wave method.

2. The temperature dependences of the elastic constants of the austenitic state in these two Ni_2MnGa were studied. Anomalous behavior of the elastic constants temperature dependence in austenitic $Ni_{0.5}Mn_{0.284}Ga_{0.216}$ was observed, especially an abrupt 15% softening of C_{11} at the Curie temperature. The latter anomaly was found to be strongly influenced by the presence and orientation of applied magnetic fields. This anomalous phenomenon indicates a premartensitic transition. Moreover in the austenitic phase of $Ni_{0.49}Mn_{0.234}Ga_{0.276}$, the elastic constants also showed a transition before martensitic phase transformation.

3. The temperature dependence of the martensitic phase of Ni_2MnGa was investigated. The key to conduct those ultrasonic continuous wave technique measurements in tetragonal martensite is using the magnetic field to bias the crystal to be single variant. In martensitic $Ni_{0.5}Mn_{0.284}Ga_{0.216}$, the temperature dependences of the velocities of all eleven elastic wave modes had abrupt changes at the temperature far below the martensitic phase transformation. The results indicate a structural phase change from the tetragonal to a second phase at lower temperature. It leads to propose an intermartensitic phase transformation.

4. The C' constant, which softened in the austenitic phase, splits into two at the M_S temperature. One of the two new shear moduli stiffens before softening again at the lower transformation M_{S2}. The other modulus, C*, was

shown to remain very soft, from M_S to M_{S2}. The standard Landau theory of structural transitions, where strain is the order parameter, assumes that the appropriate elastic modulus softens to zero as a function of temperature while the coefficients of the higher order terms in the expression of the free energy are independent of temperature. This model cannot describe the observed re-entrant behavior of C'. Here we assume that the coefficient of the third-order term also has significant temperature dependence. This assumption results in a C' vs. temperature in good agreement with observation. The temperature behavior of the other soft modulus, C*, is not as well described in this model.

5. The temperature and magnetic field effects in Fe_3Pd by the elastic constants measurements were investigate by the ultrasonic continuous wave method. The abrupt change of the elastic constants at around 45^OC indicate a possible premartensitic transformation. The magnetic field dependence of elastic constants shows a probably magnetic field induced transition.

Appendix A

Publications

1 **Liyang Dai**, James Cullen, and Manfred Wuttig, "Model for the Elastic Behavior Near Intermartensitic Transitions", J. Appl. Phys., Accepted. (2004)

2 **Liyang Dai**, James Cullen, and Manfred Wuttig, "Intermartensitic Transformation in a NiMnGa Alloy", J. Appl. Phys., Vol95, no.11, 6957-9 (June 2004)

3 **Liyang Dai**, James Cullen, Jun Cui, Manfred Wuttig "Elasticity study in Ferromagnetic shape memory alloys", Mat. Res. Soc. Symp. Proc., 785, D2.2.1(invited paper)(2004)

4 **Liyang Dai**, J. Cui and M. Wuttig, "Elasticity of austenitic and martensitic NiMnGa," in Proceedings of SPIE Vol. 5053 Smart Structures and Materials 2003: Active Materials: Behavior and Mechanics, edited by Dimitris C. Lagoudas, (SPIE, Bellingham, WA, 2003) 595-602

5 **Liyang Dai**, J. Cullen and M. Wuttig, "Magnetism, Elasticity and Magnetostriction of FeCoGa Alloys", J. Appl. Phys., 93, no.10, 8627-9 (2003)

6 M. Wuttig, **Liyang Dai**, J. Cullen, Elasticity and Magnetoelasticity of Fe-Ga Solid Solutions. Applied Physics Letters, 80, no.7, 1135-7 (Feb. 2002.)

BIBLIOGRAPHY

[1] D. I. Bolef and M. Menes. Magnetostriction in ferromagnetic shape memory alloys. *J. Appl. Phys.*, 31:1010, 1960.

[2] R. M. Bozorth. *Ferromagnetism*. D. Van Nostrand Company, Inc., 1st edition, 1951.

[3] R.M. Bozorth, E. F. Tilden, and A. J. Williams. Anisotropy and magnetostriction of some ferrites. *Phys. Rev.*, 99(10):1788, 1955.

[4] K. Brugger. Pure modes for elastic waves in crystals. *J. Appl. Phys.*, 36(3):759, 1964.

[5] V.A. Chernenko, C.Segui, E.Cesari, J.Pons, and V.V.Kokorin. Sequence of martensitic transformations in NiMnGa alloys. *Phys. Rev. B*, 57:2659, 1998.

[6] V.A. Chernenko, V.A. L'vov, and M.Pasquale. Magnetoelastic behavior of NiMnGa martensitic alloys. *International Journal of Applied Electromagnetics and Mechanics*, 12:3, 2000.

[7] V.A. Chernenko, J. Pons, C. Segui, and E.Cesari. Premartensitic phenomena and other phase transformations analysis and electron diffraction. *Acta Mater.*, 50:53, 2002.

[8] S. Chikazumi and S. H. Charap. *Physics of Magnetism*. Krieger Publishing, 1964.

[9] A. E. Clark. *Ferromagnetic Materials (Magnetostrictive Rare Earth-Fe Componds)*. North Holland Publ. Co., 1980.

[10] A. E. Clark, J. B. Restorff, M. Wun-Fogle, T. A. Lograsso, and D. L. Schlagel. Magnetostrictive properties of body-centered cubid Fe-Ga and FeGaAl alloys. *IEEE Tran. Magn.*, 36:3238, 2000.

[11] A.E. Clark, M. Wun-Fogle, J.B. Restorff, T.A. Lograsso, A. R. Ross, and D. L. Schlagel. Magnetostrictive galfenol/alfenol alloys under large compressive stresses. *Proceedings of 7th International Conference on New Actuators*, 2000.

[12] J. Cui. *Martensitic Phase Transformations and Ferromagnetic Shape Memory Effects in FePd Single Crystal*. PhD thesis, University of Minnesota, 2002.

[13] J. Cui, T. W. Shield, and R.D. James. Phase transformation and magnetic anisotropy of an iron-palladium ferromagnetic shape memory alloy. *Acta Materialia*, 52(1):35, 2004.

[14] B. D. Cullity. *Introduction to Magnetic Materials*. Addison-Wesley Publishing Company, 1st edition, 1972.

[15] L. Dai, J. Cullen, J. Cui, and M. Wuttig. Anomalous behavior of the elastic constants in $Ni_{0.50}Mn_{0.284}Ga_{0.216}$. *Appl. Phys. Lett.*, submitted, 2003.

[16] L. Dai, J. Cullen, and M. Wuttig. Intermartensitic transformation in a NiMnGa alloy. *J. Appl. Phys.*, 95(11):6957, 2004.

[17] A. DeSimone and R. D. James. A constrained theory of magnetoelasticity. *Journal of Applied Physics*, 81:5706, 1997.

[18] G. Fritsch, V. V. Kokorin, and A. Kempf. Soft modes in ni2mnga single crystal. *J. Phys. Condens. Matter*, 6:L107, 1994.

[19] A. Gonzalez-Comas, E. Obrado, L. Maosa, and A. Planes. Premartensitic and martensitic phase transitions in ferromagnetic Ni_2MnGa. *Phy. Rew. B*, 60(10):7085, 1999.

[20] A. Gonzalez-Comas, E. Obrado, L. Maosa, A. Planes, and A. Labarta. Magnetoelasticity in the heusler Ni_2MnGa alloy. *J. Magn. Magn. Mater.*, 196-197:637, 1999.

[21] R. C. Hall. Single crystal anisotropy and magnetostriction constants of several ferromagnetic materials including allous of NiFe, SiFe, AlFe CoNi, and CoFe. *J. Appl. Phys.*, 30(6):816, 1958.

[22] M. Haluska, D. Havlik, G. Kirlinger, and W. Schranz. Acoustic phonon dispersion in single crystal C_{60}. *J. Phys. Condens. Matter*, 11:1009, 1999.

[23] G. Hausch. Anormalous elastic behavior of invar alloys. *International Journal of Magnetism*, 5(1-3):111, 1973.

[24] G. Hausch. Magnetic exchange energy contribution to the elastic constants and its relation to the anomalous elastic behaviour of invar alloys. *Physica Status Solidi A*, 15(2):501, 1973.

[25] G. Hausch. Low temperature acoustic relaxation effect in FeNi and FePt invar alloys. *Journal of Physics F (Metal Physics)*, 6(6):1015, 1976.

[26] G. Hausch. On the present understanding of the bulk modulus anomaly of invar alloys in the itinerant electron model of ferromagnetism. *Journal of Physics F (Metal Physics)*, 7(5):L127, 1977.

[27] E. Hornbogen and N. Jost. *The Martensitic Transformation in Science and Technology*. Obserursel: DGM Informationsquesellschaft, 1st edition, 1989.

[28] R. Hultgren and C. A. Zapffe. The crystal structures of the iron-palladium superlattices. *Z. Krist*, 99:509, 1938.

[29] R. Hultgren and C. A. Zapffe. Gamma to alpha transformation in iron alloyed with palladium. *Nature*, 142:395, 1938.

[30] R. D. James and M. Wuttig. Magnetostriction of martensite. *Philosophical Magazine A*, 77(5):1273, 1998.

[31] A. G. Khachaturyan, S. M. Shapiro, and S. Semenovskaya. Adaptive phase formation in martensitic transformation. *Phys. Rev. B*, 43(13):10832, 1991.

[32] C. Kittel. *Introduction to Solid State Physics*. John Wiley and Sons, Inc, 7th edition, 1996.

[33] V.V. Kokorin, V.A. Chernenko, E. Cesari, J. Pons, and C. Seguí. Pre-martensitic state in Ni_2MnGa. *H. Phys. Condens. Matter*, 8:6457, 1996.

[34] V.V. Kokorin and V. Martynov. Modulated structures in Ni_2MnGa. *Phase Transitions*, B43(1-4):209, 1993.

[35] A. Kussmann and K. Jessen. Magnetic and dilatometric measurements applied to the transformation kinetics of iron-palladium alloys. *Z. Metallk.*, 54:504, 1963.

[36] Y. Liang, Y. Sutou, T. Wada, C. Lee, M. Taya, and T. Mori. Magnetic field-induced reversible actuation using ferromagnetic shape memory alloys. *Scripta Materialia*, 48:1415, 2003.

[37] V. Martynov and V.V. Kokorin. The crystal structure of thermally and stress induced martensite in Ni_2MnGa. *Journal de Physique III*, 2(5):739, 1992.

[38] S. J. Murray, M. Marioni, S. M. Allen, R. C. O'Handley, and T. A. Lograsso. 6% magnetic field induced strain by twin boundary motion in ferromagnetic nimnga. *Appl. Phys. Lett.*, 77:886, 2000.

[39] J. R. Neighbours and G. E. Schacher. Determination of elastic constants from sound-velocity measurements in crystals of general symmetry. *J. Appl. Phys.*, 38:5366, 1967.

[40] Z. Nishiyama. *Martensitic Transformation*. Academic Press, New York, 1st edition, 1978.

[41] L. Ma nosa, A. González-Comas, E. Obradó, and A. Planes. Anomalies related to the TA2- phonon-mode condensation in the heusler ni_2mnga alloy. *Phys. Rev. B*, 55:11068, 1997.

[42] A. S Nowick and B. S. Berry. *Anelastic Relaxation in Crystalline Solids*. Academic Press, New York, 1st edition, 1972.

[43] E. Obrad, A. Gonzalez-Comas, L. Manosa, and A. Planes. Magnetoelastic behavior of the heusler Ni_2MnGa alloy. *J. Appl. Phys.*, 83(11):7300, 1998.

[44] R. C. O'Handley. Model for strain and magnetization in magnetic shape memory alloys. *J. Appl. Phys.*, 83(5):3263, 1998.

[45] R. C. OHandley, S. J. Murray, M. Marioni, H. Nemback, and S. M. Allen. Phenomenology of giant magnetic-field-induced strain in ferromagnetic shape-memory materials. *J. Appl. Phys.*, 87(9):4712, 2000.

[46] A. Planes, E. Obrad, A. Gonzalez-Comas, and L. Maosa. Premartensitic transition driven by magnetoelastic interaction in bcc ferromagnetic Ni_2MnGa. *Phys. Rev. Lett.*, 79(20):3926, 1997.

[47] E. Raub, H. Beeskow, and O. Loebich. The phase diagram iron-palladium below 950. *Z. Metallk.*, 54:549, 1963.

[48] S. M. Shapiro, J. Z. Larese, Y. Noda, S. C. Moss, and L. E. Tanner. Neutron-scattering study of premartensitic behavior in ni-al alloys. *Phys. Rev. Lett.*, 57(25):3199, 1986.

[49] S. M. Shapiro, B. X. Yang, Y. Noda, L. E. Tanner, and D. Schryvers. Neutron-scattering and electron-microscopy studies of the premartensitic phenomena in ni_xal_{100-x} alloys. *Phys. Rev. B*, 44(17):9301, 1991.

[50] S. M. Shapiro, B. X. Yang, G. Shirane, Y. Noda, and L. E. Tanner. Neutron scattering study of the martensitic transformation in a ni-al beta-phase alloy. *Phys. Rev. Lett.*, 62(11):1298, 1989.

[51] K. Shimizu and T Kakashita. Effect of magnetic fields on martensitic transformations in ferrous alloys and steels. *ISIJ International*, 29:97, 1989.

[52] S. Siegel and S. Quimby. The variation of young's modulus with magnetization and temperature in nickel. *Phys. Rev.*, 49:663, 1936.

[53] A. Sozinov, A. A. Likhachev, N. Lanska, and K. Ullakko. Giant mqagnetic-field-induced strain in nimnga seven-layered martensitic phase. *Appl. Phys. Lett.*, 80:1746, 2002.

[54] A. Sozinov, A. A. Likhachev, and K. Ullakko. Crystal structures and magnetic anisotropy properties of ni-mn-ga martensitic phases with giant magnetic-field-induced strain. *IEEE Trans. on Magnetics*, 38:2814, 2002.

[55] E.E. Stenger and J. Trivisonno. Ultra study of the two-step martensitic phase transformation in Ni_2MnGa. *Physical Review B.*, 57(5):2735, 1998.

[56] U. Stuhr, P. Vorderwisch, V. V. Kokorin, and P. A. Lindgard. Premartensitic phenomena in the ferro- and paramagnetic phases of Ni_2MnGa. *Physical Review B.*, 56(22):14360, 1997.

[57] R. Tickle and R. D. James. Magnetic and magneto-mechanical properties of Ni_2MnGa. *Journal of Magnetism and Magnetic Materials*, 195:627, 1999.

[58] R. Tickle, R. D. James, T. Shield, M. Wuttig, and V. V. Kokorin. Ferromagnetic shape memory in the Ni_2MnGa system. *IEEE Transactions on Magnetics*, 35(5):4301, 1999.

[59] E. Torok and G. Hausch. Bulk modulus anomaly of fe-ni and Fe-Pt invar alloys. *Physica Status Solidi A*, 53:K147, 1979.

[60] K. Ullakko, J. K. Huang, C. Kantner, R. C. O'Handley, and V. V. KoKorin. Large magnetic field induced strains in Ni_2MnGa single crystals. *Appl. Phys. Lett.*, 69(13):1966, 1996.

[61] A. N. Vasil'ev, A. D. Bozhko, V. V. Khovailo, I. E. Dikshtein, V. G. Shavrov, V. D. Buchelnikov, M. Matsumoto, S. Suzuki, T. Takagi, and J. Tani. Structural and magnetic phase transitions in shape-memory alloys $Ni_{2+x}Mn_{1-x}Ga$. *Phys. Rev. B*, 59(2):1113, 1999.

[62] A. N. Vasil'ev, S. A. Klestov, R. Z. Levitin, and V. V. Snegirev. Magnetoelastic interaction in the martensitic transformation in an Ni_2MnGa single crystal. *JETP*, 82(3):524, 1996.

[63] A. N. Vasil'ev, V. V. Kokorin, Y. I. Savchenko, and V. A. Chernenko. Electromagnetic generation study of Ni_2MnGa. *Sov. Phys. JETP*, 71:803, 1990.

[64] P. J. Webster, K. R. A. Ziebeck, S. L. Town, and M. S. Peak. Magnetic order and phase transformation in Ni_2MnGa. *Philosophical Magazine B*, 49(3):295, 1984.

[65] J. Worgull, E. Petti, and J. Trivisonno. Behavior of the elastic properties near an intermediate phase transition in Ni_2MnGa. *Physical Review B.*, 54(22):15696, 1996.

[66] T. T. Wu. Elastic wave propagation and nondestructive evaluation of maerials. *Proc. Natl. Sci. Counc. ROC (A)*, 23(6):703, 1999.

[67] M. Wuttig, J. li, and C. Craciunescu. A new ferromagnetic shape memory alloys system. *Scripta Materialia*, 44:2393, 2001.

[68] A. Zheludev and S. M. Shapiro. Uniaxial stress dependence of the [ζ ζ 0]-ta_2 anomalous phonon branch in ni_2mnga. *Solid State Commun.*, 98:35, 1996.

[69] A. Zheludev, S. M. Shapiro, and P. Wochner. Precursor effects and premartensitic transformation in ni_2mnga. *Phys. Rev. B.*, 54:15045, 1996.

[70] A. Zheludev, S. M. Shapiro, P. Wochner, A. Schwartz, M. Wall, and L. E. Tanner. Phonon anomaly central peak and microstructures in ni_2mnga. *Phys. Rev. B.*, 51:11310, 1995.